Dias Fahmi Fajrin

3D Geomechanical Model

In the Lower Germanic Triassic Group of De Lier Field, the Netherlands

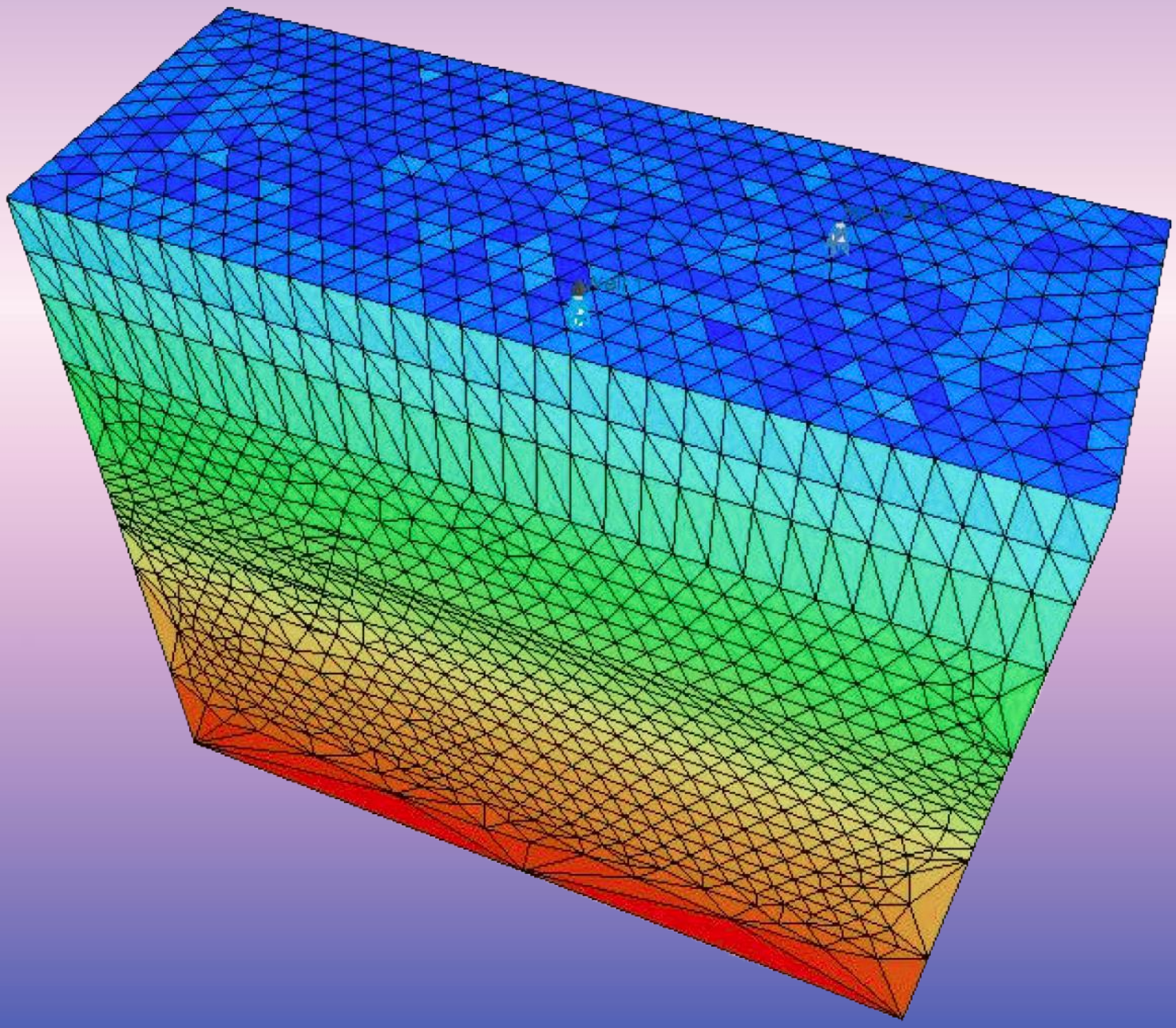

TU Delft

3D Geomechanical Model
In the Lower Germanic Triassic Group of De Lier Field the Netherlands

By

Dias Fahmi Fajrin

in partial fulfilment of the requirements for the degree of

Master of Science
in Applied Earth Science

at the Delft University of Technology,
to be defended publicly on Thursday May 28, 2020 at 11.00 AM

Supervisor:	Prof. Dr. G. Bertotti	TU Delft
Thesis committee:	Drs. J.C. Blom	TU Delft
	Dr. A. Barnhoorn	TU Delft

TU Delft

This page is left blank intentionally

Preface

This thesis marks the end of my study at the Delft University of Technology. Therefore, I would like to express my gratitude to the people who have supported me through the last tough few years.

First, I would like to express my sincere gratitude to my principal supervisor Prof. Giovanni Bertotti for the opportunity to join this project. Through his guidance, patience, and feedback, I finally finish my master's thesis.

Special thanks to both of my graduation committees, Dr. Auke Barnhoorn & Dr. Jan Kees Blom, for taking place in my graduation committee.

Also, I would like to thank the Indonesian Endowment Fund for Education (LPDP) for allowing me to study at TU Delft by financially supporting me during the study. I also feel grateful for PLN (Perusahaan Listrik Negara) for allowing me to pursue my dream to study in one of the best universities in the world.

I would like to dedicate this achievement to my beloved parents, my wife, and my daughter, my sister, and my brother, for their unconditional support at all times.

Lastly, I would like to thank all my classmates in the Petroleum Engineering and Geosciences class of 2016 and all Indonesian students in Delft for all the friendships.

Dias Fahmi Fajrin
Delft, May 2020

This page is left blank intentionally

Contents

List of Figures

List of Tables

List of Equations

This page is left blank intentionally

Abstract

As the world's population continues to increase, the demand for energy also increases. However, the use of fossil fuel energy has resulted in disadvantageous impacts for humans and the Earth. This condition becomes a good momentum to find a clean and more sustainable energy resources, given the fact that fossil fuel energy is a non-renewable resource that someday, in the future, its availability becomes scarce. Additionally, environmental awareness concerning energy-mix use and combating climate change also increases globally.

Geothermal energy is one of the better alternatives for energy sources, as it is renewable as well as clean and green. A study from the Netherlands Organization for Applied Scientific Research (TNO) says that deeper Triassic sandstones, with possibly higher temperatures, could also potentially contain geothermal reservoirs. Therefore, this condition has paved the way for the exploration of the deep reservoir.

The assessment of geothermal production usually faces considerable uncertainty due to, among other things, lack a comprehensive geomechanical model. Therefore, knowledge of the current state of stress is essential to address a wide range of problems that might arise during geothermal exploration and production—those problems such as wellbore stability, fault reactivation, induced seismicity, and deformation in depleting reservoirs.

This study aims to construct a 3D geomechanical model in the Lower Germanic Triassic group, in De Lier field. By using the effective stress ratio concept, a 3D geomechanical model is constructed to describe the principal stresses distribution. The principal stresses distribution determines how the faulting stress regime will be formed. The vertical stress, as one of the principal stresses, is controlled by depth and density. On the other hand, the minimum horizontal stress is controlled by Poisson's ratio. Four models are constructed based on several assumptions. In the model where gravity is the only source of stress, the maximum principal stress $\sigma 1$ is always vertical. Whereas, in the models where tectonic stress is included, three depth intervals related to the faulting stress regime are observed. Imposing greater tectonic stress to the model will shift the depth of transition downward.

Cross-section analysis shows that the local principal stresses variation due to the presence of different stratigraphic units and geological structures (faults and fractures). Fractures and faults at particular depth are inactive under the current stress field. Furthermore, pore pressure and friction coefficient have a significant impact on faults and fractures stability.

Keyword: stress field, the west Netherlands basin, geothermal, 3D geomechanical model, geology

This page is left blank intentionally

1 Introduction

1.1. General Overview

The increase in the world population comes with the fact that the insatiable energy demand also increases. However, our knowledge and awareness of the negative impact of fossil fuel use on the environment continue to increase. Moreover, fossil fuel energy is the non-renewable energy resource that someday, in the future, its availability becomes scarce.

Therefore, the effort to find unconventional and more sustainable energy resources, in the past few decades, has led to several results, such as geothermal energy. Geothermal energy is one of the better alternatives for energy sources, as it is renewable as well as clean and green. The use of geothermal energy means the use of heat that is stored in the sub-surface. The two primary uses of geothermal energy are the direct use of heat and electricity generation (Bonté et al., 2012). So, the combination of a permeable layer as well as large-scale circulation of fluid makes the exploitation of geothermal energy possible.

Geothermal technologies are classified into two distinctive categories. The first one is a shallow geothermal system, a relatively small scale, and produces low-temperature heat (Straathof, 2012). The other one is a deep geothermal system, larger-scale basin areas where elevated temperatures are found (Batchelor, 1984). Moreover, It is considered that the most significant portion of the world's mineral, energy, and water resources is hosted in sedimentary basins (Cacace et al., 2010; Raffensperger and Vlassopoulos, 1999). The Netherlands is one of the locations that have a large variety of permeable sedimentary layers, thus making this country has considerable potency for utilizing geothermal energy.

Geothermal energy utilizes geothermal gradients. The temperature gradients show how the temperature rises with depth from the surface to the core. A recent study estimated that the average thermal gradients in the Netherlands is 31.3°C/km (Bonté et al., 2012). That makes an aquifer at three kilometers depth has approximately a temperature of at least 90°C. Figure 1 shows the temperature at the base of the Triassic formation. The temperature at the West Netherlands Basin, indicated by a red rectangle, could reach at least 120°C. It can be concluded that the Triassic formation in the West Netherlands Basin is one of the sedimentary basins in the Netherlands that has a highest sub-surface temperature.

In the Netherlands alone, the Geological Survey of the Netherlands estimated the total recoverable heat from this type of resource could reach approximately 55 times greater than annual heat consumption (Kramers et al., 2012; Willems et al., 2017). Geothermal reservoirs with depths more than 100 m and average thermal gradients, called low enthalpy, are used for direct heating. At present, the growth of geothermal energy in the Netherlands is mainly low-enthalpy heating of districts and greenhouses (Bonté et al., 2012). When subsurface temperatures are sufficiently high, the heat can also be used to generate electricity (Limberger et al., 2018). Therefore, high-enthalpy reservoirs are usually drilled deeper than low-enthalpy and only selected places suitable for this deep or ultra-deep geothermal system (Figure 2).

The target layers for geothermal exploration in the Netherlands are mostly sandstones from the Cretaceous-Rijnland Group and the Jurassic-Schieland Group (Bonté et al., 2012). On the other hand, a study conducted by Netherlands Organization for Applied Scientific Research (TNO) says

that deeper Triassic sandstones, with possibly higher temperatures (Figure 1 and Figure 2), could potentially contain geothermal reservoirs (Van Wees et al., 2010). However, the geothermal explorations of the deep reservoirs in the Netherlands has remained an unresolved challenge due to, among other things, lack of site-specific geomechanical descriptive models. Such models can be used to predict reservoir response under given state of stress conditions.

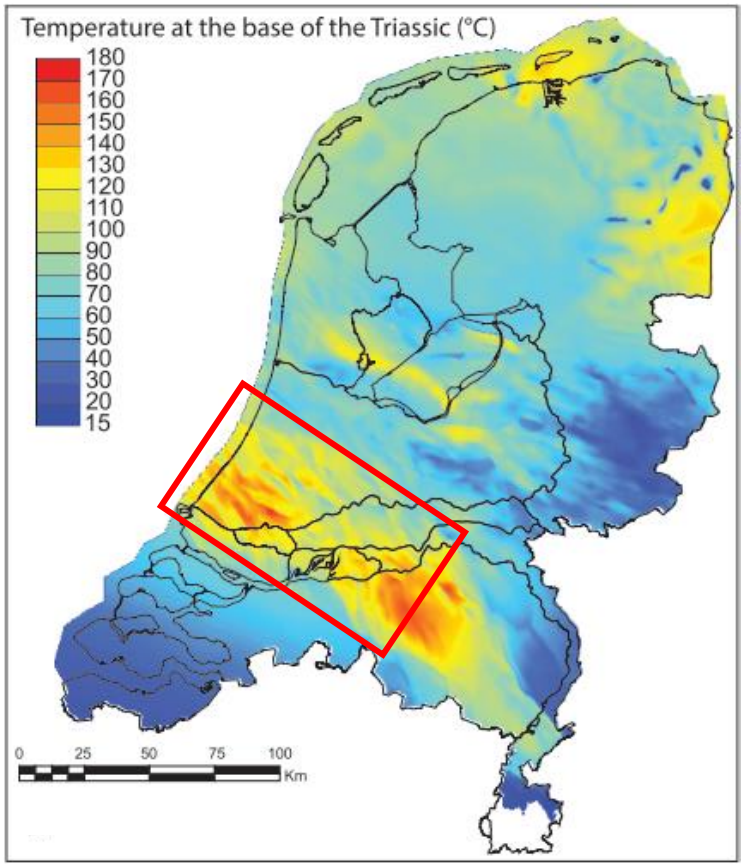

Figure 1. The temperature at the base of the Triassic. The red rectangle marks the WNB After Bonté et al. (2012)

Safe usage of many subsurface activities become one of the essential challenges in energy exploration. In this context, knowledge of present-day in-situ stress is vital for the management of hydrocarbon and geothermal reservoirs (Fuchs and Müller, 2001; Zoback, 2010). The in-situ stress data is then used to address problems that might arise due to fluid injections or fluid productions. Those problems, among other things, are induced seismicity in deep and ultra-deep geothermal production, reactivation of sealing faults, wellbore stability, and subsidence due to a long-term depletion (Heidbach et al., 2019; Van Wees et al., 2017; Zang et al., 2014). The magnitude difference between in-situ stress state to a failure criterion is also essential to mitigate hazardous risks. The difference indicates how much stress is allowed on a pre-existing fault to change due to natural or man-made processes before failure takes place (Heidbach et al., 2019; Zoback, 2010). That is some of the risks that one should mitigate prior geothermal exploration and production.

1.2. Research Objectives

This study aims to construct a 3D geomechanical model in the West Netherlands Basin - De Lier field by using seismic and well data of the targeted reservoir. The 3D geomechanical is needed to comprehend the state of stress in the study area. The model also will be used to study the applicability of the effective stress-ratio concept in describing the principal stresses distribution. It is because the principal stresses orientation will determine the stress faulting regimes.

The information on the in-situ stress field and stress-depth profiles are required to address a wide range of problems in reservoir geomechanics. Moreover, the principal stresses can vary laterally and locally due to, among other things, different stratigraphic units and the presence of faults. Therefore, further study will be conducted to understand how the current stress field will impact the existing faults and fractures. Several tectonic stress scenarios will be applied to the 3D geological model to see its impact on the in-situ stress condition.

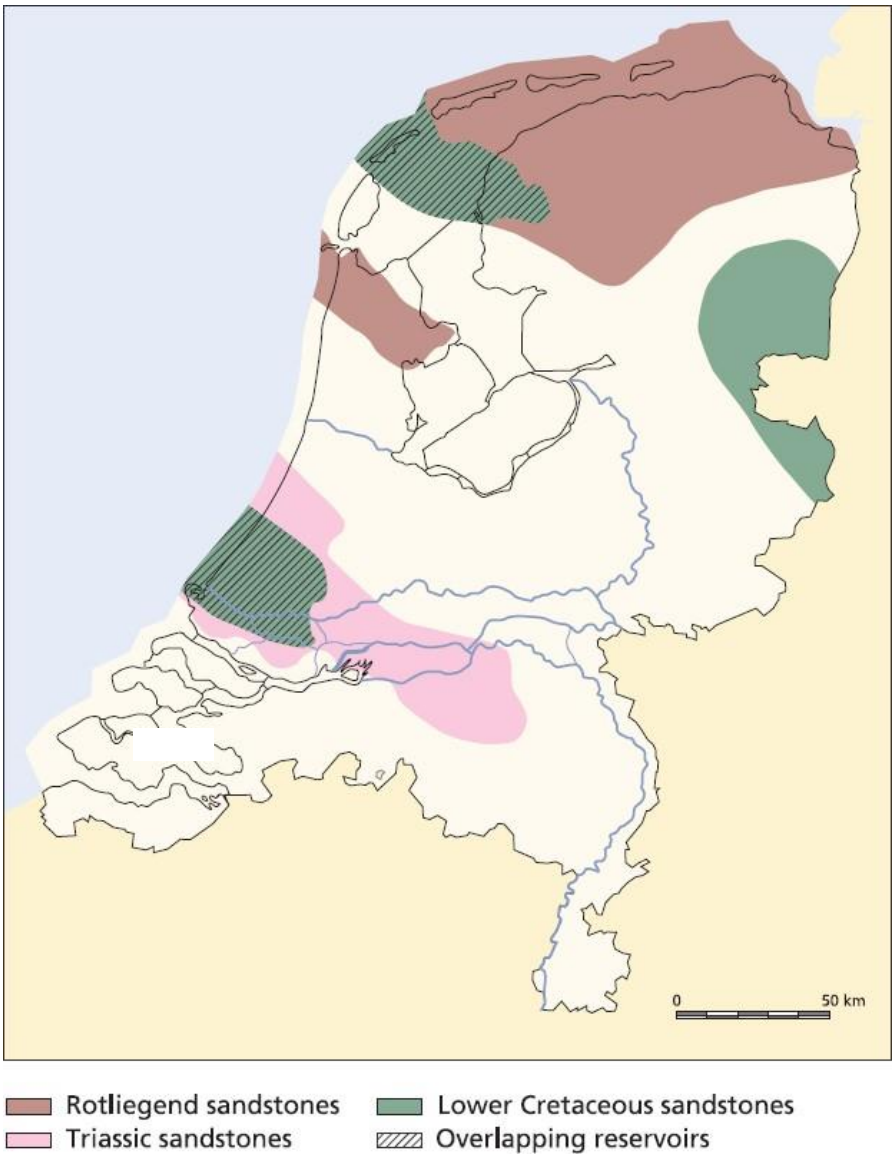

Figure 2. The distribution of reservoirs that suitable for geothermal production in The Netherlands (Wong et al., 2007)

1.3. Outline of the thesis

The organization of this thesis is as follows :

- Introduction to the study
- Literature study of regional geology and basic theory of geomechanics
- Research methodology and dataset used for the study
- Result based on the simulation model
- Discussion of the simulation model results
- Conclusion and recommendation for further study

This page is left blank intentionally

2 Literature Study

2.1. Regional geology

The area study is situated in the southwestern part of the West Netherlands Basin (WNB). The WNB is a rift-inverted basin that experienced through a polyphase tectonic deformation from Late Carboniferous onward (Van Balen et al., 2000). The WNB dimension is approximately 130 km in length and 65 km in width. It lies between London-Brabant Massif (LBM) and Central Netherlands Basin (Figure 3). The presence of major fault-zone toward the South-West becomes a boundary that separates the WNB and the LBM. While the Zandvoort Ridge and Ijmuiden High in the North and North-East separate the WNB from the Central Netherlands and the Broad Fourteen Basins (Van Balen et al., 2000). Toward the South-East, the WNB merges with Roer Valley Graben (RVG).

Late Carboniferous – Early Permian

During this age, the WNB was part of the Southern Permian Basin (Geluk, 2005). The South Permian Basin was located in the foreland of the Variscan Mountains. Therefore, the sediment sources that contributed to the Southern Permian Basin and the WNB were the London Brabant-Massif and Variscan Mountains (Van Balen et al., 2000; Wong et al., 2007).

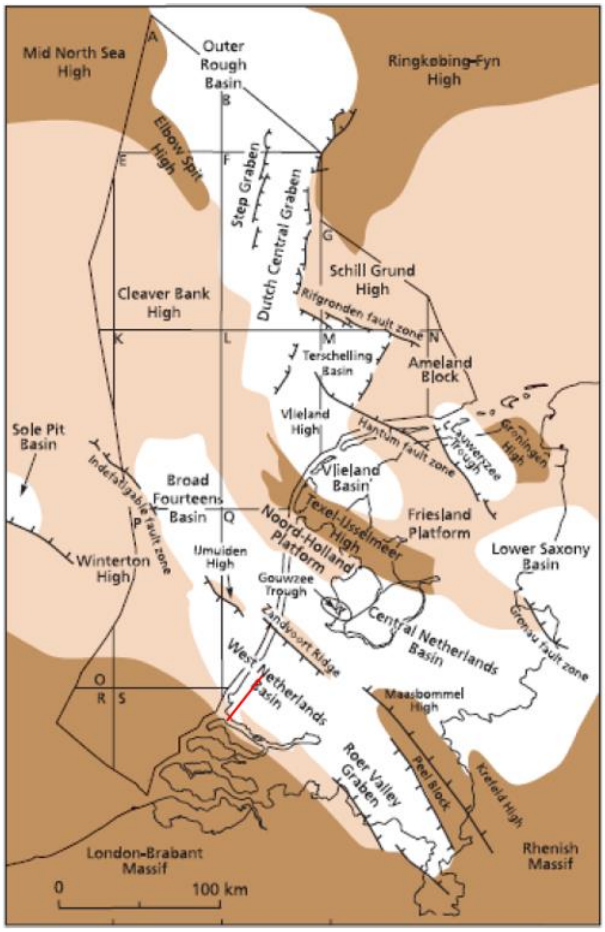

Figure 3. The red rectangle marks the location of the West Netherlands Basin During the Late Jurassic-Early Cretaceous, after Wong et al. (2007)

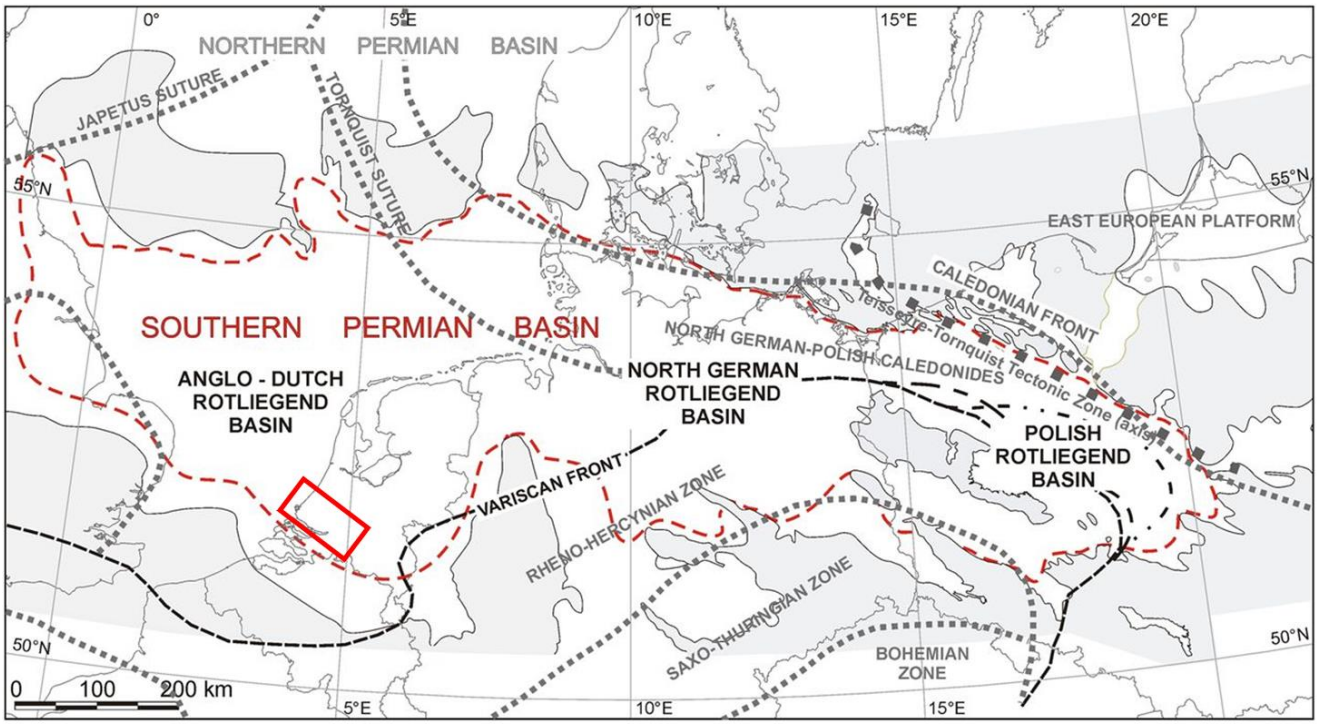

Figure 4. Southern Permian Basin in Europe during the Permian period.
The red rectangle marks the WNB, after Kiersnowski (2013); (Ziegler and Dèzes, 2006)

Late Permian – Middle Jurassic

Figure 4 illustrates the location of the WNB in the E-W striking Southern Permian Basin. The Late Permian marked the early pre-rift stage of the WNB. A short uplift event occurred during the Late Permian, then followed by regional thermal subsidence during the Early Triassic (Ziegler, 1982). Afterward, the Southern Permian Basin became dissected by rifts and split up into some smaller, fault-bounded basins and highs (Wong et al., 2007). Figure 6 and Figure 7 show the NW-SE fault pattern developed in the Triassic formation. The Early Triassic sediments were siliciclastic deposits (lacustrine sediments) with sandstone (fluvial and aeolian) and oolite intercalations. While, The Late Triassic sediment comprises of marine carbonates and evaporites (Geluk et al., 1996; Van Balen et al., 2000).

The middle Triassic marked the start of the Early Kimmerian tectonic phase (Van Balen et al., 2000). Rifting event in this phase was related to the breaking-up of Pangea (De Jager, 2007). By this time, the WNB formed as a half-graben structure with an NW-SE striking trend (Duin et al., 2006; Van Balen et al., 2000).

Late Jurassic – Early cretaceous

The syn-rift stage was marked by the strongest rifting and subsidence event that created tilted fault blocks. The primary rift system in the WNB is categorized as an NW-SE block-faulted trans-tensional system (Wong et al., 2007). On the other hand, this event divided the WNB into several smaller sub-units and caused a significant thickness variation in the Late Jurassic basin infill (Van Balen et al., 2000). The basin was filled with fluvial sediment (De Jager et al., 1996; Donselaar et al., 2015). Rifting gradually ceased at the end of the Early Cretaceous, when marine to coastal sediment of Rijnland Group deposited (De Jager et al., 1996). The WNB, however, continued to subside until the

Late of Cretaceous and resulted in a deep burial of the Main Buntsandstein Subgroup (De Jager, 2007).

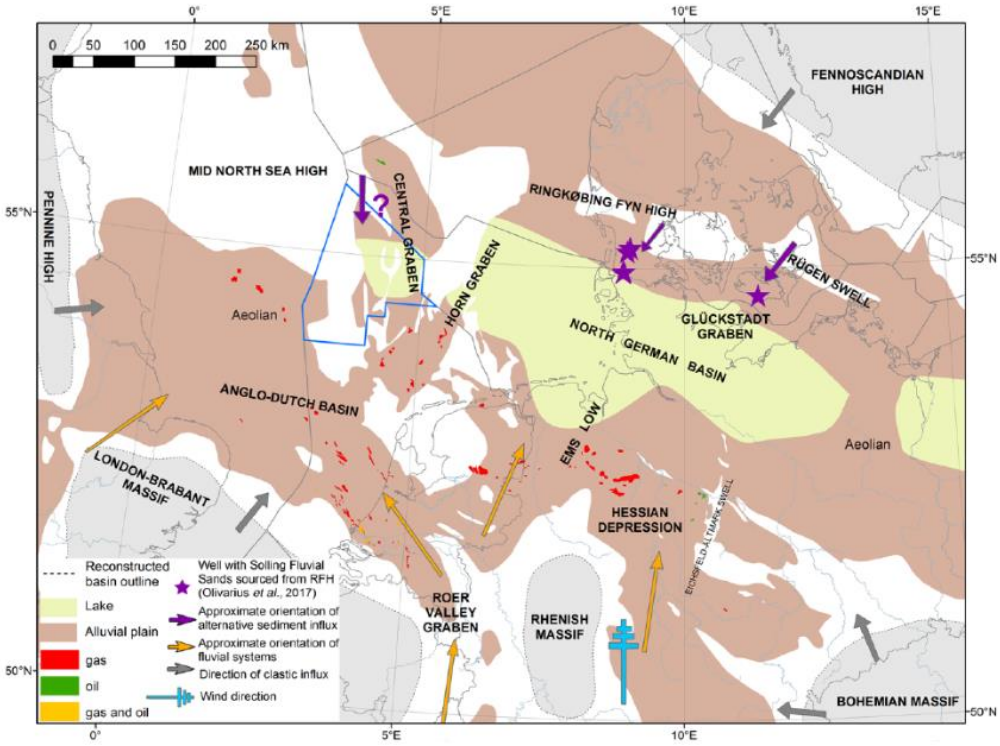

Figure 5. Paleogeographical map of the Southern Permian Basin and its sediment source during the Early Triassic period (Kortekaas et al., 2018)

Late Cretaceous - Tertiary

The Sub-Hercynian compressional phase started from the Late Cretaceous until Early Tertiary as well as marking the early post-rift stage (Verweij et al., 2012). The compressional phase was related to the gradual development of Alpine orogeny. The increasing stresses were then exerted to its northern foreland basin, in which the WNB was situated (De Jager, 2007). By this time, the WNB transformed into an inverted basin due to this compression tectonics. Thus, it also resulted in convergent oblique-slip faulting, general uplift, and erosion that reactivated pre-existing normal rift faults (Rondeel et al., 1996).

Tertiary

The Laramidae inversion phase took place at the Ealy Paleocene (Den Hartog Jager, 1996). During this phase, the WNB was uplifted and followed by a significant erosion, locally down to Triassic. The stable highs structures in the WNB subsided and were filled with Chalk sequences strata (Duin et al., 2006; Van Hulten and Poty, 2008).

The Pyrenean compressional phase occurred at the end of Eocene and caused a broad uplift in the WNB without significant fault reactivation (De Jager, 2007; Pharaoh et al., 2010). Furthermore, the early Miocene was marked by the Savian tectonic phase, albeit there was only an insignificant impact on the WNB (De Jager, 2007).

A geological time scale, including nomenclature, stratigraphy, and tectonic phases, is presented in Figure 9. The applied stratigraphic nomenclature is based on the research conducted by Van Adrichem Boogaert and Kouwe (1993) and improved by Geluk (2005).

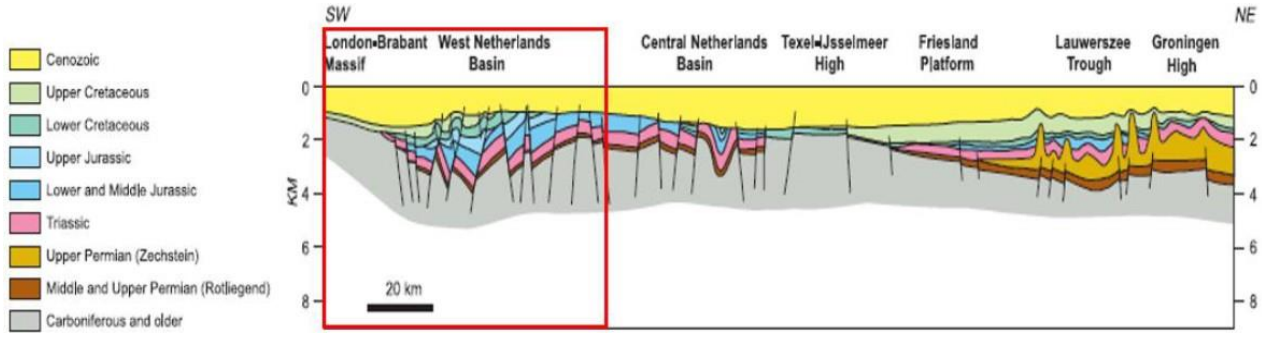

Figure 6. The SW-NE cross-section of the WNB as indicated in Figure 3, after Wong et al. (2007)

2.2. Germanic Triassic Supergroup stratigraphy

The Germanic Triassic lies conformably on top of the Zechstein Group of Permian age (Figure 8 and Figure 9). The presence of Germanic Triassic Group is scattered and has a relatively large thickness in the Mesozoic basins (Verweij et al., 2012), including the WNB, while in the other area, this group is missing due to erosion. The sediments were deposited in an arid to a semi-arid environment, which is characterized by a braided stream with aeolian, interdune, flood-plain, and crevasse-splay environments and terminated in playa lakes (Ames and Farfan, 1996).

Triassic stratigraphy can be classified into two groups; the Upper and Lower Germanic Triassic. The Lower Germanic Triassic Group consists of the Lower Buntsandstein, Volpriehausen, Detfurth, and Hardegsen Formations (Figure 8), where the last three formations formed the Main Buntsandstein subgroup (Wong et al., 2007). The Upper Germanic Triassic Group is divided into Solling, Röt, Muschelkalk, and Keuper Formations (Van Adrichem Boogaert and Kouwe, 1997). The Upper Germanic Triassic Group comprising an alternation of fine-grained clastics, carbonates, and evaporites with subordinate sandstones (Wong et al., 2007).

2.2.1. Main Buntsandstein Subgroup

The Main Buntsandstein Subgroup displays a cyclic alternation of sub-arkosic sandstones and clayey siltstones in large-scale fining-upward sequences (Wong et al., 2007). This subgroup members showed a shift from the fluvial-lacustrine Volpriehausen Formation to the eolian-dominated Hardegsen Formation. The Main Buntsandstein succession's thickness reaches about 200 m the Roer Valley Graben and thinning to 100–150 m toward the West Netherlands Basin (Geluk, 2005).

Volpriehausen Formation

The Volpriehausen Formation forms the lower-most part of the Main Buntsandstein Formation. It deposited in almost all the Netherlands subsurface (Wong et al., 2007). Volprihausen formation composed of the Lower Volpriehausen Sandstone and the Volpriehausen Clay-Siltstone. The Lower Volpriehausen Sandstones were deposited in a fluvial setting and aeolian (Ames and Farfan, 1996;

Wong et al., 2007). While, the Lower Volpriehausen Clay-Siltstone were deposited in lacustrine setting, with subordinate sandstones. The sandstones are more fine-grained than the Lower Volpriehausen Sandstone (Wong et al., 2007).

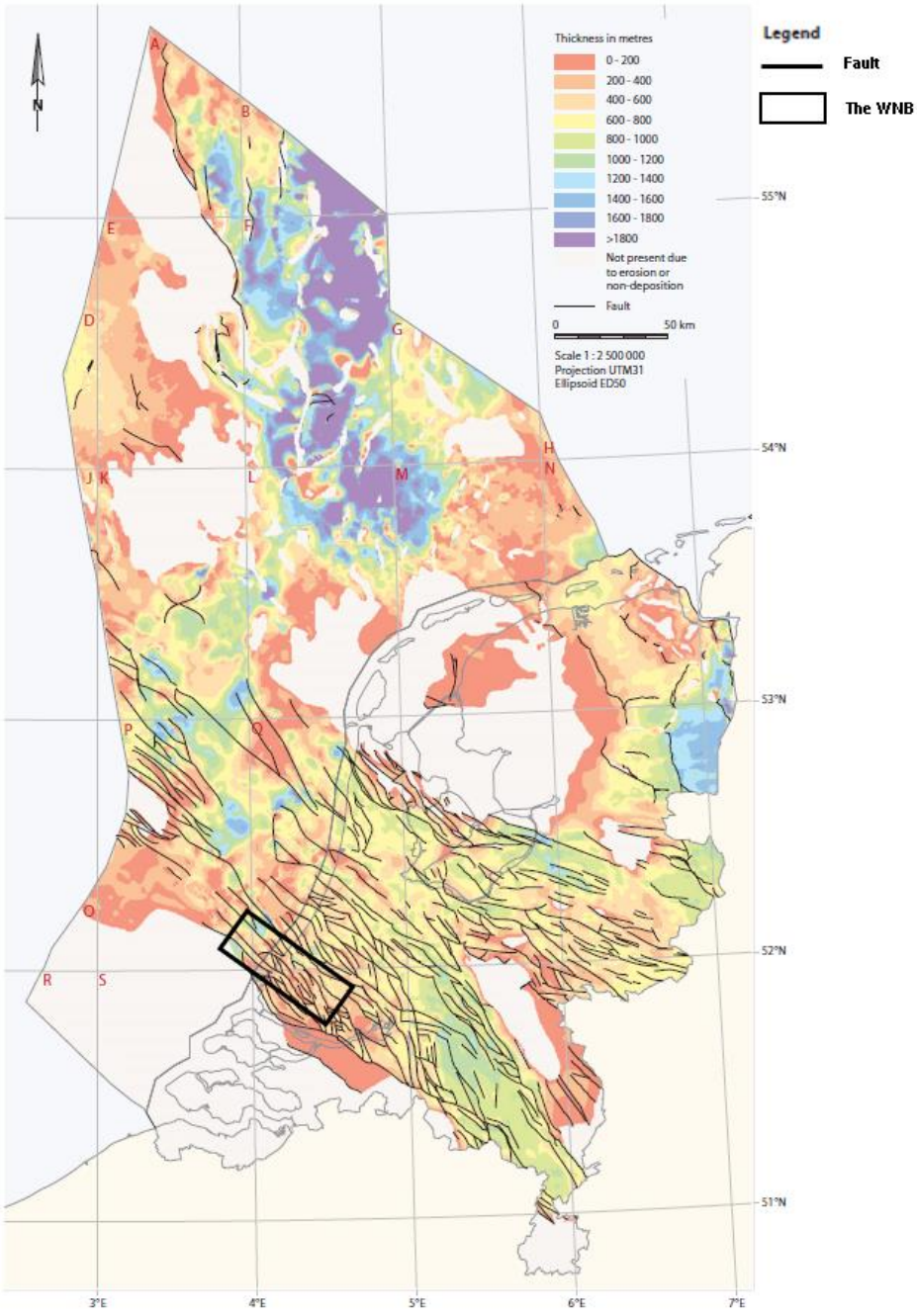

Figure 7. Thickness map of Lower and Upper Germanic Triassic Group, after Duin et al. (2006)

Detfurth Formation

The Detfurth Formation consists of a basal Lower Detfurth Sandstone Member and top Detfurth Claystone Member. In the basin margin area, the sandstone of The Lower Detfurth is considered to be one of the best hydrocarbon reservoirs in the Main Buntsandstein Subgroup. The sandstones have a fluvial and aeolian origin (Geluk and Röhling, 1997). The Lower Detfurth Sandstone Member thickness is only tens of meters in various Dutch Triassic basins. It is composed of claystone, with thin intercalations of siltstone (Wong et al., 2007).

Hardegsen Formation

The Hardegsen Formation is the uppermost of the Main Buntsandstein sequence. The Hardegsen Formation consists predominantly of siltstones with subordinate, thin sandstone beds. The thickness of this formation in the WNB reaches up to 70 m (Wong et al., 2007).

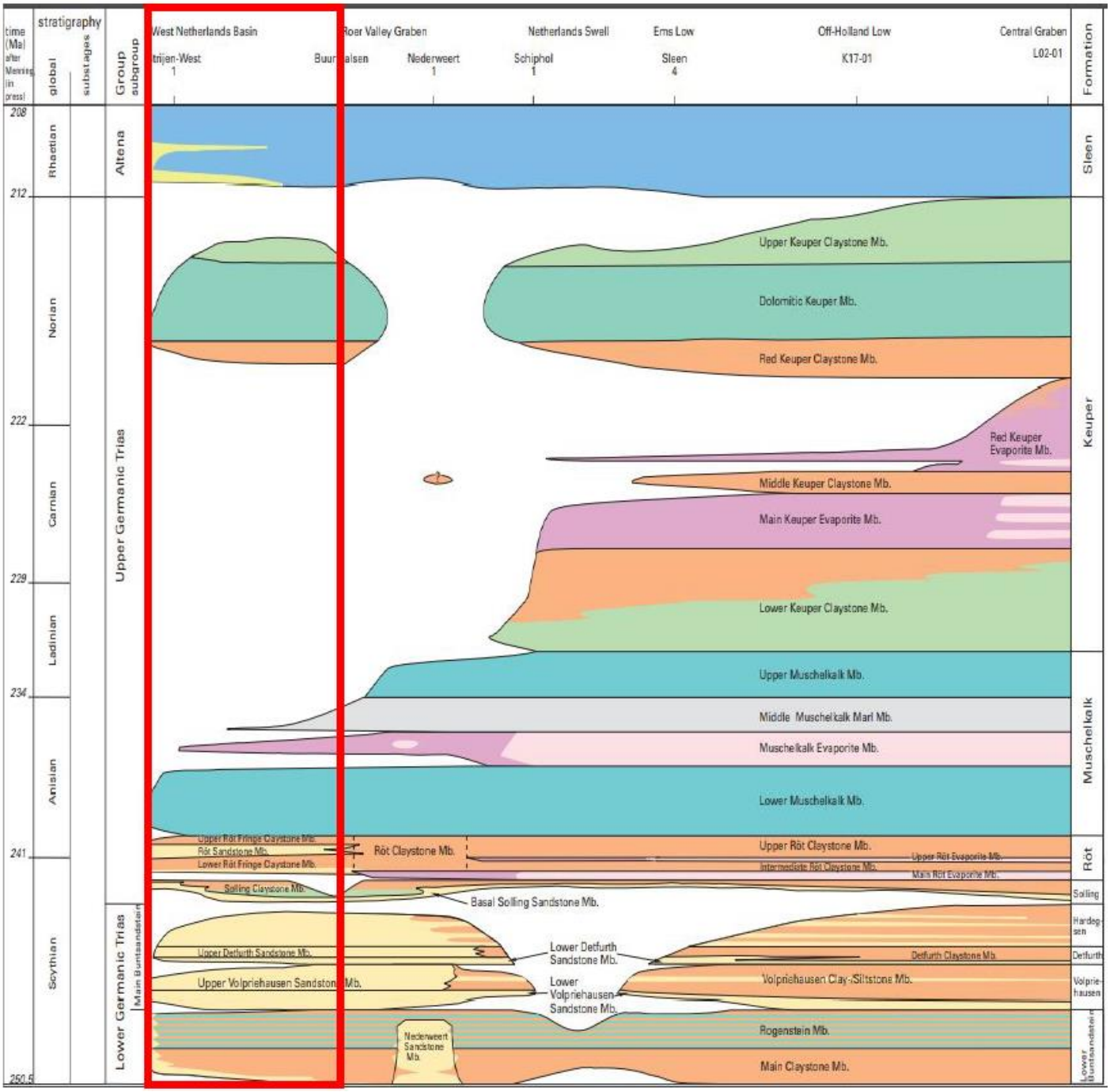

Figure 8. Stratigraphic column of the Triassic deposit, the red rectangle indicates the WNB after Van Adrichem Boogaert and Kouwe (1997).

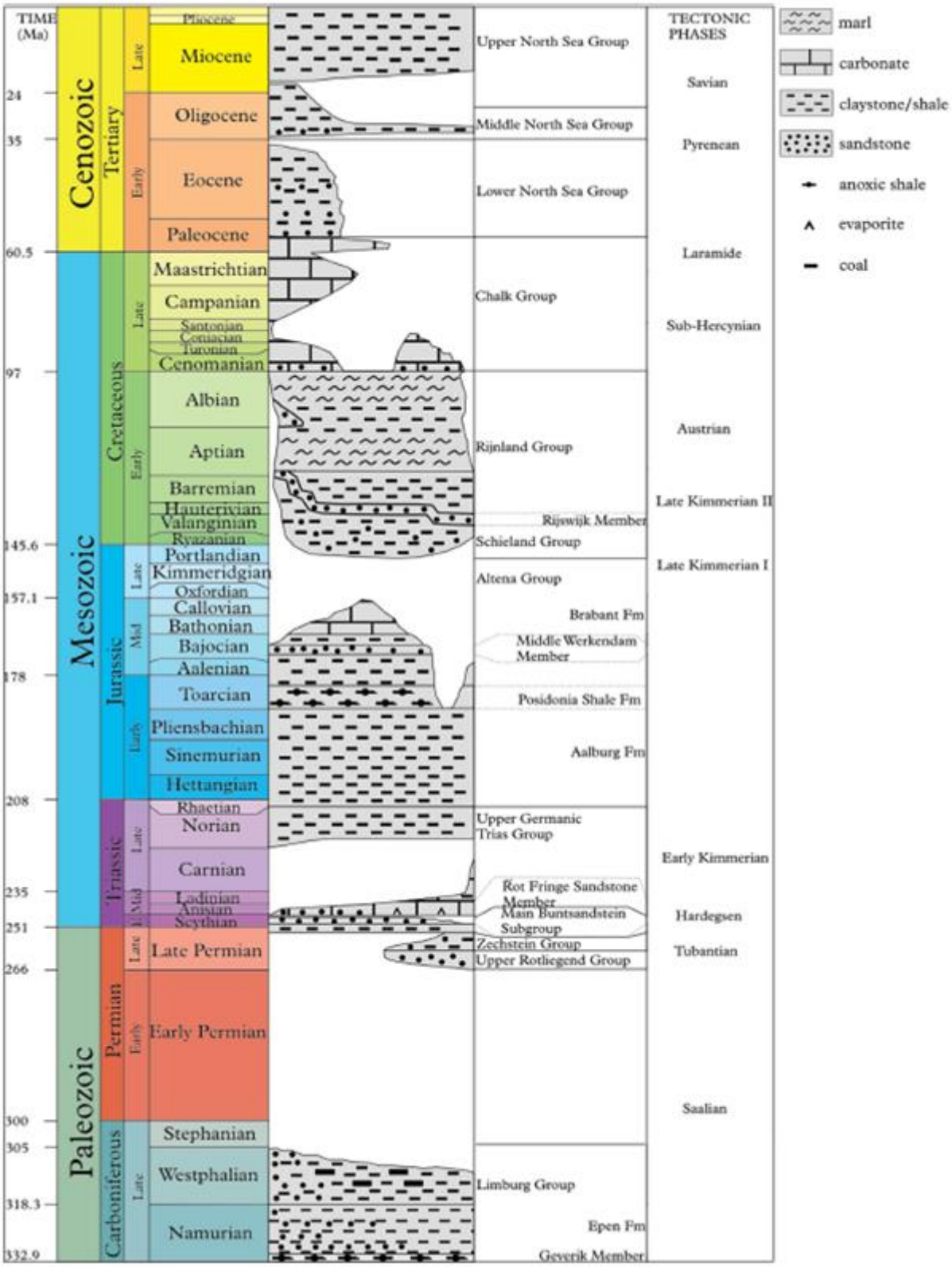

Figure 9. Geological time scale and lithostratigraphic column of the West Netherlands Basin (Van Balen et al., 2000)

This page is left blank intentionally

3 Geomechanics

3.1. The importance of stress knowledge

The Earth's stress is not only related to hazardous earthquakes but also related to all human-made activity that is reaching into the depth of the crust. During earthquakes, stresses are released by rupture and thus could lead to catastrophic events for humans. Also, the fracture aperture is affected by far-field stresses (Agheshlui et al., 2018). Human has also taken advantages of the knowledge about the Earth's stress to protect themselves against the collapse of tunnels. Thus, the primary concern regarding subsurface activities becomes safety and stability (Fuchs and Müller, 2001). Therefore, knowledge of the orientation and magnitudes of the principal stresses is vital to create a comprehensive geomechanical model.

3.1.1. Borehole failure features

Earth's crust contains significant distributed faults and fractures at various scales and orientations. Those faults and fractures developed at multiple time scales during the history of the formation's creation (Zoback, 2010). Fractures in a rock are formed as a result of stresses due to gravity and tectonic forces in the uppermost Earth's crust. When rocks subsided from the surface to depths of several kilometers, they experience a different state of stress (Bertotti et al., 2017; Zoback, 2010). Different depth and time of subsidence could have different stresses in terms of magnitude and orientation of the principal stresses. Thus, those factors then controlling the occurrence of fracturing (Zoback, 2010).

Mode I fractures oriented perpendicular to the least principal stress (Rouchet, 1981; Zoback, 2010). In the case of S_{hmin} (minimum horizontal stress) becomes the least principal stress (Normal and Strike-slip fault regime), the Mode I fractures would propagate in the SHMax – Sv plane (Zoback, 2010). Otherwise, if the least principal stress is Sv (vertical stress), then Mode I fractures would propagate in the SHMax – Shmin plane. The knowledge of how and where the fractures would propagate is essential before doing hydraulic fracturing in the formations.

On the other hand, drilling a borehole would cause stress to concentrate around the wellbore. In a vertical well, compressive stress is concentrated at the azimuth of (S_{hmin}). On the contrary, high tension stress is accumulated in the direction of SHMax (Zoback, 2010). These stress concentrations around vertical wells (Figure 10) would result in borehole failure (breakouts, and drilling-induced fractures). Compressive borehole failure would cause formation breakouts at the azimuth of S_{hmin} (Bell et al., 1979; Zoback et al., 1985). On the other hand, drilling-induced fractures caused by tensile stresses formed at the azimuth of SHMax (Zoback, 2010).

The presence of borehole failure features is beneficial, among other things, to determine the distribution and orientation of fractures and faults at depth as well as determining the magnitudes of the maximum horizontal stress (Zoback, 2010). Some studies from Bell et al. (1979) and Cox (1970) resulted in the conclusion that the azimuth of the borehole breakouts is coherent with the orientation of the stress tensor derived from nearby earthquake's focal mechanism. Borehole failure can be identified by using image logging tools, four-arm caliper tools, and sonic logging tools. Furthermore, borehole failure has become one of the primary resources to compose the world stress map (WSM). The WSM provides data on the present-day crustal stress field. It aims to quantify the stress tensor

components to characterize the crustal stress patterns and the sources of these stresses (Heidbach et al., 2019).

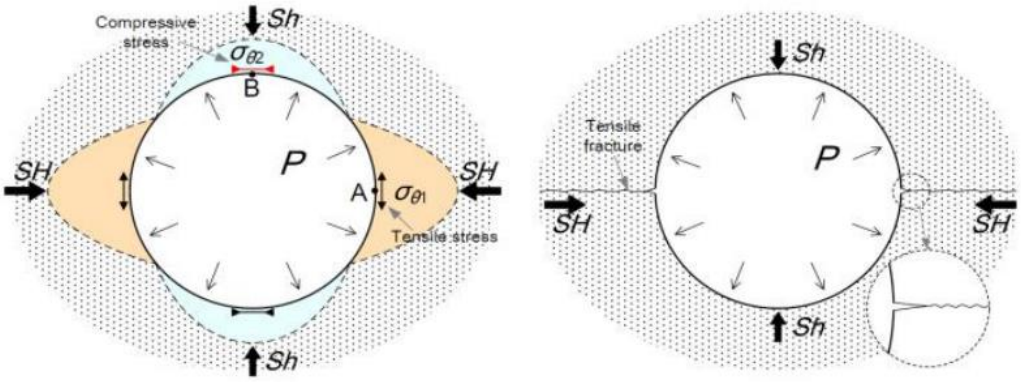

Figure 10. A schematic view of borehole failure in a vertical well, after Azit et al. (2016)

3.1.2. Faults and fractures reactivation

There is a theory indicating that Earth's crust is in a near-critical state (Heffer, 2015; Zoback, 2010). Therefore, activities such as fluid injection in hydrocarbon and geothermal industry could induce earthquakes. This process is initiated when pore pressure in the reservoir increases and frictional resistance of fault reduces, followed by releasing elastic energy already stored in the surrounding rocks in the form of earthquakes (Zoback and Gorelick, 2012).

Fault re-activation is a frictional process and can be defined as a ratio of shear to normal stress (Fuchs and Müller, 2001). If the ratio ($r = \tau/\sigma n$) exceeds the frictional strength coefficient, mostly between values of 0.6 and 1.0, the fault is considered to be critically stressed (Zoback, 2010).

Both normal and shear stress can be calculated in different locations along the fault plane by using equations 1 and 2. It is, therefore, possible to graphically evaluate if faults or fractures are in a stable or critically-stressed condition by using a Mohr-Coulomb failure criterion in combination with the Mohr circles. Mohr-Coulomb is a function of confining stress and the ranges of strength values for particular rock types (Zoback, 2010).

The mohr-Columb circle represents the value of the shear stress (τ), and effective normal stress (σn) on the fault and fracture when it experienced the failure process in terms of principal stresses $\sigma 1$ and $\sigma 3$, at an angle of β (the angle between the fault/fracture normal and $\sigma 1$). The relationship between shear stress and effective normal stress is shown in two equations below.

$$\tau = 0.5(\sigma_1 - \sigma_3)\sin 2\beta \qquad (1)$$

$$\sigma_n = 0.5(\sigma_1 + \sigma_3) + 0.5\,(\sigma_1 - \sigma_3)cos\,2\beta \qquad (2)$$

It is also stated that slip occurs when shear stress (τ) equals or exceeds the frictional sliding resistance, called the failure shear stress (τf). Hence the tendency for fault slip is given by equation 3 (Jaeger et al., 2009). Note that C, μ, $\sigma_{ft,}$ and P_p represent cohesion of the rock, coefficient of internal friction, total stress normal to the failure plane, and pore pressure, respectively.

$$\tau \geq \tau f = C + \mu(\sigma_{ft} - P_p) \qquad (3)$$

As seen from equation 3, the slip tendency is also affected by the pore pressure near the fault plane. Figure 11 illustrates the situation when pore pressure elevates from the initial state, the Mohr circle shifts to the left (Circle 1) and thus increasing the chance of failure. On the other hand, when pore pressure decreases, the Mohr circle shifts to the right (Circle 2) and decreasing the possibility of failure. Therefore, All allowable stress states in the Mohr circle are stresses that do not touch the failure envelope. Otherwise, rock is at failure state when stresses touch the failure envelope (Circle 3).

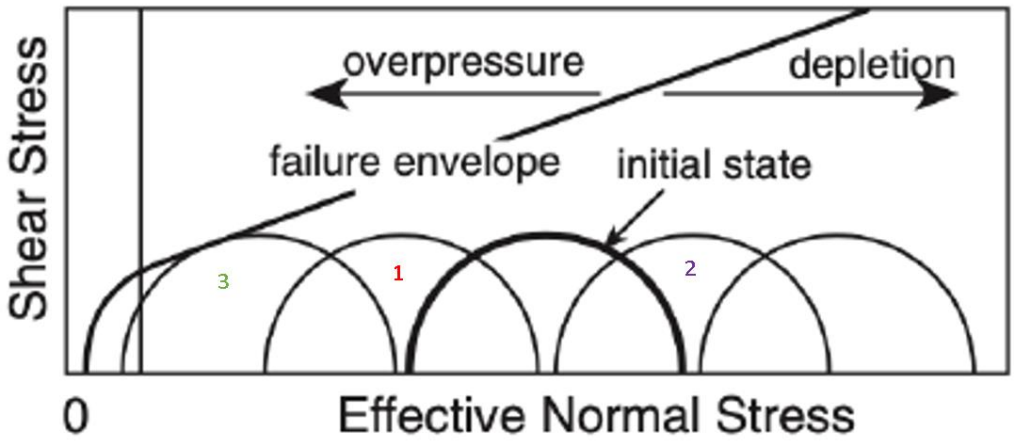

Figure 11. The Mohr circle diagram depicts the effects of pore pressure (Hillis, 2000)

3.2. Geomechanics

3.2.1. Stress

Stresses working in a body at a particular depth are described as a second-rank tensor (4), with nine components (Zoback, 2010). The subscripts are shown in each matrix component below represents the axis of an arbitrary cartesian coordinate system and the direction of the acting stresses.

$$S = \begin{bmatrix} S_{11} & S_{12} & S_{13} \\ S_{21} & S_{22} & S_{23} \\ S_{22} & S_{32} & S_{33} \end{bmatrix} \quad (4)$$

The component of the stress in one coordinate system can be evaluated in any other coordinate system through tensor transformation. Once the in-situ stress field is defined in a geographic coordinate system, it is possible to derive the stress state, among others, in a wellbore or fault coordinate system (Zoback, 2010). Furthermore, one can also choose to define the state of stress in a principal coordinate system, in which the off-diagonal stress tensor components vanish. The remaining three components are the three normal stresses (S_1, S_2, S_3). They are perpendicular to each other, and thus, their magnitudes and orientations describe the stress state (Heidbach et al., 2019; Zoback et al., 2003).

Furthermore, those principal stresses represent the maximum (the greatest), the intermediate, and the minimum (the least) principal stress, respectively. Those principal stresses are acting normally on a principal plane. The surface of the Earth is described as one of the principal planes since it has contact with the fluid (either water or air), which does not support shear stresses. The stress tensor in the principal plane coordinate system can be found in the form of the matrix below.

$$S' = \begin{bmatrix} S_1 & 0 & 0 \\ 0 & S_2 & 0 \\ 0 & 0 & S_3 \end{bmatrix} \quad (5)$$

Four parameters are needed to describe the state of stress at a certain depth: three principal stresses magnitudes and one stress orientation. Assuming that the vertical stress (S_V) is one of the three principal stresses that are acting normal to the surface of the Earth while the other two principal stresses being in a horizontal plane (Heidbach et al., 2019; Zoback, 2010). Vertical stress is a gravitational loading that is caused by the weight of the overburden, while SHMax and Shmin are maximum and minimum horizontal principal stress, respectively. The S_V can be calculated from the thickness and bulk density of the overburden by using equation 6, the remaining unknowns magnitudes of horizontal stresses (SHMax& Shmin) can be calculated by using equations 7 and 8.

$$S_v = \int_0^z \rho(z) g dz = \rho g z \quad (6)$$

where:

- Sv is vertical stress (Pa)
- ρ is the density of the overburden rock (kg/m^3)
- g is gravitational acceleration (m/s^2)
- z is the depth from the surface to a particular depth (m)

The calculation of the horizontal stresses use equations 7 and 8 (Bertotti et al., 2017)

$$S_{hmin} = \frac{v}{1-v}(S_v - P_p) + \frac{v}{1-v}S_{tect} \quad (7)$$

$$S_{Hmax} = \frac{v}{1-v}(S_v - P_p) + S_{tect} \quad (8)$$

where:

- SHMax is maximum horizontal stress (Pa)
- Shmin is minimum horizontal stress (Pa)
- v is Poisson's ratio
- S_{tect} is tectonic stress (Pa)
- P_p is pore pressure (Pa)

Pore pressure is described as a scalar hydraulic potential acting within an interconnected pore space measured to Earth's surface (Zoback, 2010). The value of pore pressure at depth is usually linked to normal hydrostatic pressure (NHP) and increases with depth. Albeit, in a more confining pressure, pore pressure could exceed hydrostatic values, and thus this condition is called overpressure. NHP can be calculated by using equation 9.

$$P_{hydro} = \int_0^z \rho(w) g dz = \rho_w g z_w \quad (9)$$

The concept of effective stress was first introduced by Terzaghi (1925) in the subject of soil mechanics. It is stated that soil or a saturated rock is controlled by the effective stresses, the differences between externally applied stresses, and internal pore pressure. The pore pressure only influences the normal stress components (σ_1, σ_2, σ_3) and not the shear stress components (Zoback, 2010). Equation 10 shows the relationship between effective stress and pore pressure

$$\sigma = S - P_p \quad (10)$$

where:

- σ is effective stress (can be horizontal or vertical)

- S is total normal stress (S_1, S_2, and S_3)
- P_p is pore pressure

3.2.2. Effective stress ratio

The ratio between the effective horizontal stress and vertical stress is called the effective stress ratio (ESR). ESR becomes one of the parameters that need to be calculated and used in the geomechanical model in JewelSuite. The effective stress ratio formula based on the minimum and maximum horizontal stress is shown in equations 11 and 12, respectively (van der Zee et al. 2011).

$$ESR_{min} = \frac{S_{hmin} - P_p}{S_v - P_p} = \frac{\sigma_{hmin}}{\sigma_v} \quad (11)$$

$$ESR_{min} = \frac{S_{Hmax} - P_p}{S_v - P_p} = \frac{\sigma_{Hmax}}{\sigma_v} \quad (12)$$

3.3. The stress regime

When the relative magnitudes of the three principal stresses are known, the stress regime can be assigned. Table 1 shows the tectonic stress regime defined with three principal stresses based on faulting theory by Anderson (1951). The magnitude of the vertical (overburden) stress and the maximum and minimum horizontal stresses determine the fault regime. In a normal fault regime (NF), the $S_1 \approx S_v$, gravity drives normal faulting, and it could also cause a fault to slip when the least horizontal principal stress is the least/lowest principal stress (S_v > SHMax > Shmin).

In a very compressive environment, the maximum principal stress (S_1) will always be SHMax, and both principal horizontal stresses will exceed the principal vertical stress (SHMax > Shmin > S_v). This condition would lead to a reverse fault regime. However, the strike-slip fault regime represents an intermediate state of stress (SHMax > Sv > Shmin) when the principal vertical stress (Sv) ≈ S_2. Also, the strike-slip fault regime occurs when SHMax and Shmin has a significant difference in magnitude (Zoback et al., 2003).

Table 1. Stress faulting regime

Stress regime	S_1	S_2	S_3
Normal fault	Sv	SHMax	Shmin
Strike-slip fault	SHMax	Sv	Shmin
Reverse fault	SHMax	Shmin	Sv

This page is left blank intentionally

4 Methodology & Datasets

4.1. Workflow overview

In order to make a 3D geomechanical model in the West Netherlands Basin (WNB), the existing seismic and well logs data will be used. The general workflow for this study is illustrated in Figure 12.

Figure 12. The workflow of geomechanical modeling

The proposed of geomechanical study will include the following tasks:

1. The first step is collecting geological information from the literature. The important data, such as regional geology, tectonic history, and sedimentary rocks, will be used to reconstruct the initial insight of the study area.

2. The next step is interpreting seismic data. Horizons and faults are the product of this process. Several procedures, such as seismic well-tie and velocity modeling, are carried out to create a better depth model. Those processes are done by using the Petrel E&P Software Platform.

3. A 3-D finite element modeling is a step before simulating the 3D geomechanical model. A software of JewelSuite 2017.4 Subsurface Modeling is used to create a geometry of a geomechanical model with the horizons and faults from the seismic interpretation as the primary input. Seven stratigraphic units have been included in this model.

4. Create a 1-D geomechanical model from existing wells that intersect with the Triassic formation. The 1D geomechanical model is intended to provide preliminary information and constraint on the current stress field. A range of wells data will be selected based on their relevance and well log data coverage.

5. Perform 3D finite element analysis for some tectonic scenarios and calculate changes and variations of in-situ stress and assess the impact on the possibility of fault reactivation.

4.2. Seismic interpretation

The seismic interpretation is performed in the time domain by using the Petrel E&P Software Platform. Furthermore, the interpretation will be converted into a depth domain. In general, the seismic interpretation is made by initially performing well to seismic integration by investigating the acoustic character of the horizons. The seismic acoustic character of each horizon is used as a guidance and lithology marker in horizon interpretation.

Furthermore, an investigation of the acoustic character of the horizons from density and sonic logs is done. The seismic and well data are loaded into Petrel for horizons and faults interpretation. In this process, selected wells will be integrated into the seismic data. Since the seismic data is in the time domain, a time-depth conversion is required to create a structural depth map. The workflow for seismic interpretation is illustrated in Figure 13.

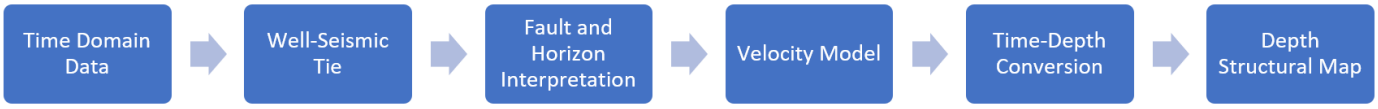

Figure 13. Seismic interpretation workflow

4.2.1. Seismic well-tie

Well logs measurement such as gamma-ray, resistivity, sonic and density logs are recorded in the depth domain. Meanwhile, seismic measurement and interpretation are in the time domain. In order to transform well logs measurement from depth to time, or to transform the seismic interpretation from time to depth, a time-depth relationship needs to be established. The first step is importing the well data that contains information such as well tops and well logs data. The next process is generating the synthetic seismograms. Synthetics are obtained from sonic and density logs from which an acoustic impedance can be calculated. There are often gaps measurements in the sonic log which lead to a poor tie. In order to enhance the well tie, the sonic log used in this process is calibrated with well shoot data from the check shot survey.

A synthetic seismogram is generated from primary reflectivity. Reflectivity is caused by changes in impedance. Since impedance is produced from velocity (VP) and bulk density (ρ), a primary reflectivity can be generated from the slowness (DT) and bulk density curves.

The last step is convolving the primary reflectivity with Butterworth wavelets to give the appearance of the seismic. Butterworth is chosen as it provides the most suitable representative synthetic seismogram. The result of the synthetic seismogram can be compared directly to the seismic. A good calibrated sonic logs and appropriate wavelets will result in a good time-depth relationship that means a good tie between the seismic and the borehole. Once this process is done, the well and its attributes will appear and attach to the seismic display. Prior to fault and horizon interpretation, the manual inspection is done to check whether the well tops are fitted with its reflectivity responses. This is done to avoid misinterpreted the horizon zone.

4.2.2. Velocity model

In order to convert the faults and horizons mapped in time to depth, a velocity model is generated based on velocity interval from depth marker and horizon time by using a layer-cake model. The interpolation method used a “distance weighted” approach. Therefore, the velocity interval for each horizon zone is calculated by equation 13.

$$V_{int} = 2\frac{Z_{top} - Z_{base}}{TWT_{top} - TWT_{base}} \quad (13)$$

The estimated interval velocities are then used to create a velocity model in Petrel software. Furthermore, the time domain can be converted into a true vertical depth (TVD) domain in Petrel. Mostly, the estimated difference in TVD depth for each top formation is below 30 m. This difference could be caused by time and depth variation that corresponds to each of the top formations.

4.2.3. Seismic data

The seismic data was a 3D on-shore time-migrated type. Well and seismic data in this project used the Rijksdriehoekstelsel New (RD New), the Netherlands national projection system. The well and seismic data located on the onshore are available in RD coordinate system; therefore, no coordinate transformation is needed. The data used in this study overlap with seismic data of L3NAM1990C from www.log.nl. The original seismic data was shared by the Applied Geology Research group-TU Delft regarding the study on the deep geothermal reservoir in De Lier Field.

The geometry of the geomechanical model is created from the geological horizons and faults interpretations from seismic data. Based on the location of the study, the seismic data is the 3D onshore seismic data located in De Lier field, southwest of the Netherlands. Figure 14 shows the seismic coverage in the study area.

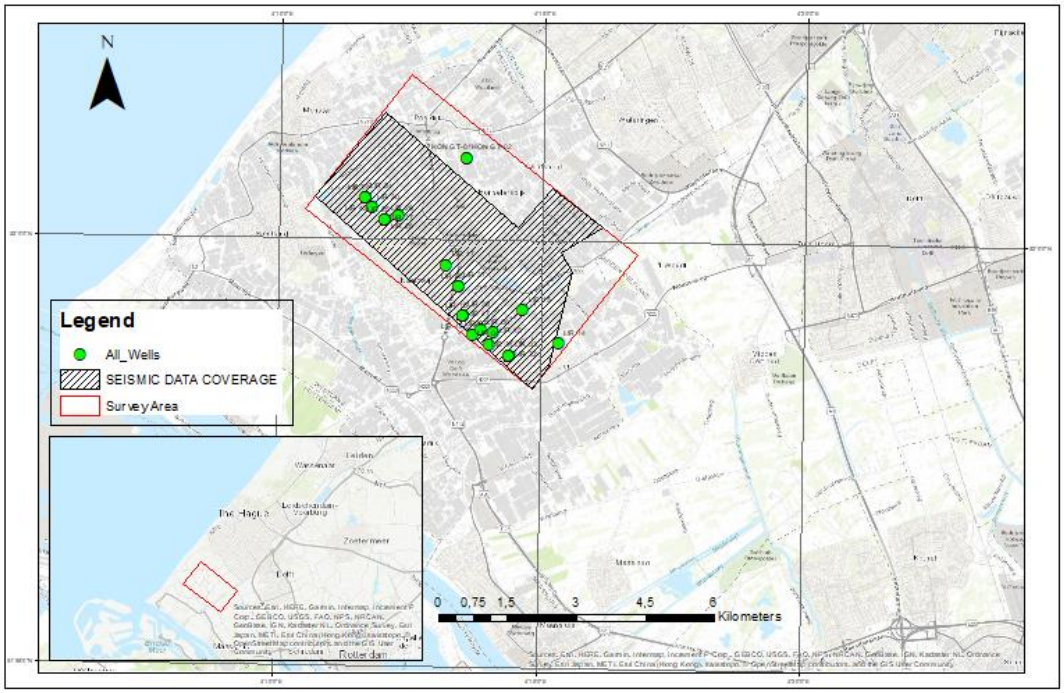

Figure 14. Wells and seismic survey area. Basemap source from ESRI-ArcGIS

The seismic parameters are presented in Table 2. The original seismic data has SEG polarity and phase convention. It means that an increase in impedance results in a positive amplitude and will be displayed in blue. A decrease in impedance occurs in negative amplitude and will be displayed in red color. Otherwise, a non-SEG polarity display will be displayed in reverse. An increase in impedance results in negative amplitude and will generally be shown in red color. A decrease in

impedance results in positive amplitude and will generally be displayed in blue color. However, the polarity display in this project has been flipped into non-SEG (normal European display convention).

4.3. Well data

There are twenty-eight (28) wells in the study area that are listed for the seismic interpretation process (Figure 14 and Appendix A). Those wells data are downloaded from the TNO website www.nlog.nl. Each well should contain several important data that later will be used in interpreting, such as well ID, coordinates, location, vertical datum, total depth, well markers, well deviation path, well logs, and reports. However, not all wells have complete data, yet the selection process is carried out to select which wells are useful for interpretation processes in the Petrel E&P Software Platform.

Table 2. Description of volume seismic data

Description	Value
Number of inlines	317
Number of crosslines	187
Inline length	3720.27 m
Inline interval	20 m
Crossline length	6320.04 m
Crossline interval	20 m
Inline rotation from North	38.59°

The criteria that are applied in the selection process, such as:

- the wells that intersect with the Triassic formation
- the wells that are in seismic coverage
- the wells that have bulk density log (RHOB) and slowness log (DT)
- the wells that have well-shot data

Further selection resulted that only two (wells) are suitable to be taken into interpretation processes. Most of the wells have incomplete logs data. Finally, LIR-45 and NLW-GT-01 are the wells that were used in the seismic interpretation process. NLW-GT-01 (Naaldwijk-GT-01) is a well that was completed for exploration of geothermal energy in the Triassic formation by Trias Westland B.V. It was completed in March 2018. Furthermore, horizons interpretation arranged from the shallower surface (base Upper North Sea Group) to the deeper surface (base Lower Germanic Triassic Group).

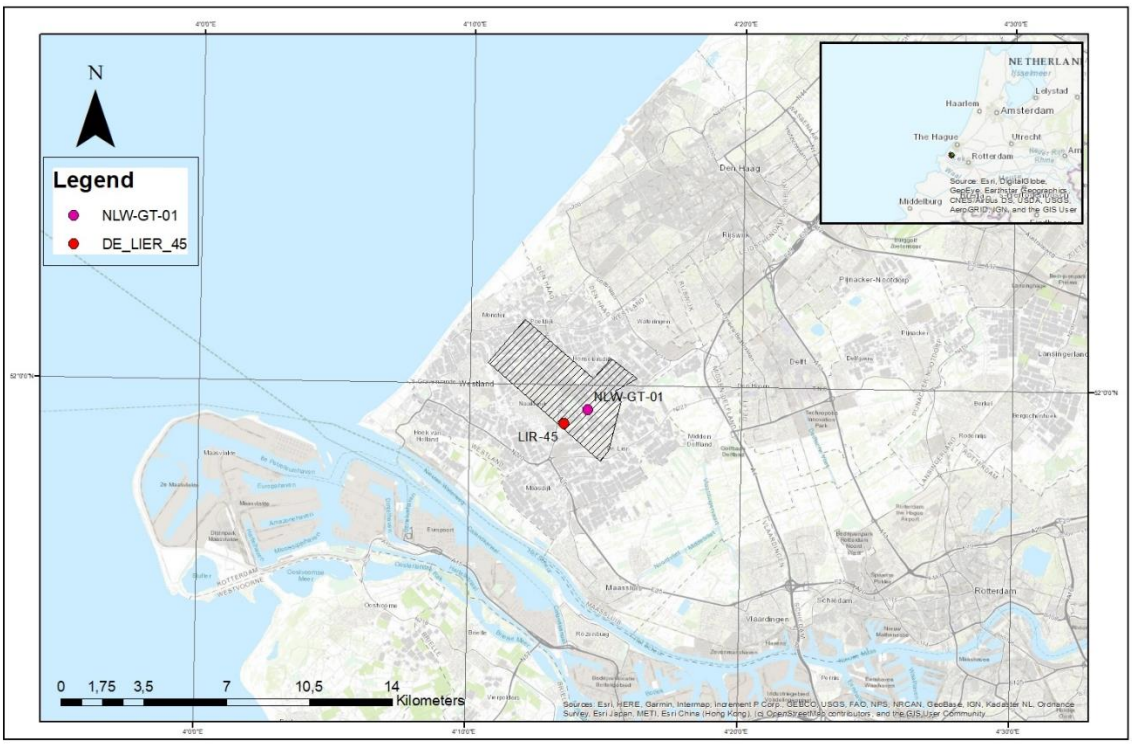

Figure 15. Selected wells for seismic interpretation. Basemap source from ESRI-ArcGIS

4.4. 3D structural modeling

Figure 16 shows the general workflow to build a 3D geomechanical model in the JewelSuite Subsurface Modeling software. The workflow contains several steps in sequence, such as stratigraphic modeling, fault modeling, 3D structural modeling, 3D mesh structural modeling, and 3D finite element mesh model.

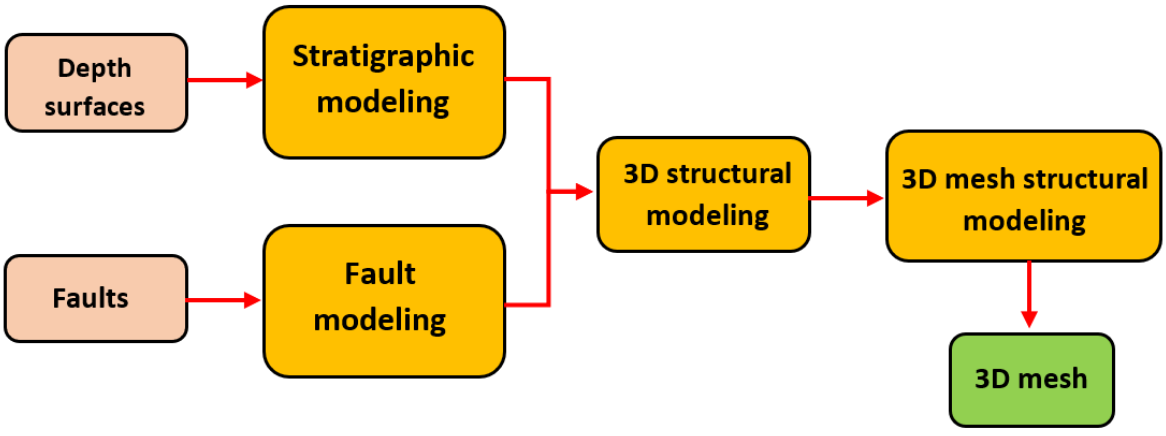

Figure 16. 3D geomechanical modeling workflow

It is necessary to define a representative volume that the main structural features are correctly incorporated. The shape of the structural model is in perfect cubic shape, regardless of the interpreted horizons initially. This process is intended to avoid any substantial numerical issues that

may appear related to the finite size of the model during the finite element simulations. Figure 17 shows the representative volume in modeling. The length is 5925 m, the width is 2250 m, and the depth is 4455 m.

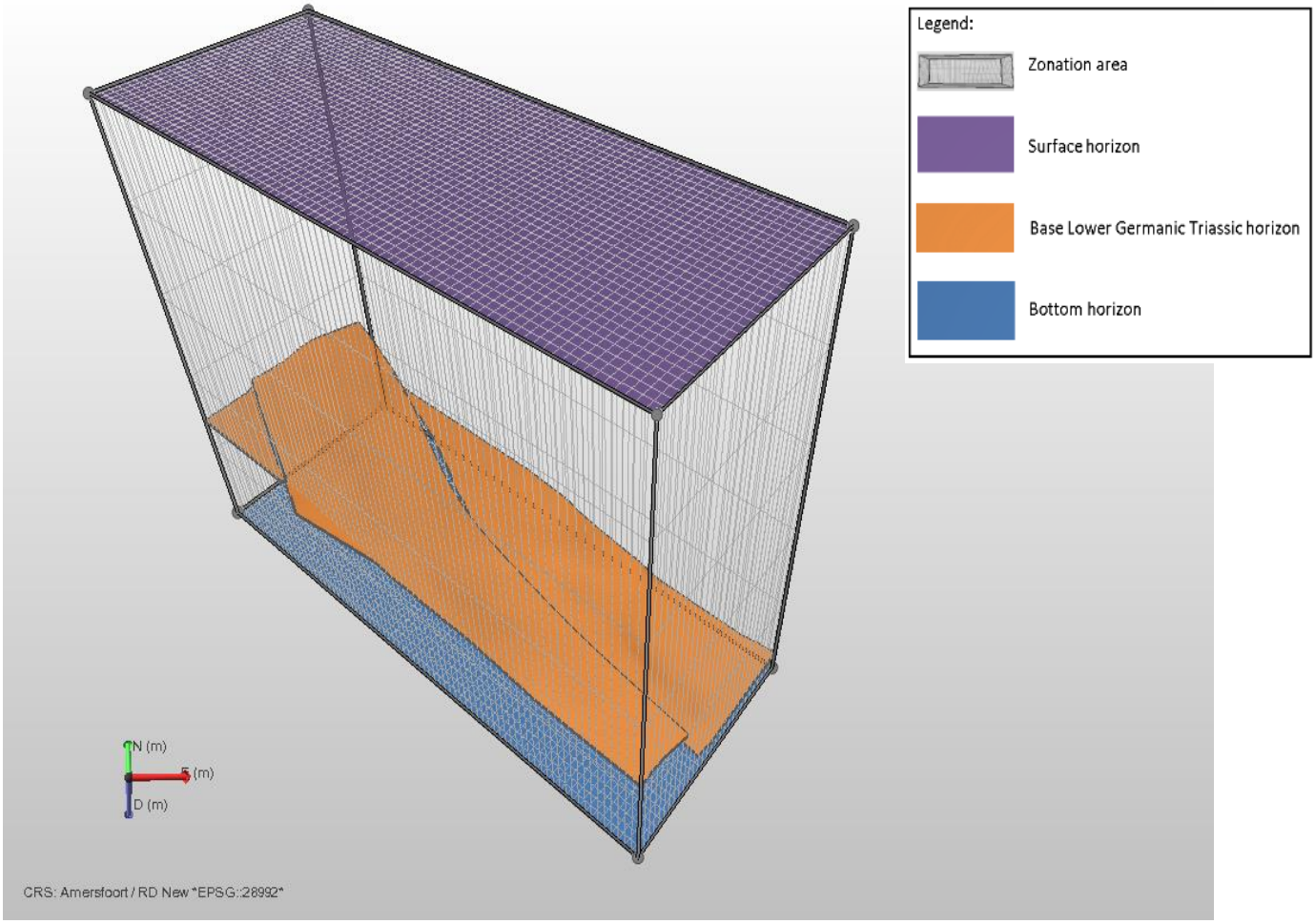

Figure 17. View of the modeling area

4.4.1. Fault and stratigraphic model

The process of creating the fault model is initiated by choosing the fault surfaces as the primary input. The next step is creating a fault model from existing fault surfaces that have been mapped earlier. The horizons and faults are imported from Petrel software and classified into two separate surface sets, horizon surface set that contains horizons only and fault surface set that includes faults only. A stratigraphic model requires these horizons as the primary input. Thus, a stratigraphic model will show different stratigraphic units and the order in which they occur (from top model to the bottom model)

Further editing in fault modeling is required to inspect if there are still intersections between two or more fault surfaces since fault interaction between two or more faults is not allowed to intercept each

other. The editing process is also intended to retract and extend the surface between the faults and intersected horizons.

Furthermore, all of those editing processes are done to ensure that all surfaces are in a watertight connection. It means that the surfaces not only do not intersect with each other but also there is no gap between them. The other model that needs to be created is a stratigraphic model. The stratigraphic model is the framework that contains the order and sequence of horizons. In this model, not only zones are defined but also the order in which the zones will be generated using a hierarchical approach. This model forms the basis for the next modeling steps where the actual horizon is assigned and modeled in the 3D structural model. The stratigraphic model, in this case, will use interpreted horizons as the primary input.

4.4.2. 3D mesh structural model

The 3D structural modeling consists of building the geological structure of the field in a three-dimensional volume by importing, editing, and interpreting relevant horizons surfaces, stratigraphic, and faults into a model. The input for the structural model consists of a set of horizons (2-D Point sets) and polylines to define the fault geometry. Polyline sets can be converted into a fault surface (tri-mesh) using the JewelSuite software. During this process, the intersection between the faults and the horizons can be cleared by using the horizon clean-up and fault cutoff line options.

The selected horizons were edited in such a way that the structural grid is formed of an optimally shaped finite element to limit computational errors. A total of seven horizons and three faults were selected and integrated into the model (Table 3).

A 3D mesh structural model is then developed after the 3D structural model is successfully created. A mesh model is created for each surface (both horizons and faults). However, to avoid generating a 3D structure with a very high level of detail, which would lead to a very large computational requirement for the finite element simulations, each horizon was coarsened to limit the size of the model. The typical separation distance between two nodes is around 200 m.

Furthermore, this process will determine the level of resolution and the computational time required while doing further geomechanical simulation in Abaqus/CAE software. The output of the 3D mesh structural model will have coarser tri-mesh shape surfaces.

Table 3. Layer and elements utilized to mesh the area study

	Before re-meshing			After re-meshing		
Layer name	Boundary nodes	Nodes element	Triangles	Boundary nodes	Nodes element	Triangles
Upper North Sea Group (NU)	301	805	1305	285	1660	3031
Lower North Sea Group (NL)	300	802	1300	284	1668	3048
Chalk Group (CK)	380	795	1289	331	1690	3043
Rijnland Group (KN)	417	880	1337	333	1714	3089
Schieland Group (SL)	391	802	1207	330	1716	3096
Altena Group (AT)	370	775	1174	324	1503	2676
Lower Germanic Triassic Group (RB)	374	765	1150	285	1660	3031

4.4.3. 3D mesh and finite element model

The generation of the 3D mesh model was based on the 3D mesh structural model. The structure of the geomechanical volume is made entirely watertight by connecting all horizons and faults so that no gap exists within the two or more surfaces. The structural modeling still requires some editing in the geometry of the horizons and faults to avoid the presence of inconsistent structures caused by the coarsening process, for instance, where consecutive horizons intersect each other.

The next step is constructing a 3-D Finite Element mesh by using Abaqus/CAE, a finite element software ABAQUS. The size and the number of finite elements are constrained by the number of horizons, faults, and the size of the tri-meshes. The mesh resolution was set to obtain an optimal resolution to perform numerical simulations while following the geometry imposed by the tri-meshes. All faults are integrated into the structural model. Therefore their geometries will constrain the construction of the FE mesh by generating a discontinuity at some locations.

Before simulation in Abaqus, the 3D mesh model needs to be populated with material properties (Table 4). Furthermore, simulation is carried out in two stages: First, an initialization stage in which the model is equilibrated with an applied realistic stress field. Second, the full simulation is prepared and run at multiple time steps. Material properties that need to be submitted are the boundary condition, the azimuth of SHMax, and the effective stress ratio between of SHMax/S_V and Shmin/S_V at particular depths.

The JewelSuite is using the geological stress convention while the Abaqus using engineering stress convention. Based on the geological stress convention, positive stress means compression, and negative stress is tension. Meanwhile, compressive stresses are negative in Abaqus, and tensional stresses are positive.

Table 4. Rock and material properties

Layer name	Density (kg/m^3)	Poisson's ratio	Young's modulus [GPa]
Upper North Sea Group (NU)	2050	0.3	2
Lower North Sea Group (NL)	2050	0.3	2
Chalk Group (CK)	2252	0.25	10
Rijnland Group (KN)	2360	0.25	16
Schieland Group (SL)	2470	0.25	16
Altena Group (AT)	2580	0.25	16
Lower Germanic Triassic Group (RB)	2650	0.25	19.3

The rock and material properties for all reservoir layers are taken from the NAM report (BV, 2013). Whereas, the value of Poisson's ratio and Young's modulus at Lower Germanic Triassic group was taken from the study conducted by Hinkofer (2017) concerning the geomechanical characterization of the Buntsandstein in the WNB. In addition, the density data are based on density well logs data. Some assumptions are made for Schieland and Altena Group, as the NAM report does not have such properties for those formations. In this case, those properties are being assumed similar to the properties of Rijnland Group.

4.5. Boundary condition

Figure 18 illustrates the displacement boundary conditions that hold the model in place. The nodes-set located at the bottom of the model is fixed in all three directions (x, y, and z); therefore, it cannot move to all directions. The nodes-set located at the outside is fixed in all horizontal directions but can move in the up-down (depth) direction.

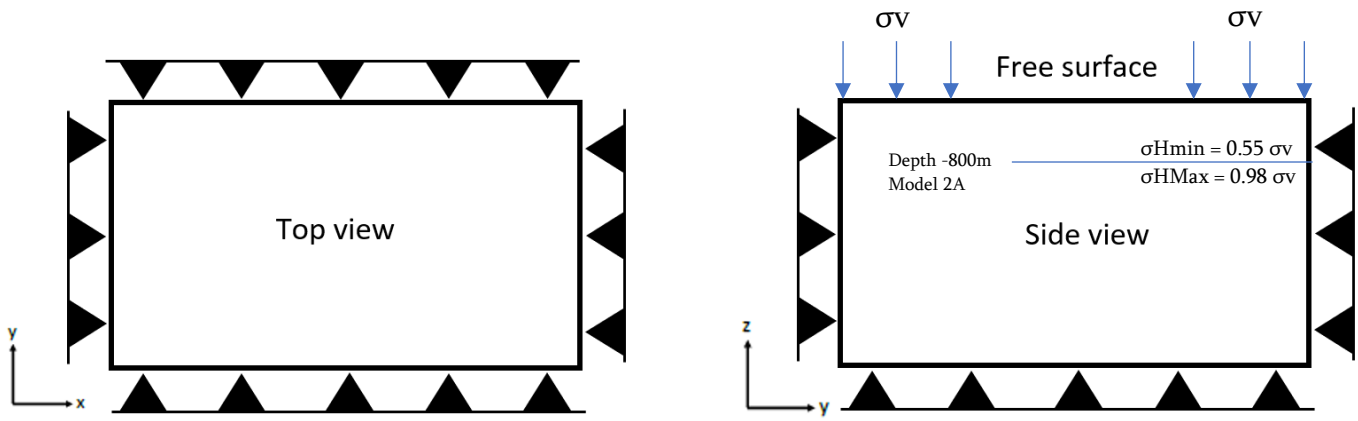

Figure 18. Boundary condition

4.6. Effective stress ratio

The effective stress ratio is one of the approaches to interpolate or extrapolate the magnitudes of SHMax and Shmin based on ESRmax and ESRmin. Therefore, one can estimate the magnitudes the principal stresses at depths shallower or deeper than measured depths. The ESR values are applied in JewelSuite by using both ESRmax and ESRmin at each corresponding depth. Equations 11 and 12 indicate how to find ESRmax and ESRmin. The value of ESRmax and ESRmin is presented in Table 5.

Furthermore, the Effective Stress Method calculates the maximum and minimum horizontal stresses from the continuous profile of the vertical stress (Sv). In addition, the value of pore pressure (Pp), in-situ measurement of Shmin, and determination of SHMax can also be as calibration points. That information is plotted in JewelSuite to generate interpreted trend lines. The final magnitude of SHMax and Shmin is then generated from this trend line (source: JewelSuite Manual Book). Since the initial stress tensor is known, Abaqus will establish geostatic equilibrium to calculate the stress to the whole of the mesh model.

Figure 19 shows both ESRmin and ESRmax and its corresponding depth. ESR values are categorized into four models, and those models later will be described in detail in Chapter 5 – part 1D Geomechanical model. It can be concluded from Figure 19 that effective stress ratio increases as the magnitude of tectonic stress increases. This is caused by the increasing value of the maximum and minimum horizontal stress. Also, the ESR value at the shallower depth is higher than the ESR at the deeper depth. It is because, at the shallower depth, the horizontal stresses have a more significant role than the vertical stress.

Table 5. Effective stress ratio and corresponding depth

Unit	Depth (m)	Model 1		Model 2A		Model 2B		Model 2C	
		ESRmin	*ESRmax*	*ESRmin*	*ESRmax*	*ESRmin*	*ESRmax*	*ESRmin*	*ESRmax*
NU	0	0.43	0.43	9.48	21.55	18.41	42.68	36.64	84.93
NU	200	0.43	0.43	1.46	2.85	2.38	5.28	4.59	10.14
NU	400	0.43	0.43	0.94	1.64	1.34	2.85	2.51	5.28
NL	500	0.43	0.43	0.85	1.42	1.15	2.41	2.13	4.39
NL	667	0.43	0.43	0.76	1.22	0.98	2.02	1.79	3.62
CK	800	0.33	0.33	0.55	0.98	0.68	1.64	1.21	2.95
CK	1158	0.33	0.33	0.47	0.74	0.52	1.16	0.88	1.99
KN	1400	0.33	0.33	0.45	0.70	0.49	1.07	0.83	1.81
KN	2068	0.33	0.33	0.41	0.58	0.41	0.82	0.65	1.31
SL	2200	0.33	0.33	0.41	0.56	0.40	0.79	0.64	1.25
SL	2451	0.33	0.33	0.39	0.53	0.38	0.73	0.59	1.12
AT	2600	0.33	0.33	0.39	0.52	0.37	0.71	0.58	1.08
AT	2876	0.33	0.33	0.38	0.50	0.36	0.67	0.56	1.00
RB	3200	0.33	0.33	0.38	0.48	0.35	0.63	0.53	0.92
RB	4300	0.33	0.33	0.35	0.39	0.37	0.46	0.42	0.59

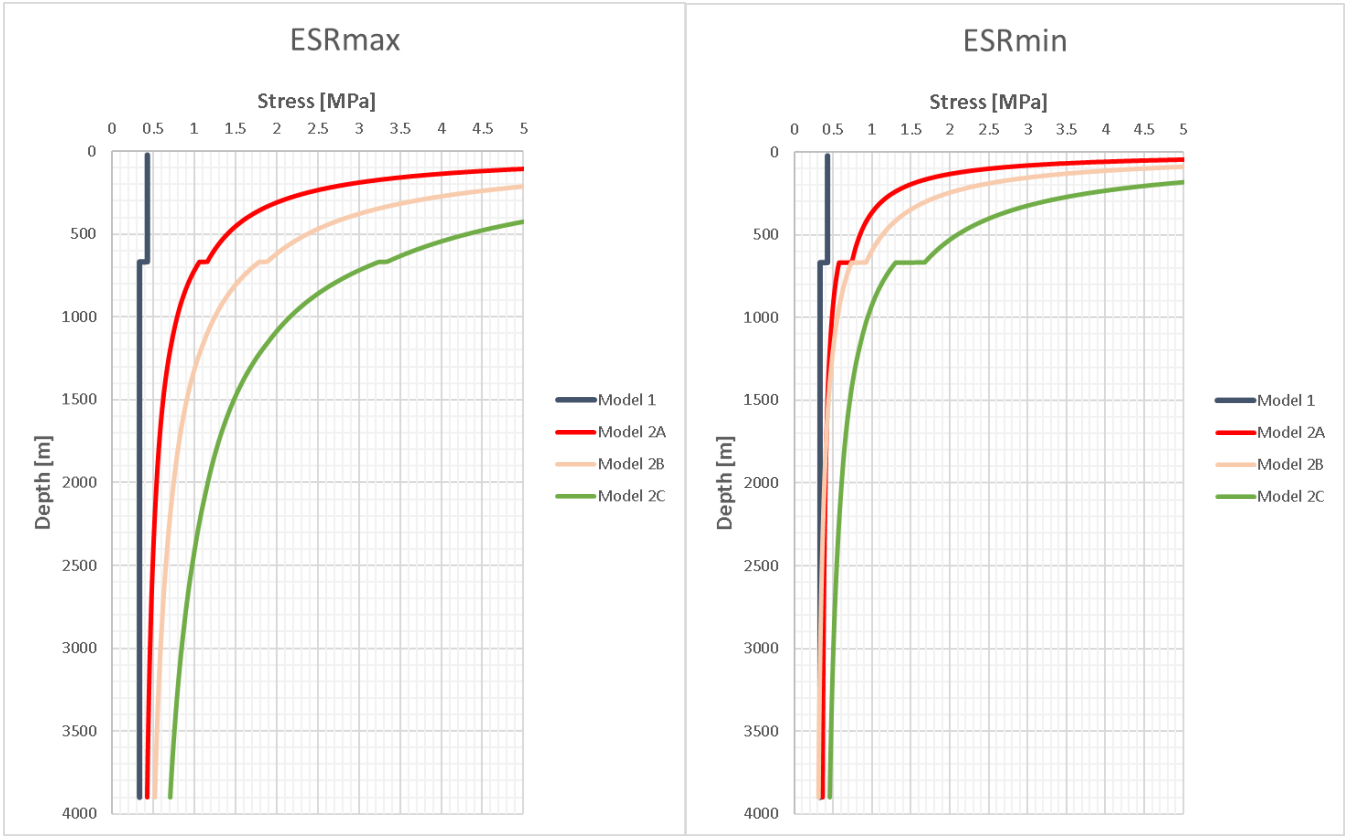

Figure 19. Comparison ESRmin and ESRmax values of all models

Model 1=Gravity only; Model 2A=tectonic 5 MPa; Model 2B=tectonic 10 MPa; Model 2C=tectonic 20MPa.

This page is left blank intentionally

5 Results & Discussions

5.1. Horizons and faults interpretation

5.1.1. Horizons interpretation

In this stage, although the target reservoir is in Triassic formation, the other horizons which are overlying the Triassic still need to be interpreted to provide reference horizons for the Triassic formation. Prior to interpretation processes, a crosscheck is done by comparing two-way travel time (TWT) from seismic and TWT from Digital Geological Model (DGM) provided by NLOG (Appendix B). DGM is a time map model of the Netherlands subsurface based on lithostratigraphic layers.

The information from those two models can be used to confirm the coherence between the seismic model and well-tie processing. During the processes, several arbitrary composite lines that intersect the top wells are created. Horizon interpretation processes are done by using a composite line with 16 or 32 increments. The five first horizons are the base Upper North Sea Group, base Lower North Sea Group, base Chalk Group, base Rijnland Group, and base Schieland Group. Those horizons have a clearer and visible amplitude response, while there are seven horizons, as indicated in Table 3 and Table 4.

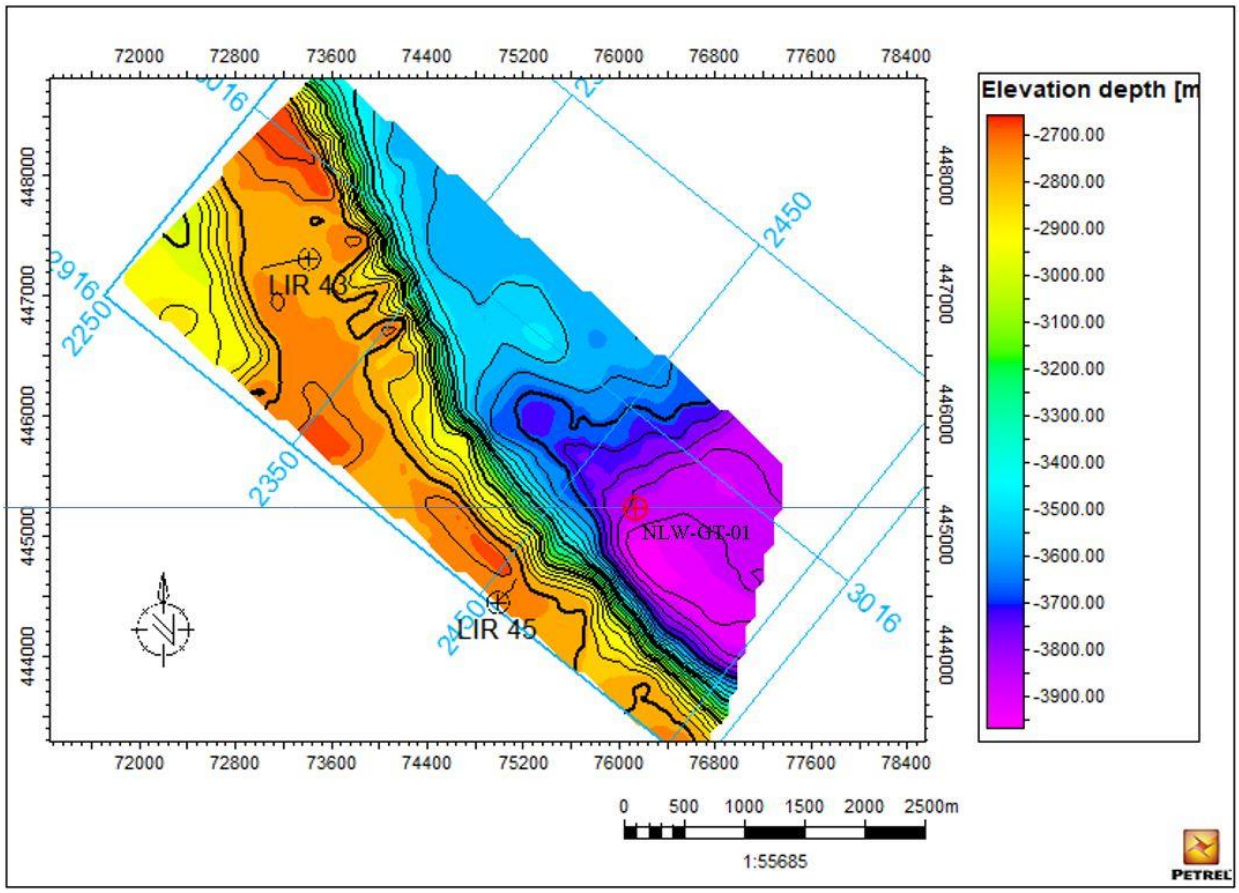

Figure 20. The depth map of the top Lower Germanic Triassic group

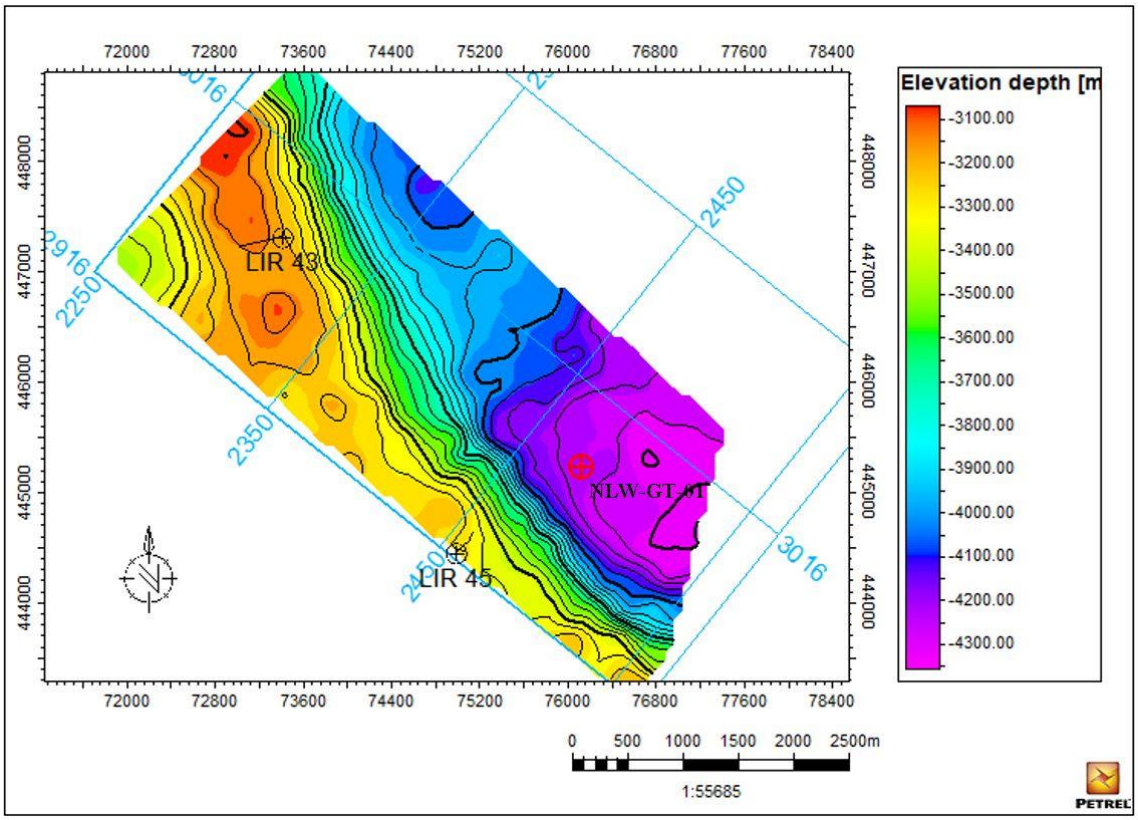

Figure 21. The depth map of the base Lower Germanic Triassic group

The two-way travel time map model (Appendix B) indicates that the Lower Germanic Triassic Group has TWT values ranged from 2162 ms - 2948 ms, while the seismic data (Appendix B) shows that the TWT value ranged from 2200 ms - 2300 ms. To be concluded, the seismic and well-tie process is reasonably good. In addition, the well tops from each well are located on the desired reflector. Thus, no correction is needed.

The amplitude response for the top of the Triassic succession (base Altena Group and base of the Lower Germanic Triassic) is not clear enough to interpret. That phenomenon could be caused by low impedance contrast. Though, in some parts, the reflectivity response still can be traced. Therefore, for simplicity, the Main Buntsandstein will be represented as the whole horizon of the Lower Germanic Triassic Group.

Figure 20 and Figure 21 show the horizon of the top and base Lower Germanic Triassic group, respectively, in the depth domain. The shallowest depth lies in -2700 m, while the deepest depth is -4300 m. Furthermore, it can be concluded that in general, well LIR-45 and LIR-43 are located at the up-thrown block, whereas well NLW-GT-01 is located at the down-thrown block. The depth of the Lower Germanic Triassic group at the top structural high, where LIR-45 is located is ranging from -2700 m to -3400 m. In addition, the Lower Germanic Triassic group in the down-thrown block, where NLW-GT-01 is situated, has a depth ranging from - 3500 m to - 4300 m. The abrupt changes in depth value that occurred to the NE and SW in the Lower Germanic Triassic group indicate the presence of the faults.

5.1.2. Faults interpretation

The fault interpretation is conducted by using a combination of seismic response and variance attribute. Therefore, the variance attribute can be used to isolate edges from the input data set. This process means isolating discontinuities in the horizontal continuity of amplitude. In order to give more certainty in fault interpretation, another amplitude versus offset (AVO) attributes is also added, such as 3D Edge Enhancement (Appendixes B). The faults are characterized by an apparent discontinuity in one or multiple horizons.

There are three normal faults observed. Two faults intersect with the targeted reservoir while the other one only intersects the Top Cretaceous formation. In addition, those two faults bounded the study area with the NW-SE orientation trend (Figure 22 and Figure 23). The up-thrown block and down-thrown block of the Lower Germanic Triassic group is characterized by significant fault offset that could reach up to 1000 m.

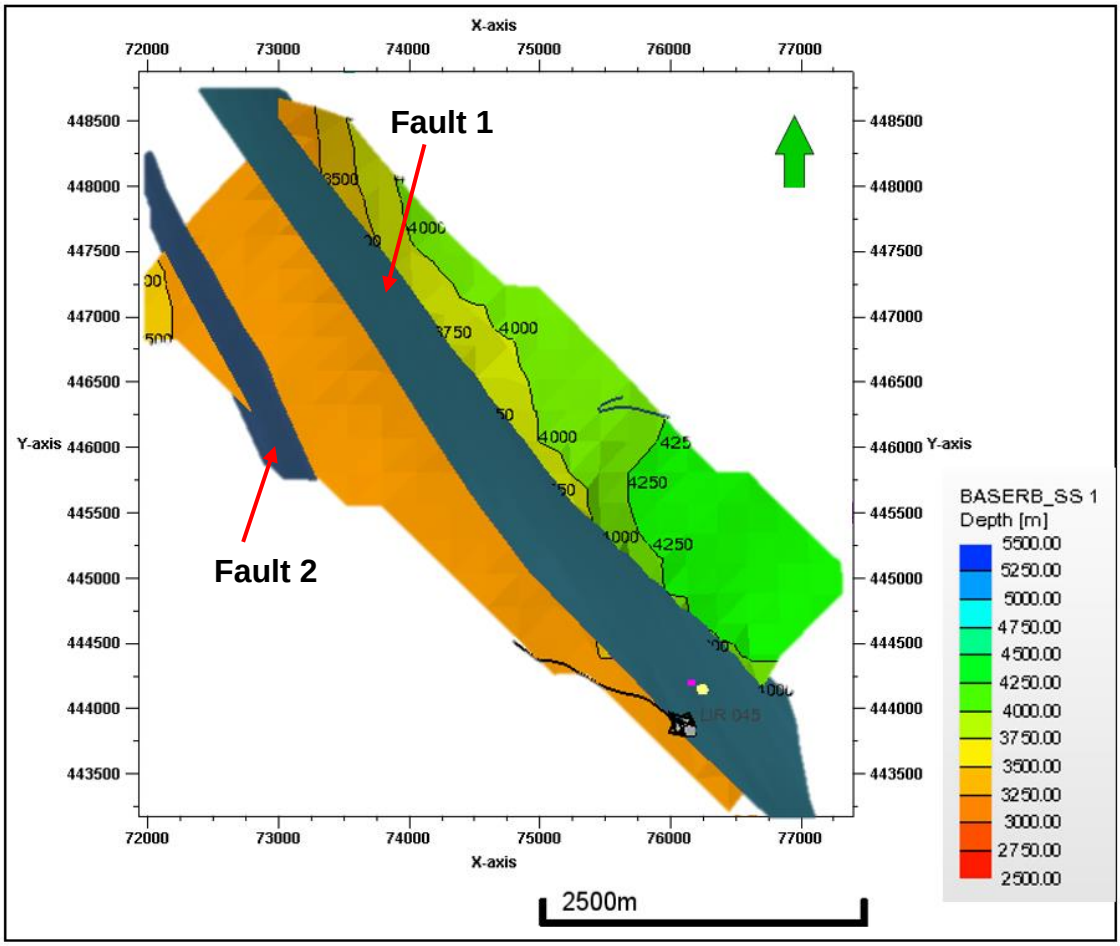

Figure 22. Fault map at the base Lower Germanic Triassic group (RB)

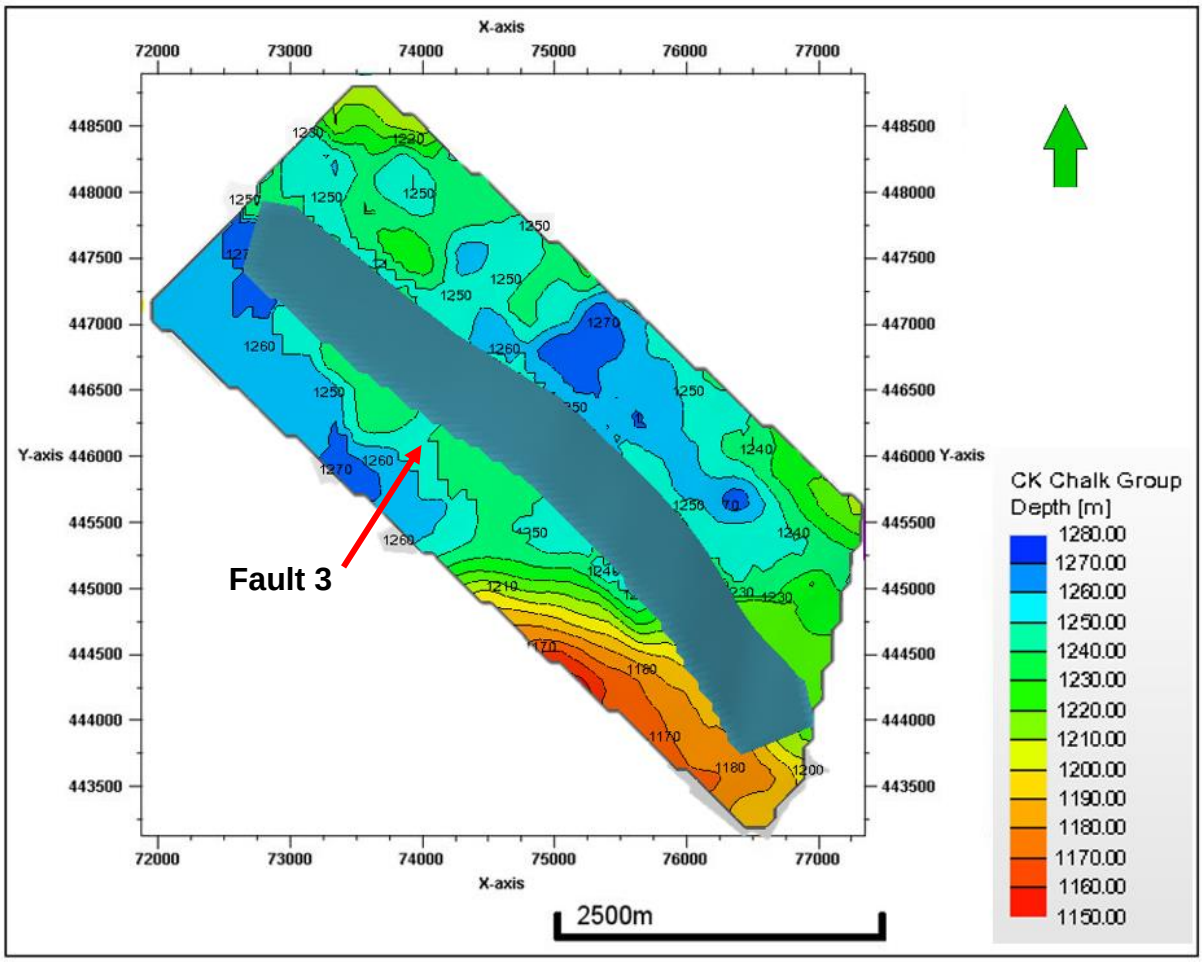

Figure 23. Fault map at the base Chalk group (CK)

5.2. Local stress orientation

The orientation of SHMax is required in the simulation in the Abaqus simulator. Therefore, a brief analysis is conducted to determine the SHMax orientation in the study area. The stress dataset was taken from the previous study conducted by Van Eijs and Dalfsen (2004), Mechelse (2017), and Rondeel and Everaars (1993). In addition, the stress database from WSM (World Stress Map) was also used in this study.

The stress orientation was mostly obtained from the presence of stress-induced borehole features such as borehole breakout (BO) and drilling-induced fracture (DIF). The SHMax orientation for the study area will be obtained from the nearest available stress field dataset, and those well are Q16-08, P18-A-06, and well Q13-07-S2, despite the fact that those wells are located outside of seismic coverage. Figure 24 shows that well P18-A-06 and Q13-07-S2 are located close to the NW-SE trending faults in the Lower Germanic Triassic Group.

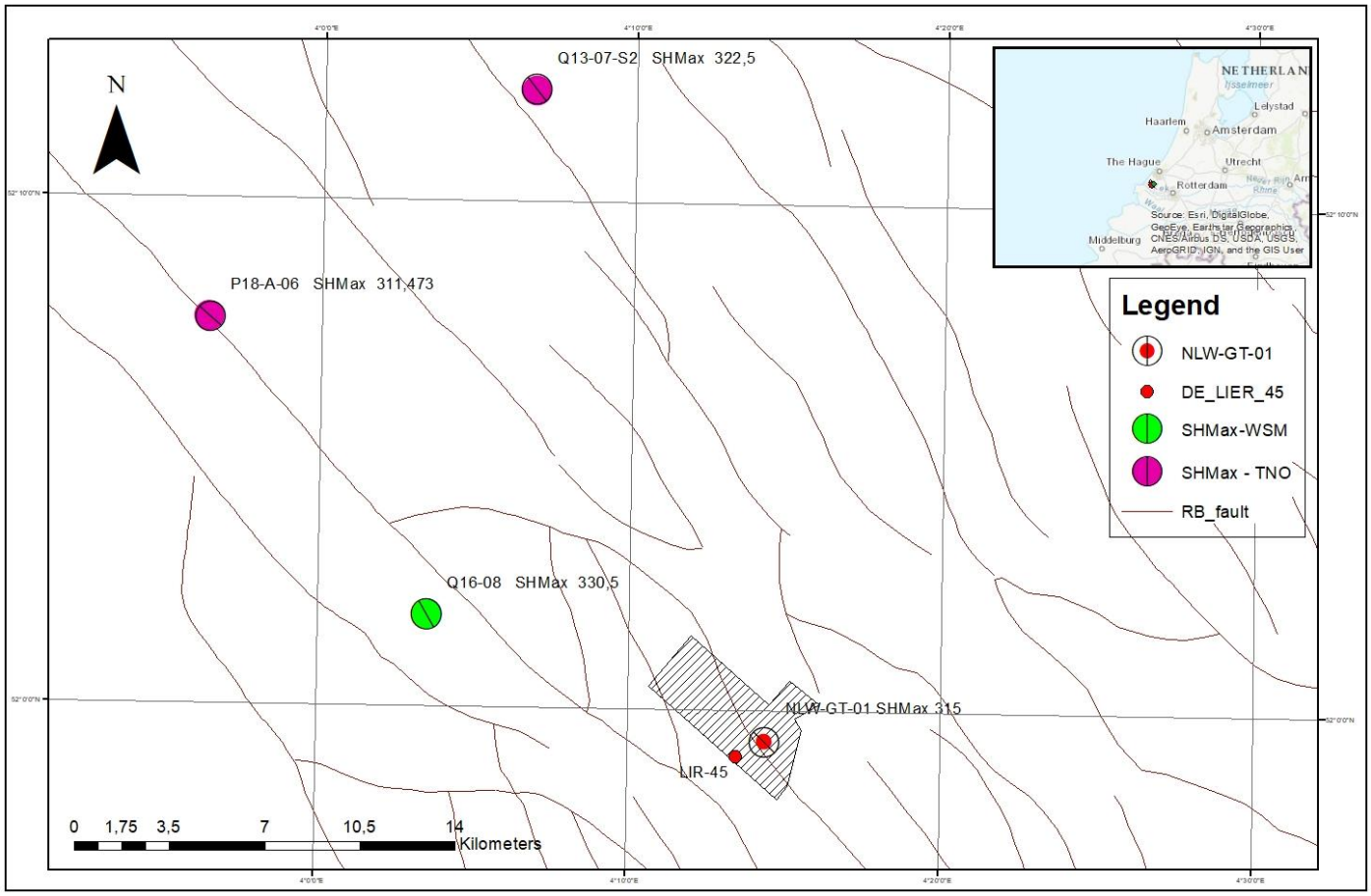

Figure 24. The location of wells that intersect with the Lower Germanic Triassic group

Well Q16-08 is located 1.3 km away to the nearest fault plane, while well P18-A-06 is 110 m away to the adjacent fault plane. The distance of well Q13-07-S2 is 1 km to the adjacent fault plane (Figure 24). Well P18-A-06 has the shortest distance to the fault plane. As previously mentioned, those wells are not taken from the exact study area. Those datasets are located 12.5 and 25 km away from LIR-45 and NLW-GT-01. Also, there is a recently submitted study by Applied Geology research group of TU Delft, about borehole failure features at well NLW-GT-01. The brief result of that study indicates an azimuth of 135°N or 315°N of SHMax orientation at well NLW-GT-01.

Figure 25 and Figure 26 show the distribution of borehole breakout (BO) and drilling induced fracture (DIF) with depth in well P18-A-06, Q13-07-S2, and Q16-08. Those figures show the SHMax orientation in the Lower Germanic Triassic Group.

In all wells, the borehole breakout (BO) and drilling-induced fracture (DIF) are indicated at different depths. Over the entire interval, it is depicted that the BO and DIF have a reasonably constant direction as all BO and DIF are oriented in the NW-SE direction. Also, well P18-A-06 (Figure 25) has a relatively spread out values. As a result, the numbers have a higher standard deviation compared to other wells. The SHMax direction value at Well Q16-08 (Figure 26) is close to the mean value. As a result, the numbers have a lower standard deviation compared to other wells.

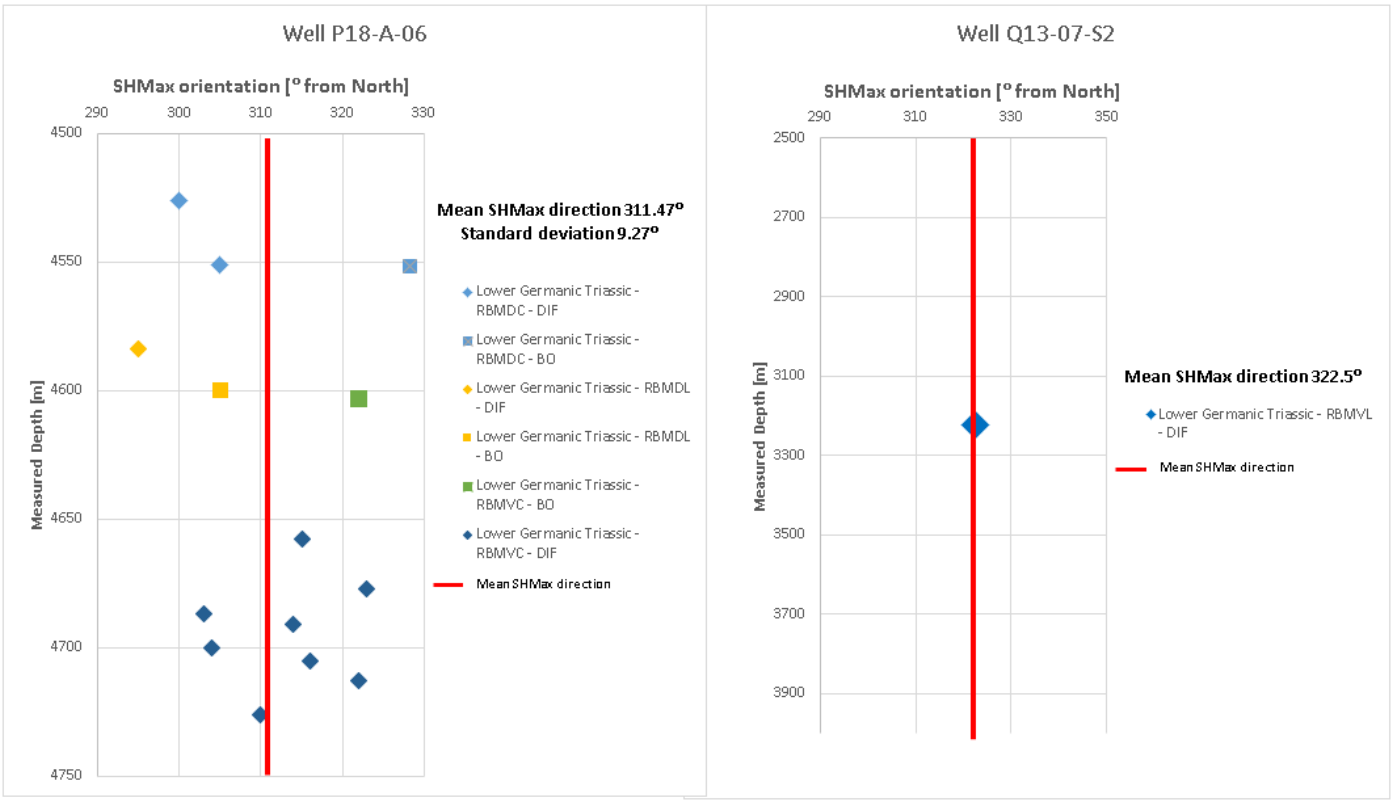

Figure 25. The SHMax orientation with depth (Well P18-A-06 and Q13-07-S2)

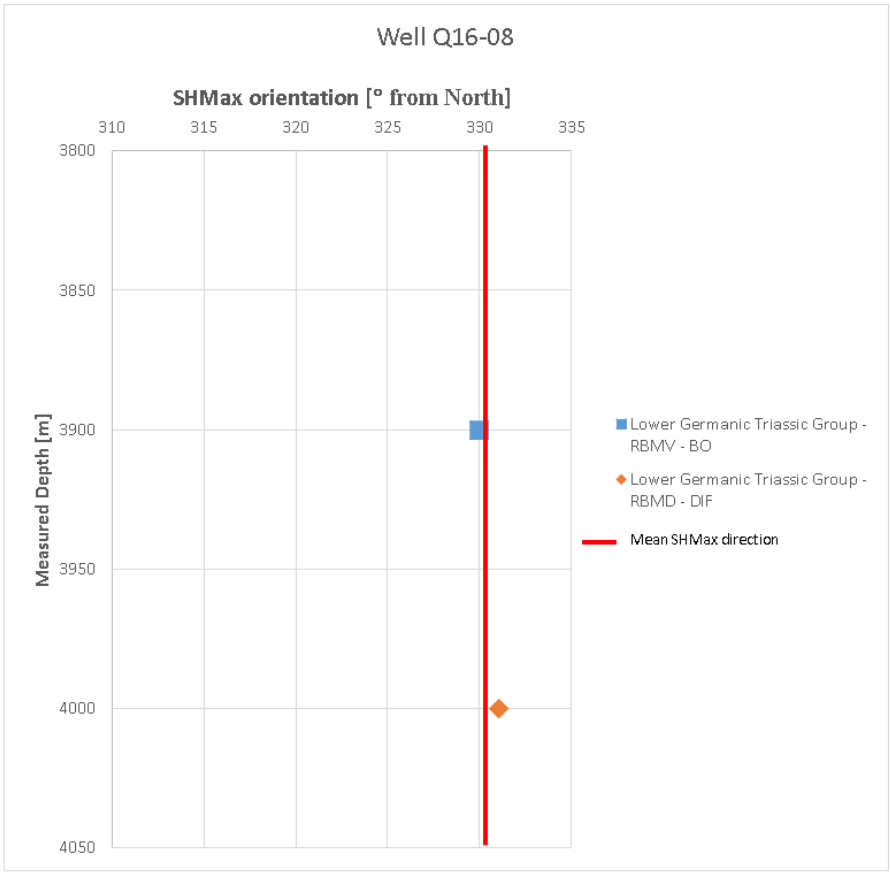

Figure 26. The SHMax orientation with depth (Well Q16-08)

To be concluded, from figures 24, 25, and 26, the stress orientation in and around the study area is ranging from 311°N – 330°N. Also, the result is still in accordance with the study made by Müller et al. (1992), Fuchs and Müller (2001), Klein and Barr (1986) that the SHMax orientation in western Europe shows a uniform NW-SE trend, with a mean value of N145°E or N325°. In addition, the study from Mechelse (2017) stated that most stratigraphies in The Dutch Stress Map indicate an NW-SE of SHMax orientation.

The local stress deviation might occur due to the presence of local geologic structures, such as salt domes. The closer the location to the center of a salt structure, the more the stress field trajectory will be deflected (Mechelse, 2017). However, there is not any presence of salt structures near the study area that could cause stress rotations.

5.3. 1D Geomechanical model

In order to characterize the stress regime at a specific location in the study area, the one-dimensional in-situ stress model will be discussed, that is based on boundary conditions and additional assumptions. As such, the sensitivity of the in-situ stress regime to different parameter conditions can also be studied. There are four models in this study to represent the several possibilities of the stress regimes in well LIR-45 and NLW-GT-01.

The 1D in-situ stress models are made based on stratigraphic and well log data of LIR-45 and NLW-GT-01. Those two wells are located in the study area and intersect with the targeted reservoir in the Main Buntsandstein formation (the Lower Germanic Triassic Group).

In this 1-D model, bulk density from well log data is used in calculating the vertical stress (S_V). The vertical stress, which is controlled by overburden, used varied of bulk density (ρ) from well log data. Pore pressure is assumed to be normal hydrostatic pressure (NHP), and thus fluid density is assumed to equal with 1030 kg/m^3.

5.3.1. Gravity-only model (Model 1)

This model is based on the assumption that gravity is the only source of stress that will affect the magnitude of both vertical and horizontal stress. There is no tectonic stress applied in this model. The Poisson's ratio that is being exerted by the overburden played a significant role in controlling the magnitude of the horizontal stresses (Bertotti et al., 2017). Since this model only uses gravity as a source of the stress, then the model will yield the same magnitude of minimum and maximum horizontal stress (SHMax & Shmin). The calculation for SHMax and Shmin uses equations 7 and 8.

The in-situ stress profiles for the gravity-only model is shown in Figure 27. Furthermore, the magnitude of S_V is always larger than horizontal stresses at all depths, including in the Lower Germanic Triassic group (RB). In other words, the maximum principal stress (σ1) is always vertical stress (S_V). Thus, all stratigraphic units experience only a normal faulting stress regime.

However, there is a small drop in the magnitude of SHMax and Shmin at the interface of the Lower North Sea Group (NL) and the Chalk Group (CK). This condition is caused by a small difference in Poisson's ratio between those two formations (Table 4). However, the overall magnitudes of SHMax and Shmin increase linearly with respect to the depth.

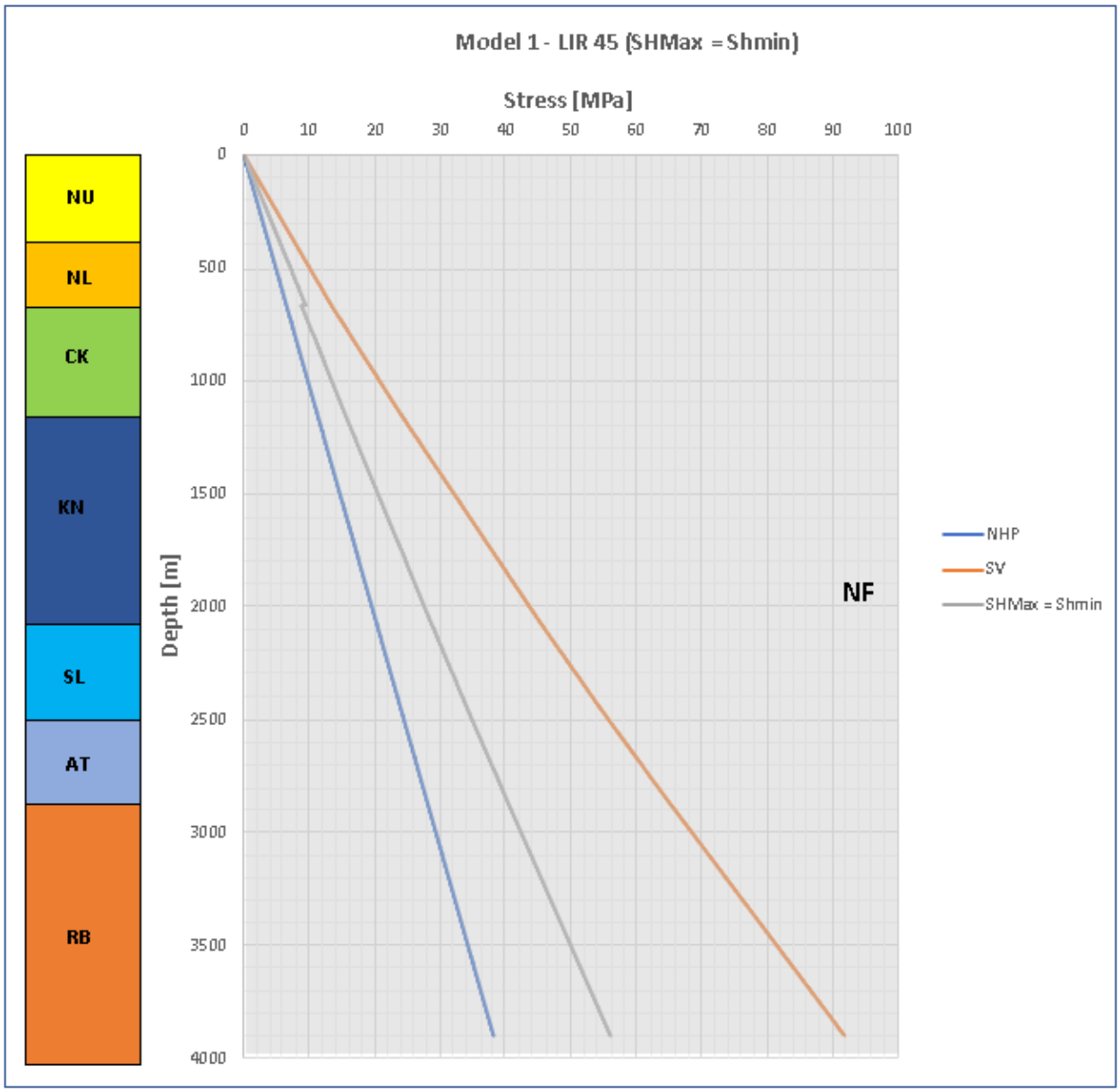

Figure 27. Stress profile against depth; NU=Upper North Sea group;NL=Lower North Sea group; CK=Chalk group;KN=Rijnland group;SL=Schieland group;AT=Altena group;RB=Lower Germanic Triassic group

5.3.2. Gravity-tectonic model (Model 2A)

The second model involves not only gravity but also far-field tectonic stress. The presence of the far-field tectonic stress, in this case, could come from plate movement and lithospheric flexure that are caused by lateral changes in the thickness and density of the lithosphere (Zoback, 2010). Since the presence of far-field tectonic stress affecting the horizontal stress, then the magnitude of minimum and maximum horizontal stress (SHMax and Shmin) will be different. The horizontal stresses (SHMax and Shmin) are determined by using equations 7 and 8.

Table 6. The magnitude of tectonic stress used in the simulation models

Model	Source of stress	Tectonic stress (MPa)
Model 1	Gravity-only	0
Model 2A	Gravity-tectonic	5
Model 2B	Gravity-tectonic	10
Model 2C	Gravity-tectonic	20

The last three models are classified into three different scenarios involving different tectonic stress magnitudes. This is intended to determine to what extent the tectonic forces will affect the stress regime. Table 6 shows a summary of the magnitude of tectonic stress applied to each of the models.

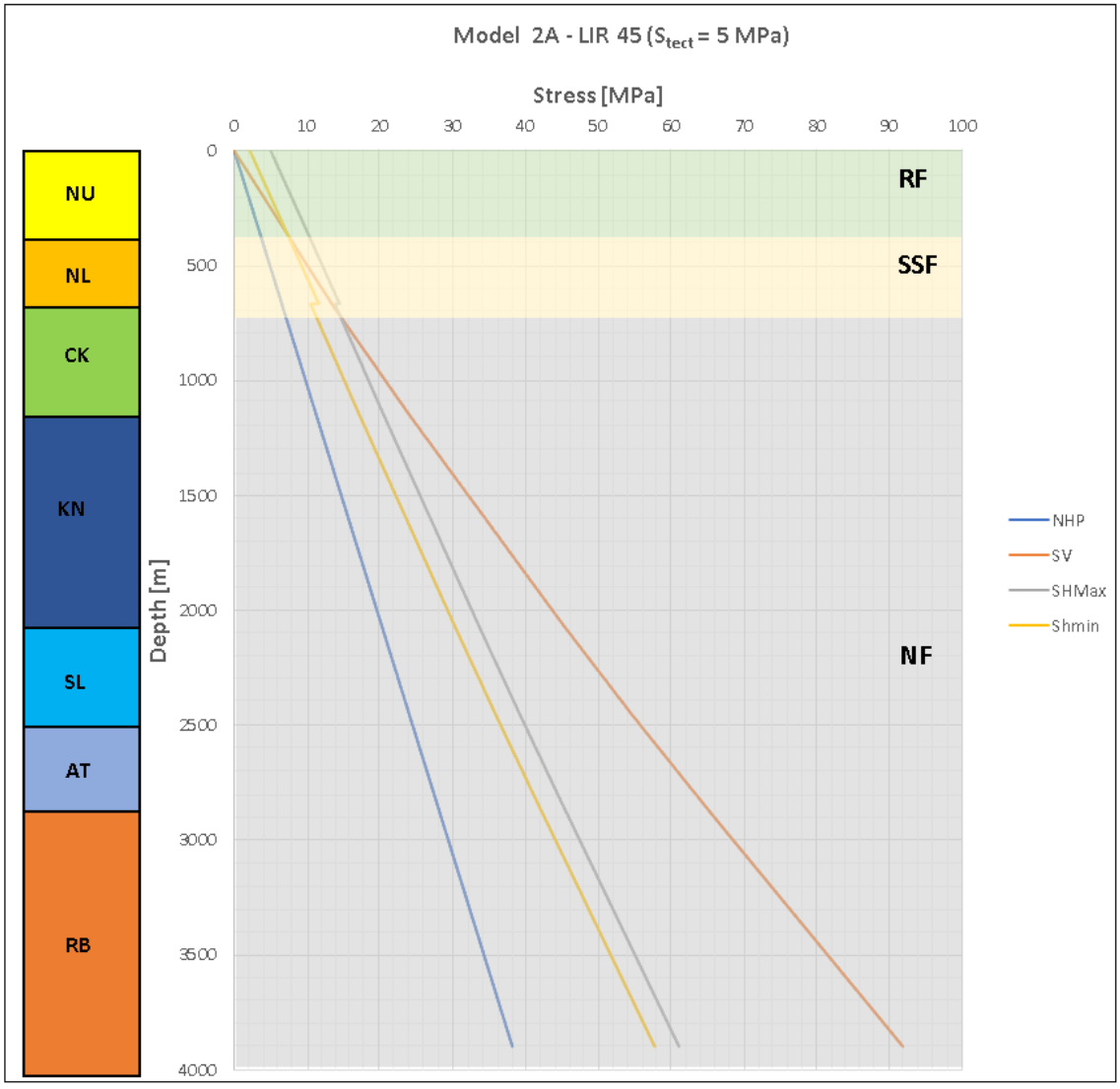

Figure 28. Stress profile against depth with tectonic stress 5 MPa; NF = Normal Fault SSF = Strike-slip fault; RF = Reverse fault

Model 2A used additional 5 MPa tectonic stress. Figure 28 depicts the effect of tectonic stress on the tectonic regime. Unlike model 1, in model 2A, the vertical stress (S_V) does not always become the maximum principal stress. Through depth, the stress direction cross to each other; thus, stress permutation occurs at a depth of transition.

At the first 400 m depth, the vertical stress acts as the minimum principal stress. Furthermore, the SHMax and Shmin act as the maximum and intermediate principal stress, respectively. Thus, the uppermost depth experiences reverse faulting stress regime (RF).

The strike-slip faulting stress regime (SSF) occurs at depth -400 m to -720 m. At this range of depth, the vertical stress acts as the intermediate principal stress. Meanwhile, the depth of transition between the strike-slip faulting stress regime to normal faulting stress regime is situated at a depth of -720 m. Therefore, the Lower Germanic Triassic group (situated at a depth from -3000 m to -4000 m) is entirely in a normal fault tectonic regime (NF). The magnitudes of the vertical stress (Sv) increase linearly, and at some point, it exceeds the horizontal stresses, hence Sv becomes the maximum principal stress.

5.3.3. Gravity-tectonic model (Model 2B)

The third model also includes tectonic stress in the calculation. The tectonic stress magnitude is 10 MPa. Figure 29 illustrates how the stress regime changes trough the depth and thus, resulting in three different tectonic regimes.

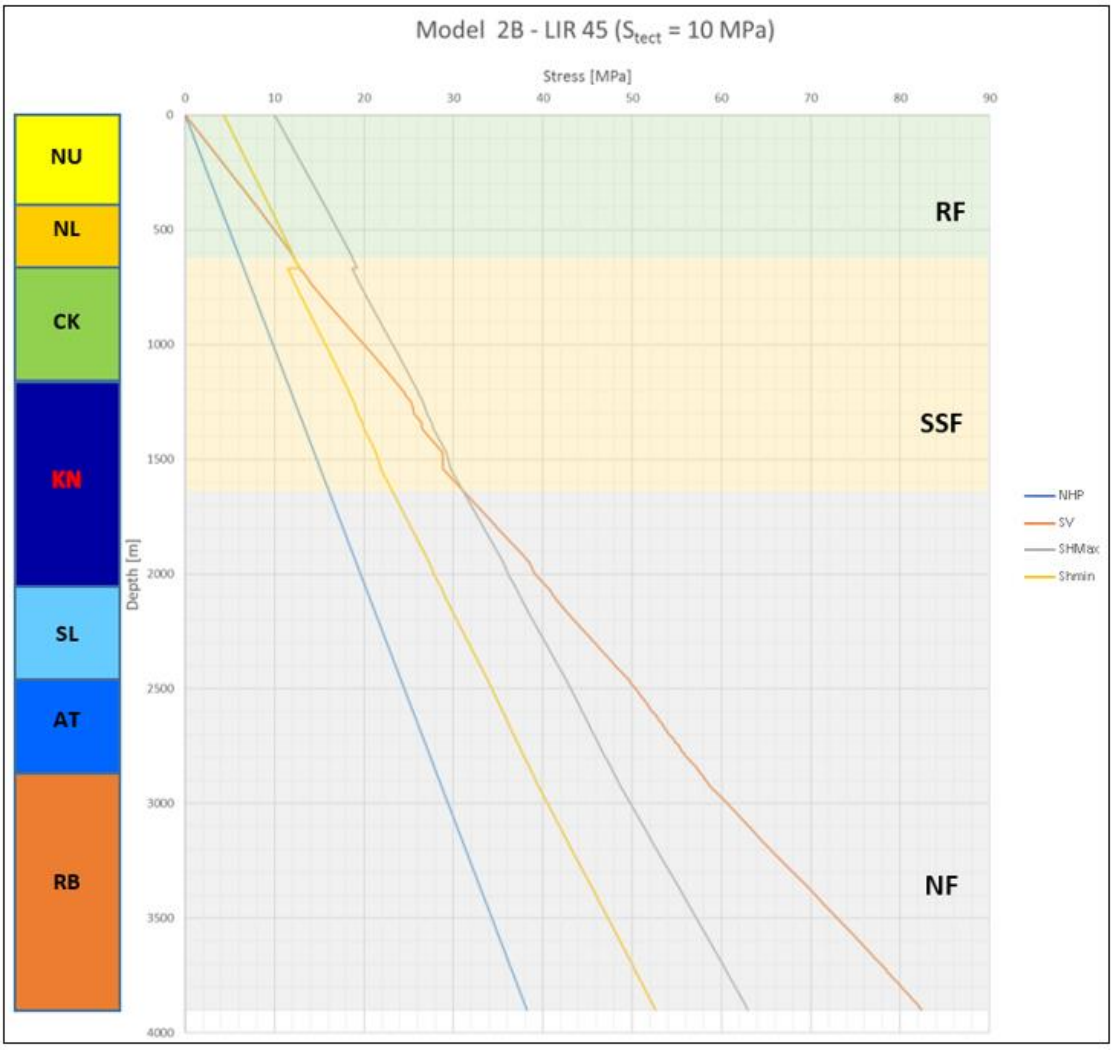

Figure 29. Stress profile against depth with tectonic stress 10 MPa; NF = Normal Fault SSF = Strike-slip fault ; RF = Reverse fault

The depth between 0 m to -600 m experiences reverse faulting stress regime (RF), whereas strike-slip faulting regime is observed at the depth from -600 m to -1650 m. The normal faulting regime is found deeper than in what happened in Model 2A. The regime of normal faulting is started at a depth of -1650 m compared to Model 2A at a depth of 800 m.

5.3.4. Gravity-tectonic model (Model 2C)

The last scenario also includes additional tectonic stress of 20 MPa. According to Figure 30, three tectonic regimes are spotted along with the depth. It appears that by applying greater tectonic stress in the model, makes all tectonic boundaries shift downwards. In addition, the zone for each tectonic regime model also becomes larger than the previous model with relatively small tectonic stress.

Figure 30 also shows that the reverse fault regime appears at first 1000 m of depth, followed by a strike-slip fault regime until a depth around -2900 m. The rest of the depth is in a state of a normal faulting regime.

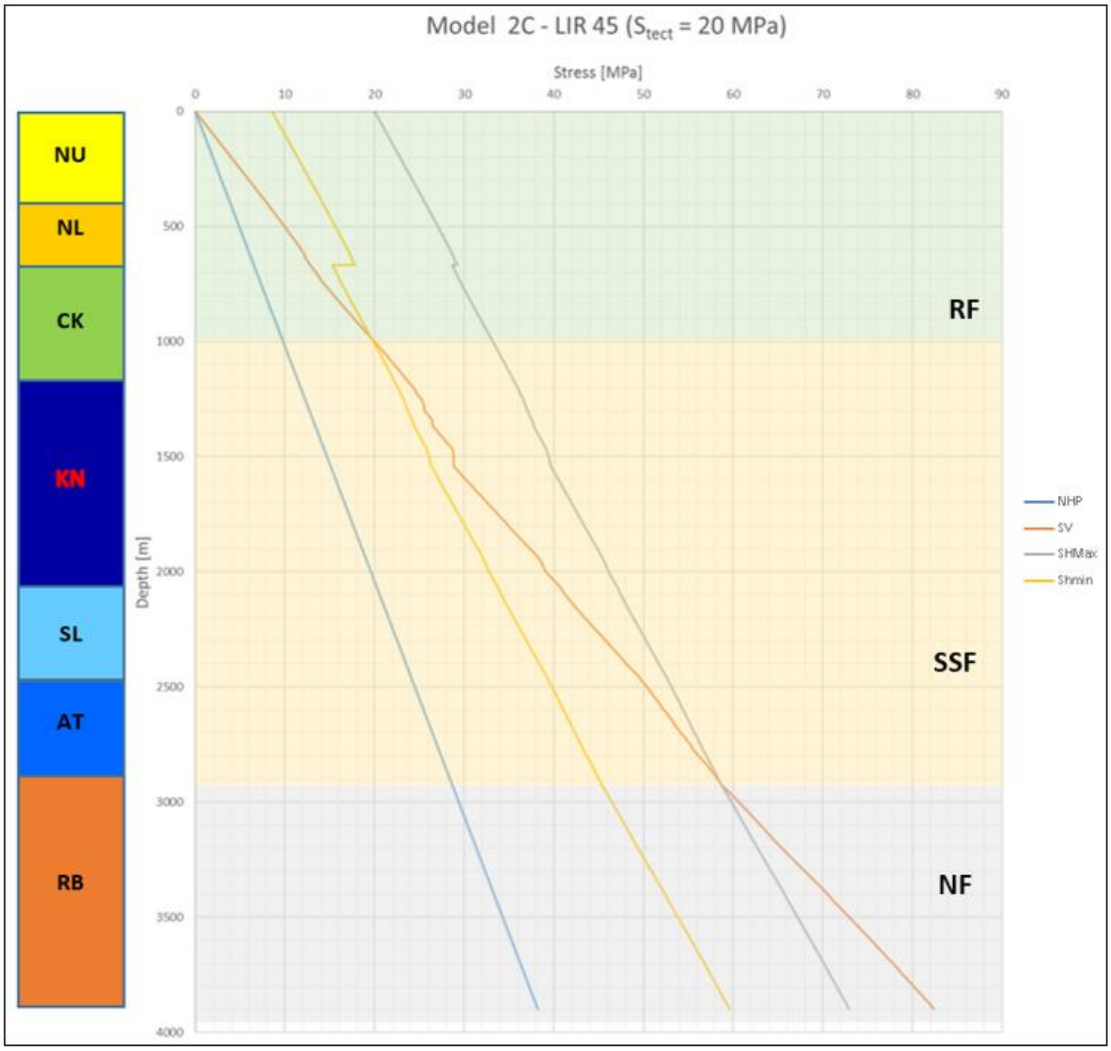

Figure 30. Stress profile against depth with tectonic stress 20 MPa; NF = Normal Fault SSF = Strike-slip fault; RF = Reverse fault

5.3.5. Comparison of the models

Table 7 shows the summary of stress faulting regimes and their corresponding principal stress for each model. It can be concluded that in the model where tectonic stress is absent (Model 1), the only stress regime that can be observed is only a normal fault stress regime. Whereas in all models where tectonic stress is added (Model 2A, 2B, and 2C), three different stress regimes are observed.

There are normal fault, strike-slip, and reverse faulting regime observed in all gravity-tectonic models (Model 2A, 2B, and 2C). Furthermore, those three different stress regimes occur at different depths according to the magnitude of the tectonic stress added in the model. The bigger the tectonic stress, the larger the zone for each of the stress regimes. For example, in model 2A, where only 5 MPa tectonic stress was added, resulting in 400 m of reverse faulting regime zone. Whereas in model 2C where 20 MPa tectonic stress was added, resulting in almost 1,000 m of reverse faulting regime zone.

In addition, by adding a more significant magnitude of tectonic stress, the tectonic boundaries shift downward. The stress permutations are observed in all gravity-tectonic models (Model 2A, 2B, and 2C), at which the principal stresses direction changes throughout the depth. However, the stress regime transition is controlled by the depth rather than by stratigraphic units.

Table 7. Summary of stress faulting regime from all models

Model	Stress regime	Depth (m)	σ1	σ2	σ3
Model 1	Normal faulting	0-3900	S_V	SHMax	Shmin
Model 2A	Reverse faulting	0-400	SHMax	Shmin	S_V
	Strike-slip faulting	400-720	SHMax	S_V	Shmin
	Normal faulting	720-3900	S_V	SHMax	Shmin
Model 2B	Reverse faulting	0-600	SHMax	Shmin	S_V
	Strike-slip faulting	600-1650	SHMax	S_V	Shmin
	Normal faulting	1650-3900	S_V	SHMax	Shmin
Model 2C	Reverse faulting	0-1000	SHMax	Shmin	S_V
	Strike-slip faulting	1000-2900	SHMax	S_V	Shmin
	Normal faulting	2900-3900	S_V	SHMax	Shmin

5.4. 3D Geomechanical model

5.4.1. 3D Mesh model

The first process prior to creating a 3D mesh is creating a 3D structural model. The 3D structural model is the integration process between the fault model, the stratigraphic model, horizons surface set, and markers. The output of this process was used as an input for 3D mesh structural modeling. Figure 32 shows the example of a 3D structural model used in the modeling.

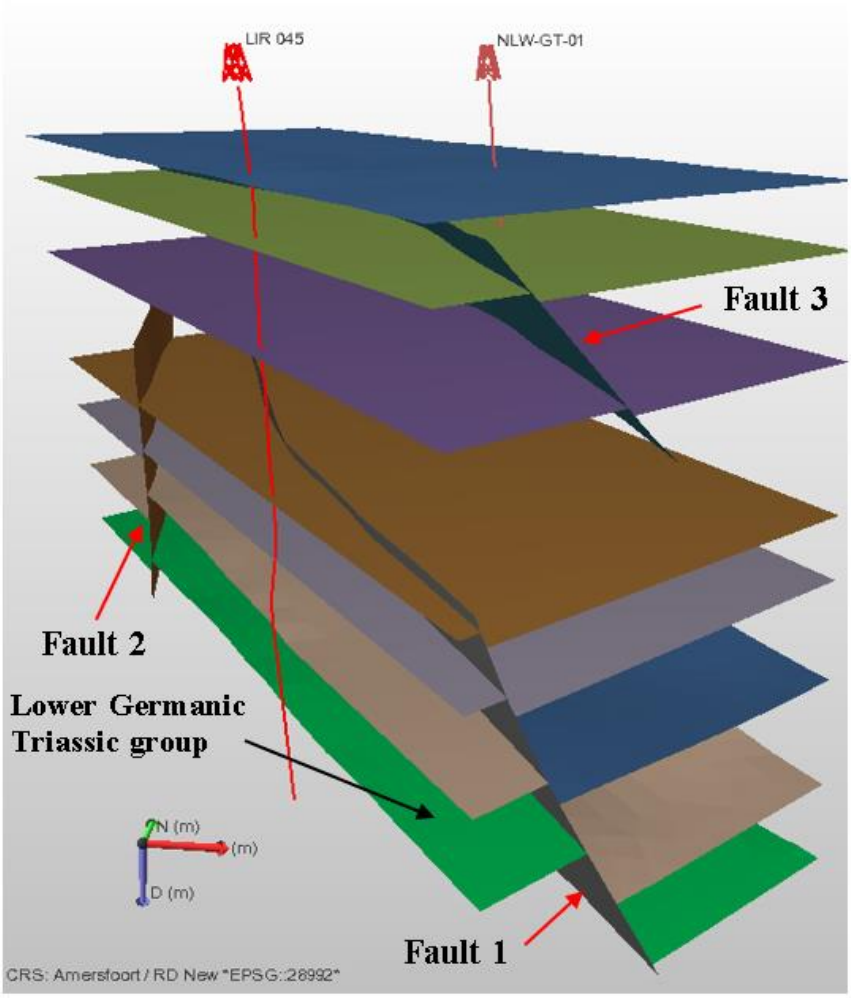

Figure 31. The 3D Structural model of horizons and faults

Furthermore, the product of a 3D mesh structural model is similar to a 3D structural model in appearance, but the 3D mesh structural model has coarser tri-mesh shape surfaces (Figure 33). The re-meshing parameters result can be seen in Table 3. After the 3D mesh structural modeling was completed, those surfaces are ready to export to the Abaqus/CAE software to create a 3D finite element mesh model.

The result of the 3D mesh model is presented in Figure 34. Some compartments between horizons and faults were identified. This means that the previous process was conducted entirely watertight at intersections and/or the edges of the model; otherwise, the compartment will be overlapping.

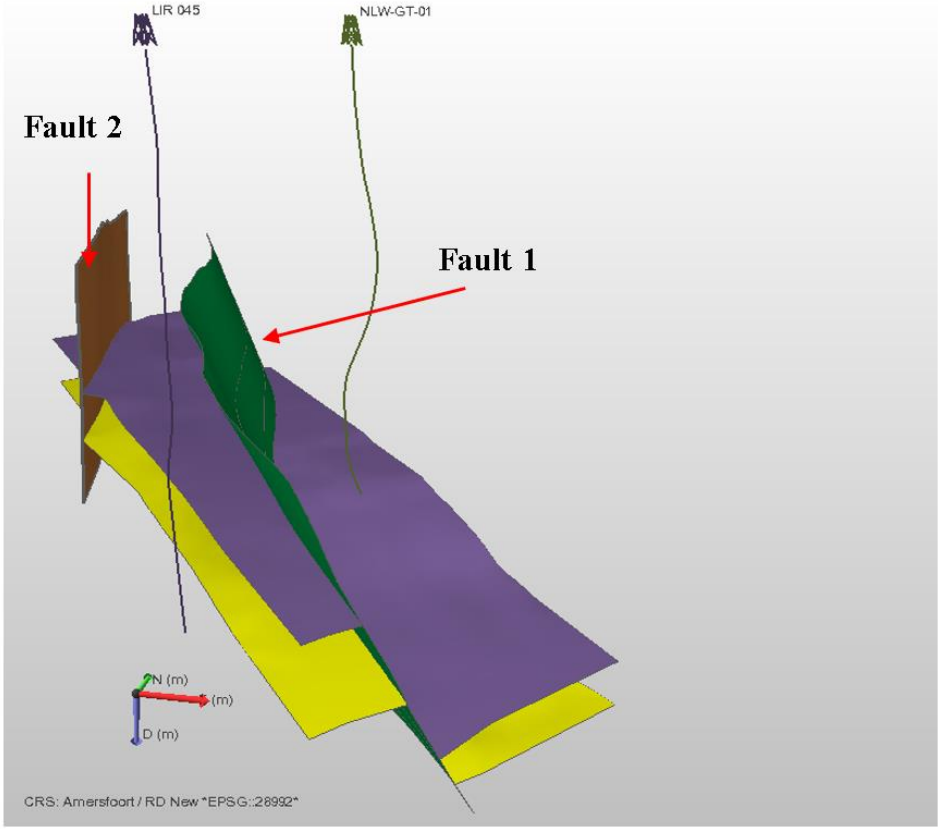

Figure 32. The 3D structural model of the Lower Germanic Triassic group and fault 1 & 2

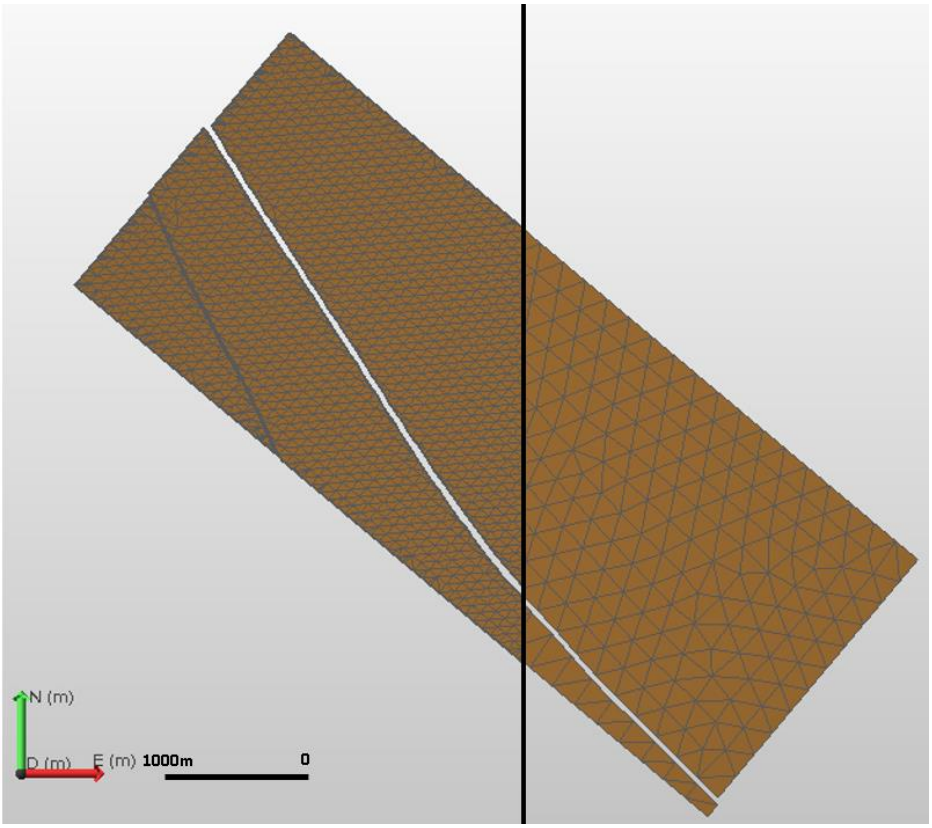

Figure 33. The comparison between 3D structural model (left) and 3D mesh structural model (right), the base of the Rijnland group (KN)

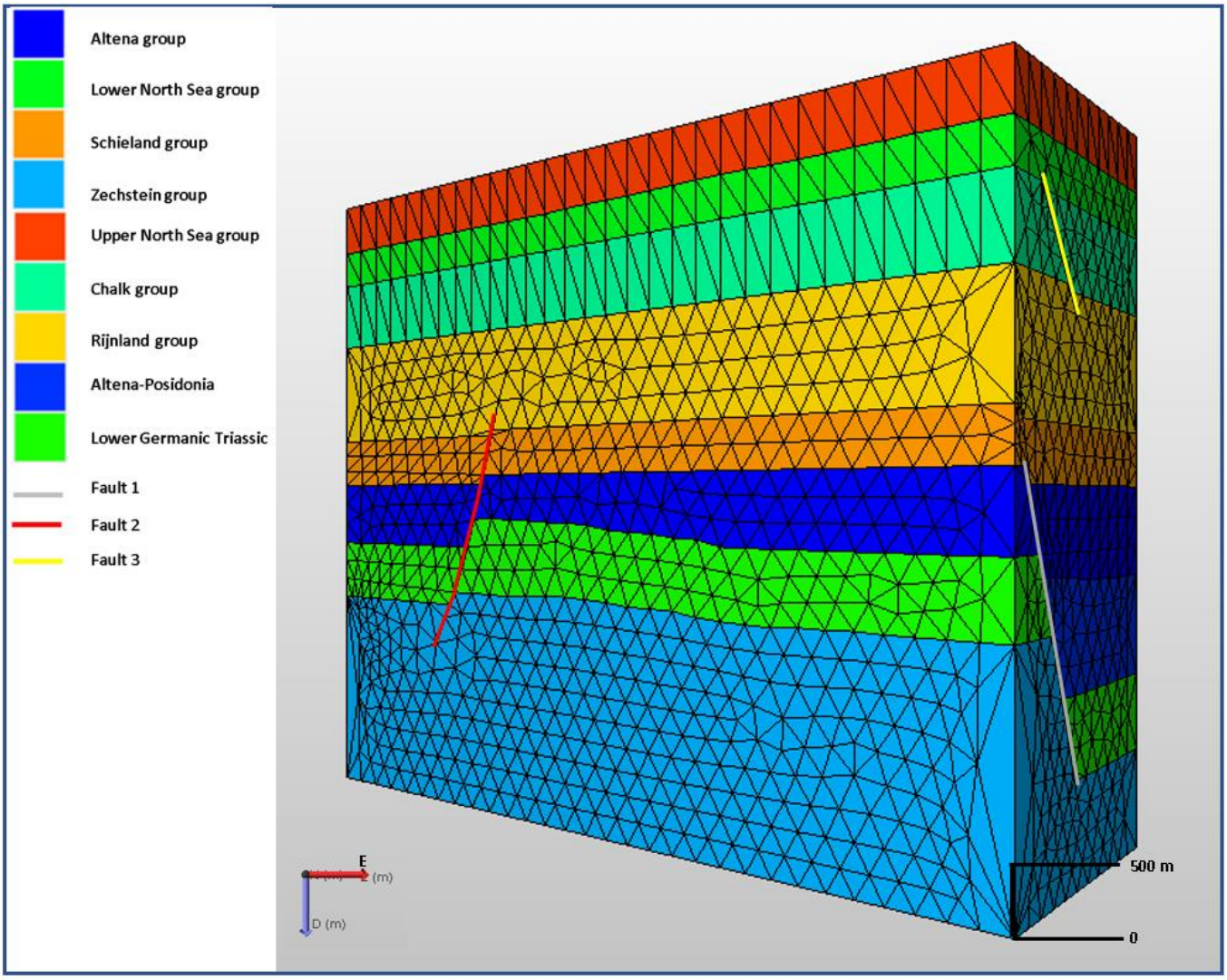

Figure 34. The finite element model and its corresponding materials, view from South

5.4.2. Stress simulation

Abaqus simulation is conducted in two steps. First, the stress initialization stage in which the 3D finite element mesh model is populated with applied ESRmin and ESRmax. Abaqus then runs a step to obtain equilibrium on the model. The output stress field, which will be oriented based on the azimuth of SHMax as input, is then processed by a Python script to apply the actual stress field orientation and effective stress ratios.

The next stage is a full geomechanical simulation that includes a stress calculation. The initial stress tensor is used as the initial stress state for the full Abaqus simulation. The results in the .odb file are processed in Abaqus. The results are then imported on the mesh in JewelSuite, where they can be used for further analysis and processing. Figure 35 shows the result of the geomechanical simulation. The model has the vertical stress in d-direction, pointing vertically by the orange arrow, and maximum horizontal stress with azimuth 325° (NW).

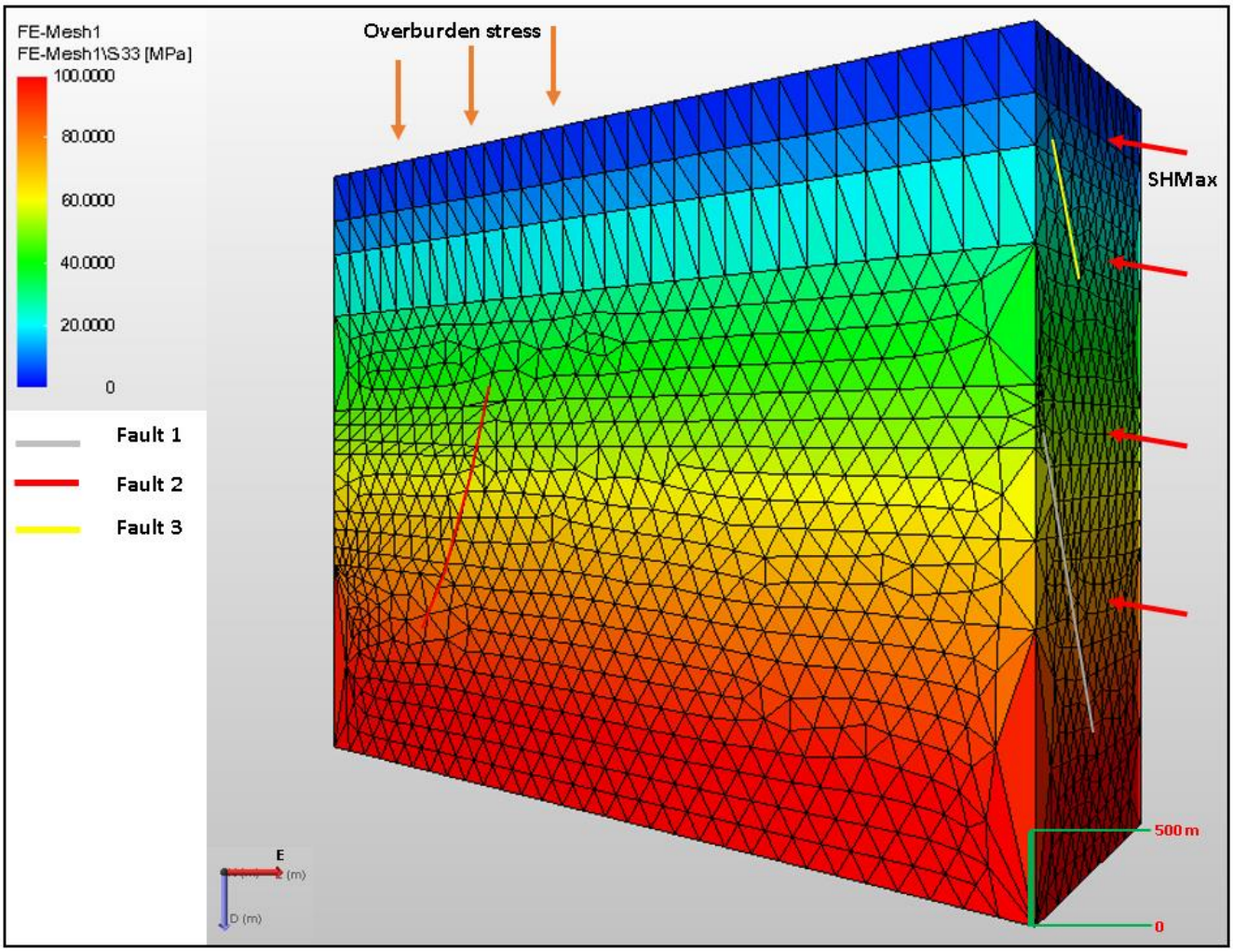

Figure 35. The finite element model and S33 (vertical stress), view from South

5.4.3. Point analysis

Point analysis was conducted to obtain information about the principal stress magnitude and its orientation at a particular point in the 3D finite element model. There are two points samples taken from cross-section 1. The point's location can be seen in Figure 36. Point A and B are situated at the up-thrown block and down-thrown block of the Lower Germanic Triassic group, respectively. The detailed description of the model is listed in Table 8.

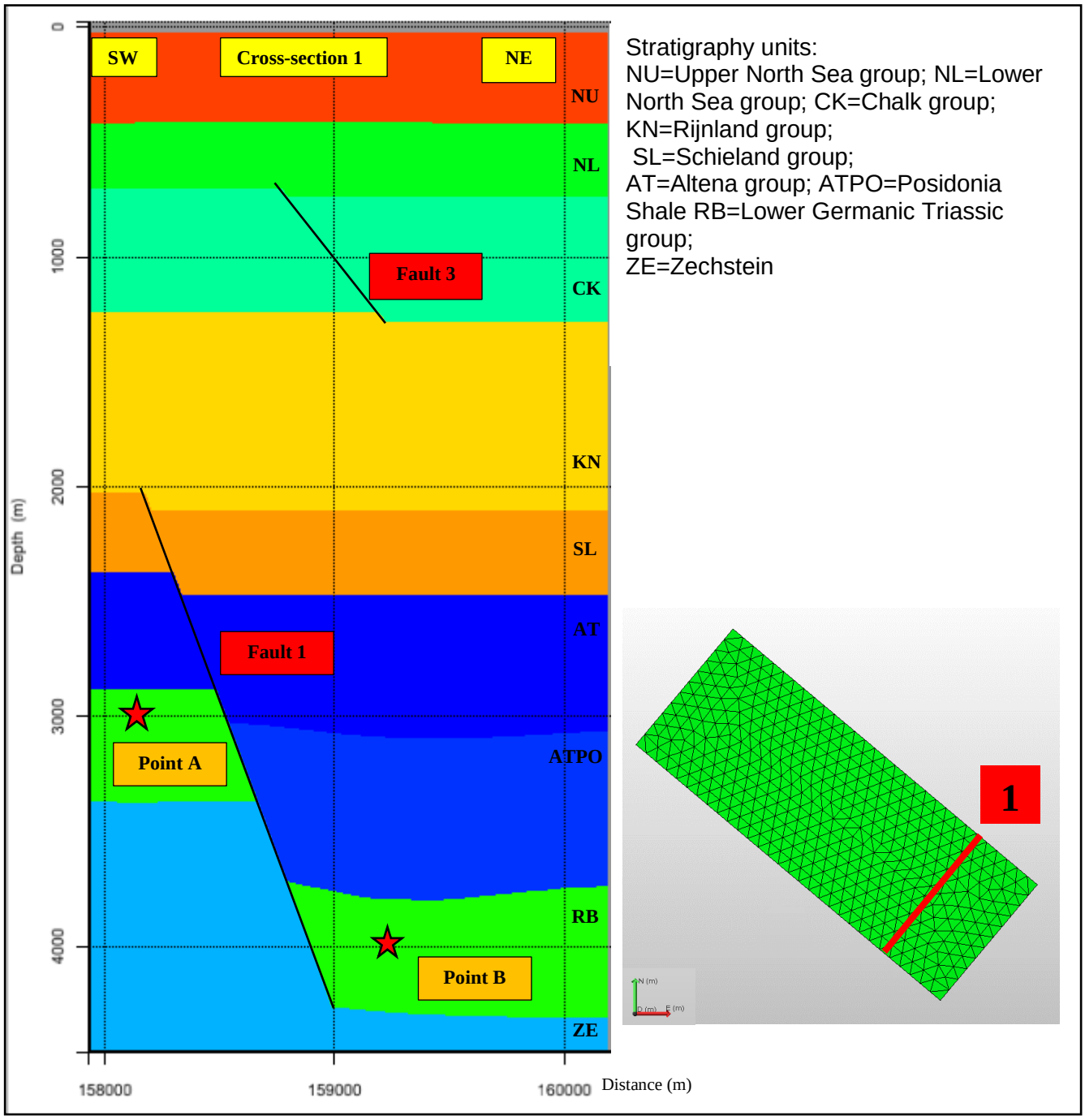

Figure 36. Cross-section 1 and the location of point A and B

Table 8. Point information – cross-section 1

Cross-section 1	Easting	Northing	Element ID	Node ID	Depth (m)	Material
Point A	75657	444262	63960	91620	-3000	RB
Point B	76594	445380	59387	86375	-4000	RB

Point A (-3000 m)

The magnitude of the principal stresses of point A in all models can be seen in Figure 37. The negative signs of the Abaqus/CAE convention were switched into a positive sign geomechanical convention, and they represent compressive stress. Point (Figure 37) experiences a normal fault stress regime in model 1, 2A, and 2B. The maximum principal stress is oriented to the vertical direction and coincides with the vertical stress (Sv). However, stress permutation occurred in model 2C when the magnitude of the vertical stress is almost equal to the maximum horizontal stress (Sv = SHMax). Thus, the direction of intermediate principal stresses is a combination of horizontal stress and vertical stress (Figure 38)

Therefore, it makes the zone at a depth around -3000 m could have a strike-slip fault regime and a normal fault regime at the same time. From this depth onward, in model 2C, the formation experiences a normal fault regime, whereas, at a shallower depth, the formation experiences a strike-slip fault regime, as indicated in Figure 30 (1D Geomechanical model 2C).

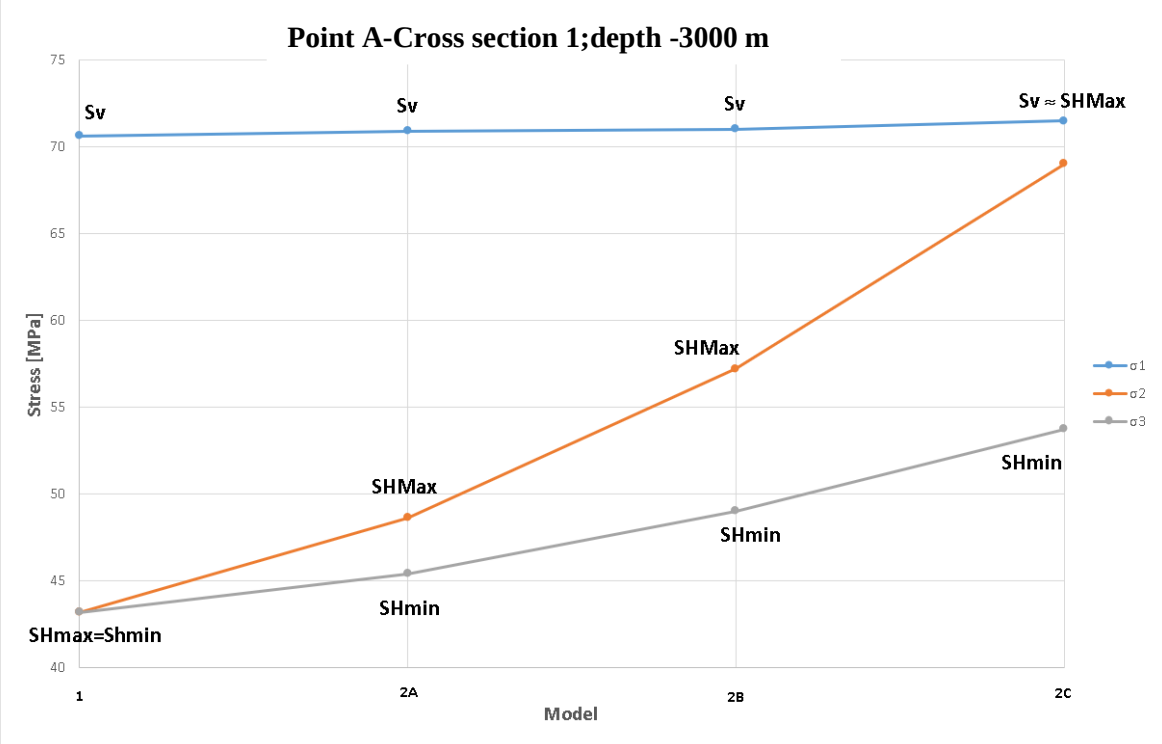

Figure 37. The magnitude of principal stresses at point A-cross section 1

Model 1 is the gravity only model, where tectonic stress absent. Model 2A, 2B, and 2C are gravity-tectonic stress with additional tectonic stress 5 MPa, 10 MPa, and 20 MPa, respectively.

Figure 38 illustrates the intermediate principal stress direction with arrows symbol in model 2C. The negative signs of these principal stresses represent the compressive stress. Stress permutation is observed around a depth around -3000 m, also marked the depth of transition. They are indicating that the intermediate principal stress direction changes from the vertical direction to the horizontal direction. The intermediate stress orientation, at a depth shallower than -3000 m, oriented to a vertical direction and coincided with the vertical stress (Sv). In other words, depth less than -3000 m is in the strike-slip faulting regime. However, at a depth deeper than -3000 m, the intermediate principal stress orientation changes from the vertical direction to horizontal direction. The change in stress faulting regime is because the vertical stress (Sv) increases at a higher rate compared to the horizontal stresses. Therefore, at a certain depth, the vertical stress (Sv) will become the maximum principal stress.

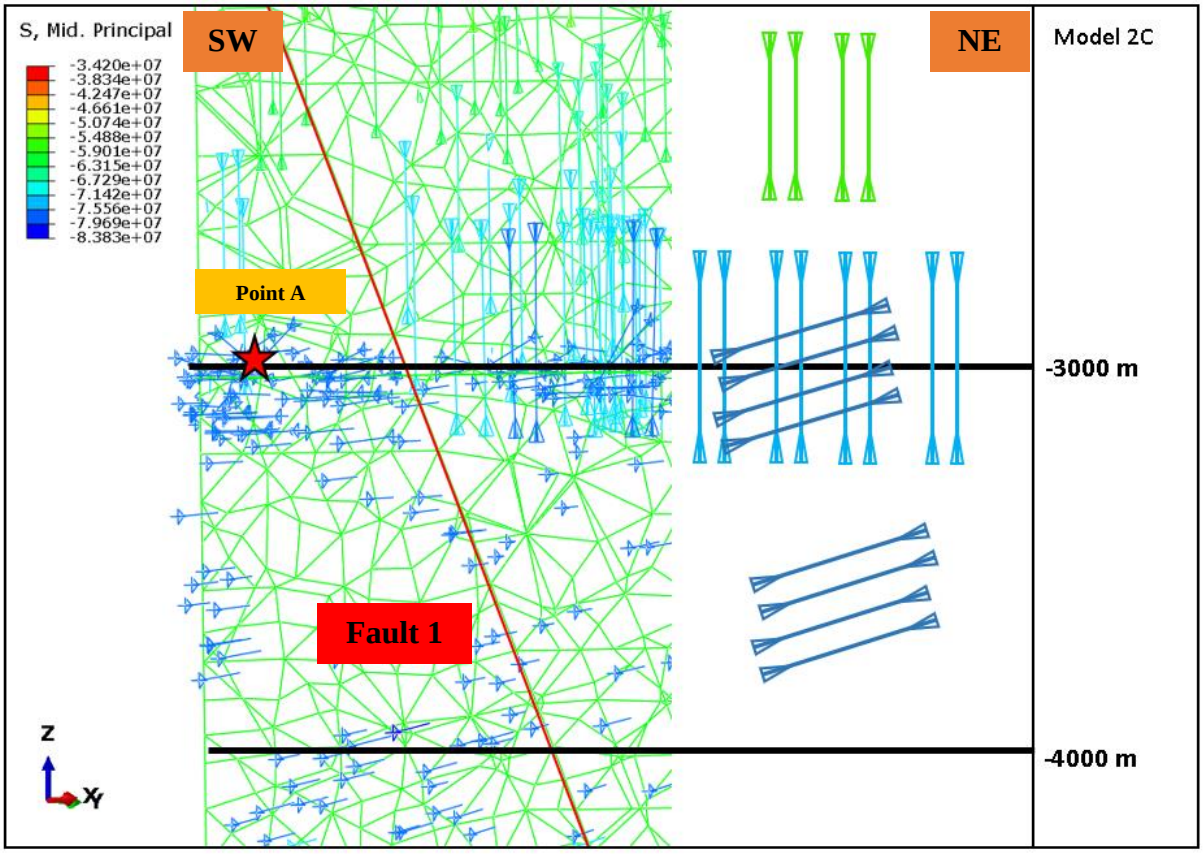

Figure 38. The intermediate principal stress orientation; cross-section 1

Point B (-4000 m)

Figure 39 shows the trend of the principal stresses at a depth of -4000 m. The magnitude of $\sigma 1$ in point B is similar throughout all the models. The maximum principal stress is oriented to a vertical direction and coincides with the vertical stress (Figure 40). Thus, point B is always in the state of a normal faulting regime. However, the transition depth in model 2C takes place at the shallower depth.

The summary of the principal stresses orientation, and its stress regime is presented in Table 9.

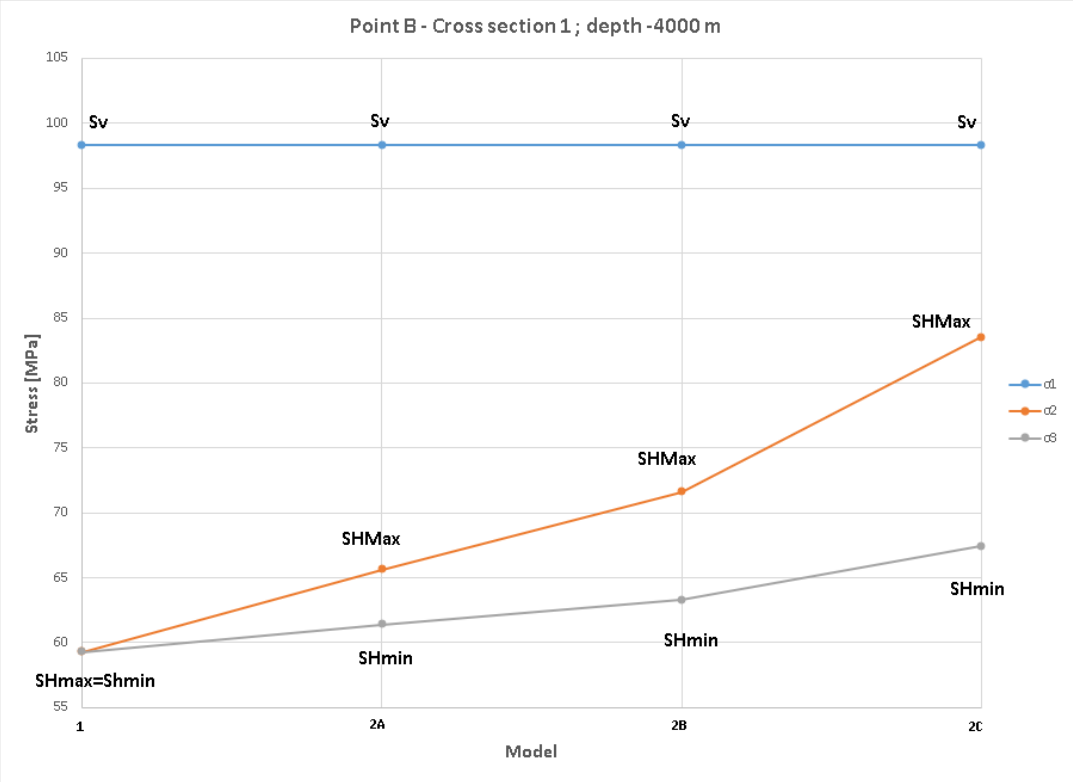

Figure 39. The magnitude of principal stresses at point B-cross section 1

Model 1 is the gravity only model, where tectonic stress absent. Model 2A, 2B, and 2C are gravity-tectonic stress with additional tectonic stress 5 MPa, 10 MPa, and 20 MPa, respectively.

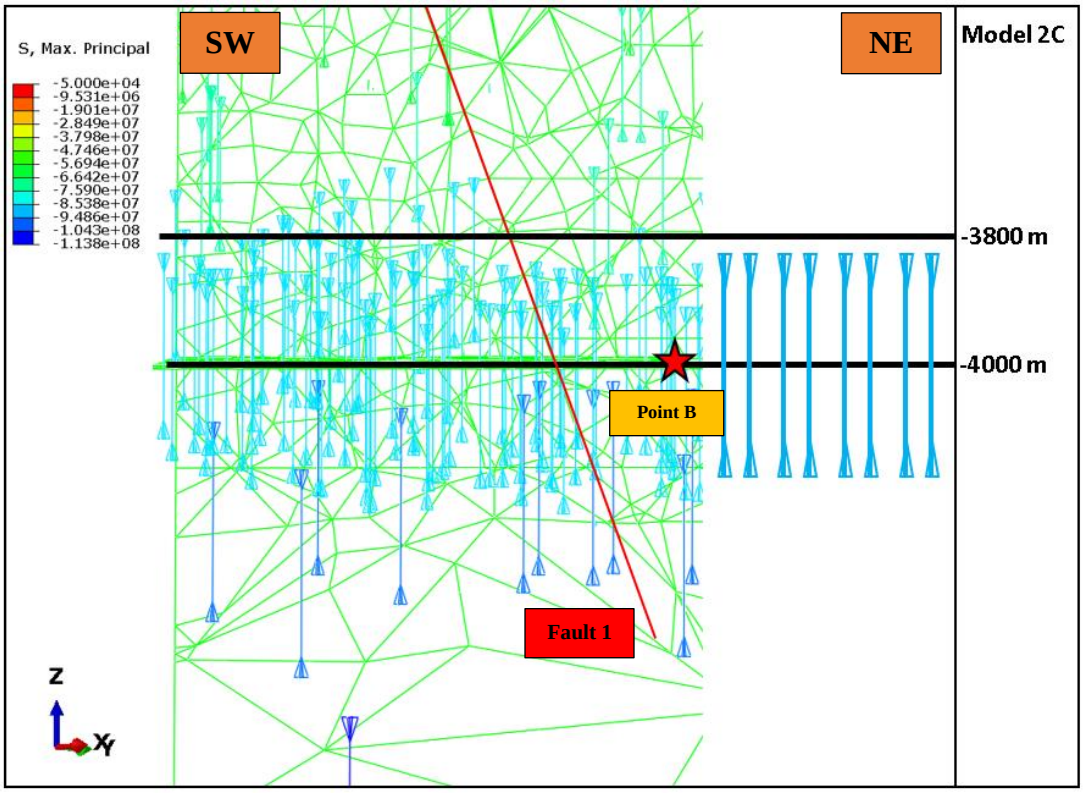

Figure 40. The maximum principal stress orientation; cross-section 1

Table 9. Summary of stress faulting regime of all points in all 3D models

Model	Point	Depth (m)	Tectonic stress (MPa)	σ1	σ2	σ3	Stress regime
Model 1	A	-3000	0	S_V	SHMax	Shmin	Normal faulting
Model 2A			5	S_V	SHMax	Shmin	Normal faulting
Model 2B			10	S_V	SHMax	Shmin	Normal faulting
Model 2C			20	S_V & SHMax	S_V & SHMax	Shmin	Strike-slip faulting & Normal faulting
Model 1	B	-4000	0	S_V	SHMax	Shmin	Normal faulting
Model 2A			5	S_V	SHMax	Shmin	Normal faulting
Model 2B			10	S_V	SHMax	Shmin	Normal faulting
Model 2C			20	S_V	SHMax	Shmin	Normal faulting

5.4.4. Cross-section analysis

The cross-section analysis was performed in order to understand stress distribution in a lateral direction. The example location of the cross-section can be seen in Figure 41. The cross-section is situated at a depth of -3000 m. The negative signs of the Abaqus/CAE convention were switched into a positive sign geomechanical convention, and they represent compressive stress.

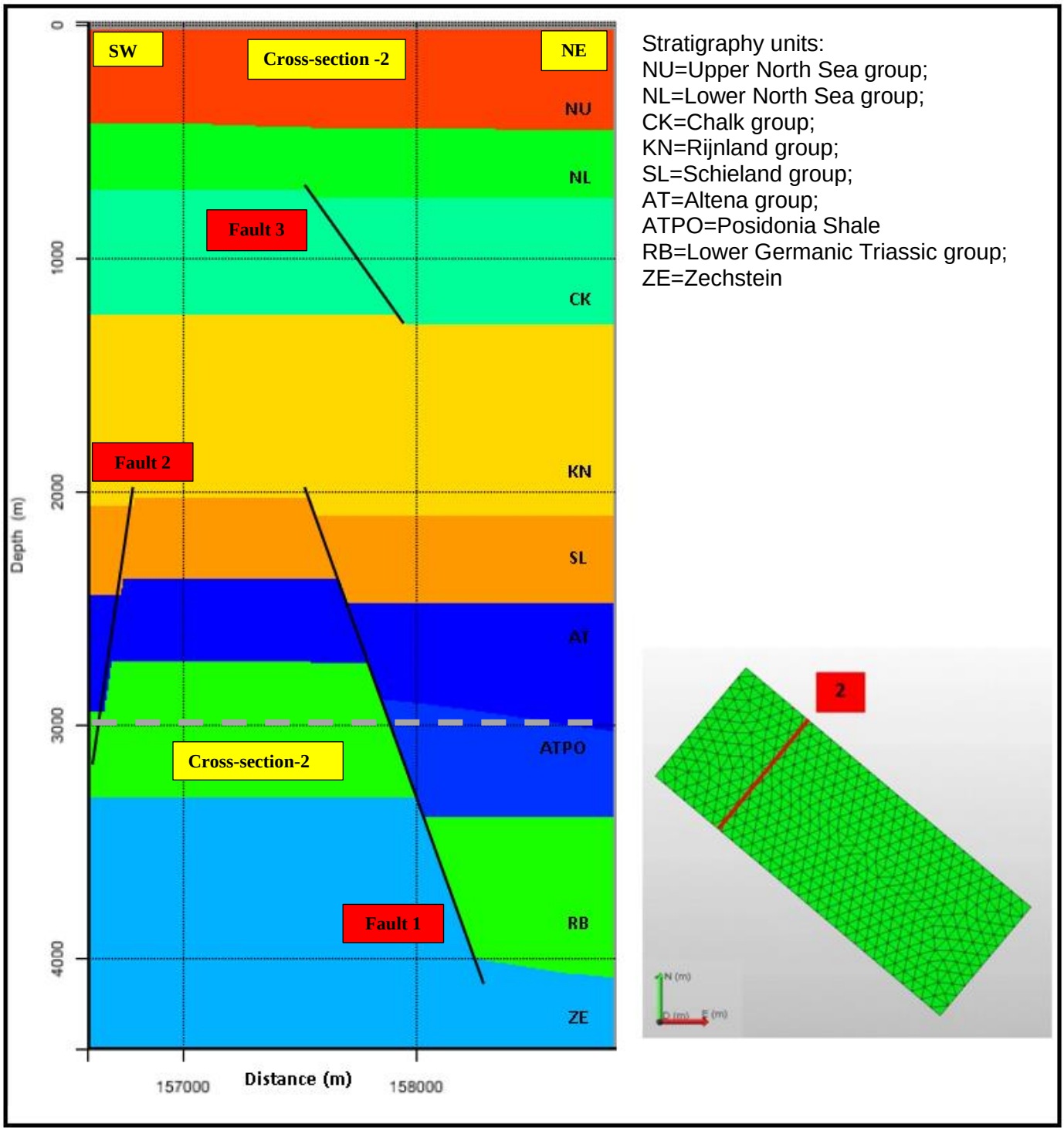

Figure 41. Cross-section 2 and the location of cross-section analysis

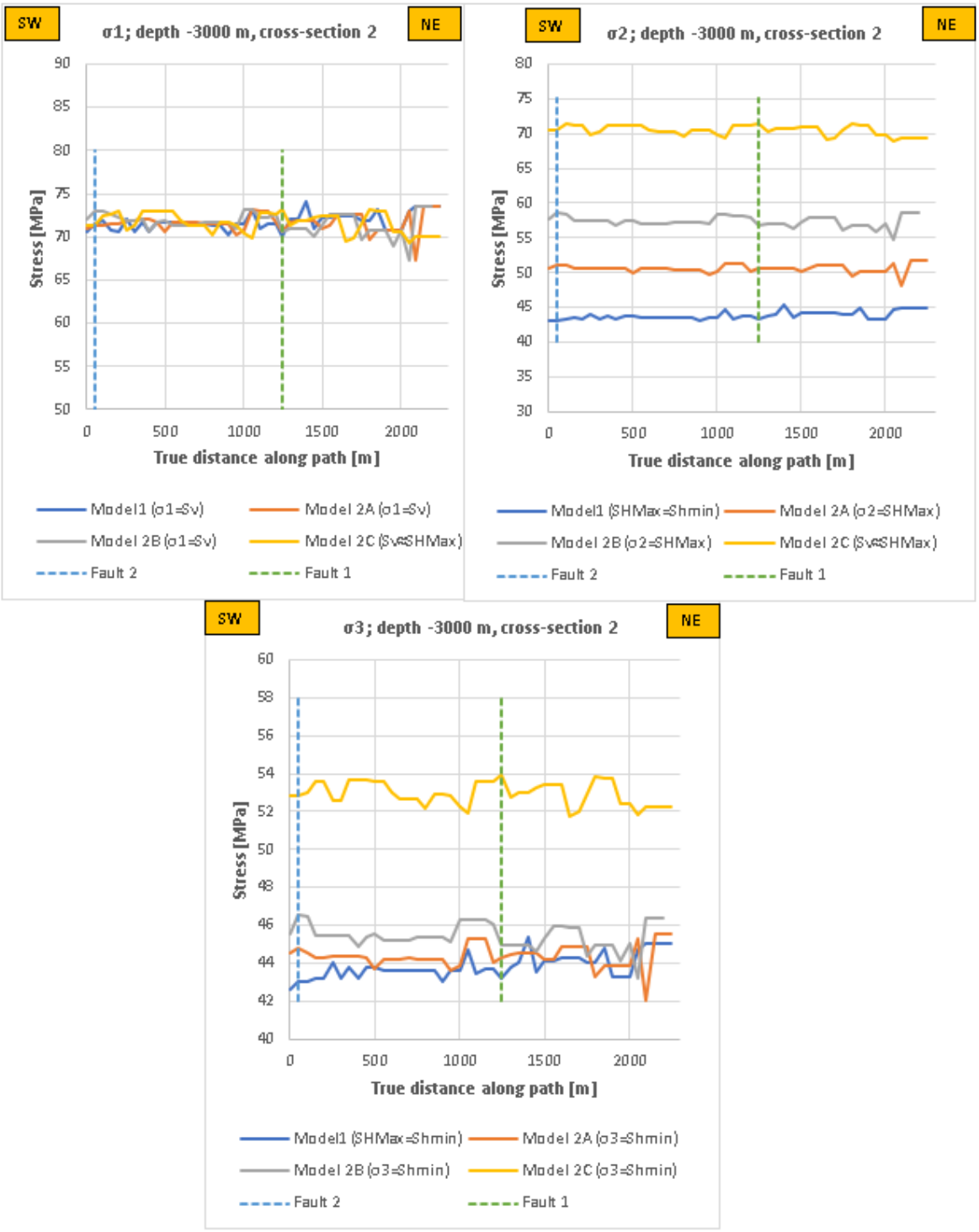

Figure 42. The magnitude of principal stresses in cross-section 2 (depth of -3000 m). Left: Maximum principal stress, right: intermediate principal stress, bottom: minimum principal stress

Model 1 is the gravity only model, where tectonic stress absent. Model 2A, 2B, and 2C are gravity-tectonic stress with additional tectonic stress 5 MPa, 10 MPa, and 20 MPa, respectively. Note, faults indicated in Figure 42 does not represent the actual size. It only represents the position of faults within a cross-section.

Figure 42 shows that the magnitudes of all principal stresses show some variations along the cross-section. The principal stresses magnitudes vary locally due to the presence of geological

unconformities, different stratigraphy units, geological structures (faults and fractures), and rock properties. However, the magnitudes of σ1 are similar in all models, because the maximum principal stress is coinciding with the vertical stress (Sv). Thus, the vertical stress is only influenced by density and depth. It also can be implied that there are stress permutations between σ1 and σ2 in model 2C, as the magnitudes of both principal stresses are almost similar. It means that the depth around -3000 m is a depth of transition, where stress faulting regime change. The change in stress faulting regime is because the vertical stress (Sv) increases at a higher rate compared to the horizontal stresses.

Figure 43 shows that at the upper levels, above the depth of transition, the intermediate principal stress (σ2) coincides with the vertical direction. Meanwhile, at deeper levels, below the depth of transition, the intermediate principal stress (σ2) coincides with the horizontal direction. Thereby, the vertical stress becomes the maximum principal stress (σ1).

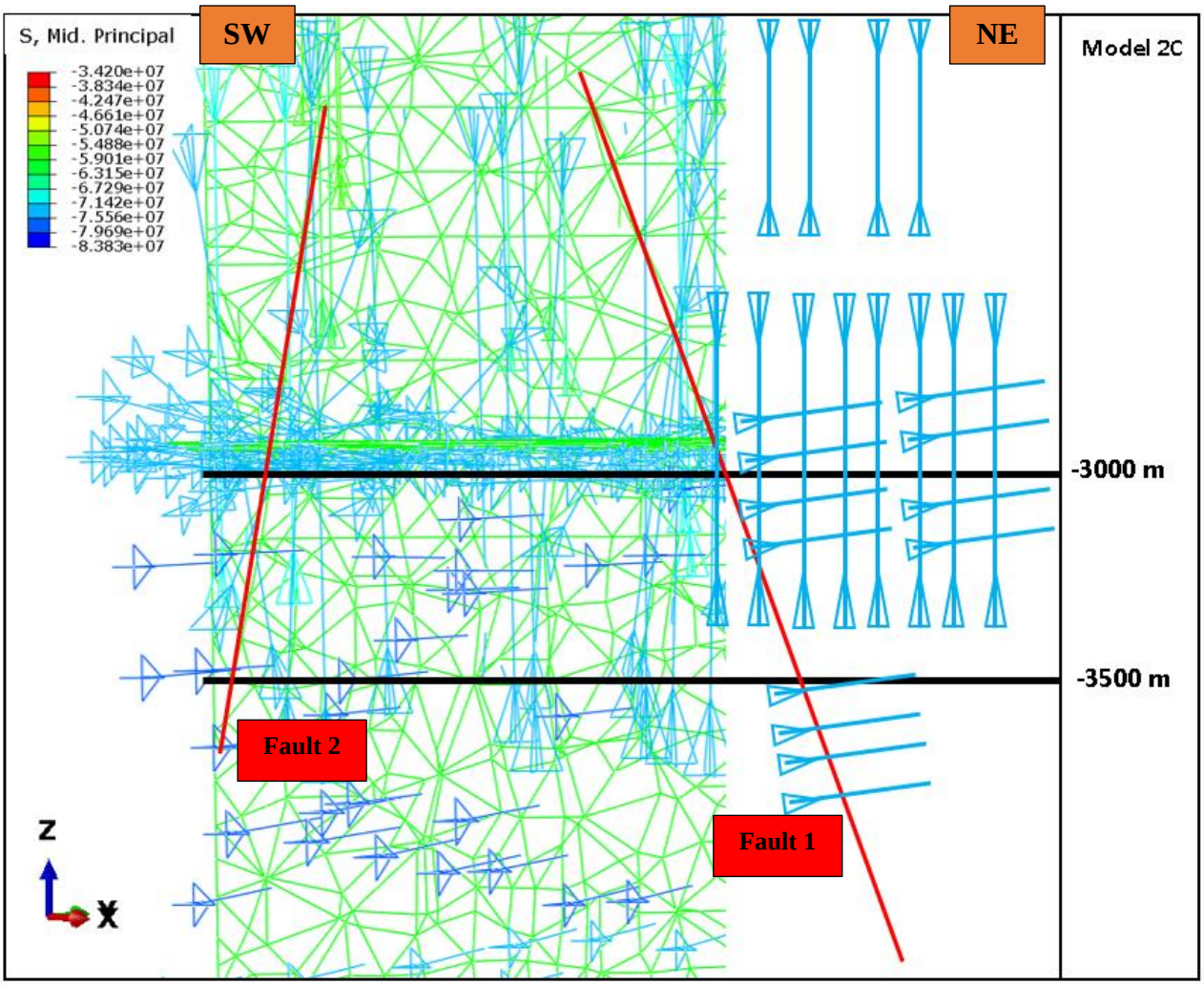

Figure 43. The intermediate principal stress orientation; cross-section 2

5.4.5. Fault analysis

The other principal stress calculation was conducted to understand the impact of the stress field on the faults. The stress state along a fault will impact its stability. Faults that were inactive could be reactivated due to several factors, such as the change in the state of stress and pore pressure. The analysis of lateral stress distribution around the fault is carried out to determine the preliminary condition of existing faults in the study area. The principal stresses were calculated in cross-section 2 at depth -3000 m. At this depth, the cross-section cut through two bounding faults (Figure 41).

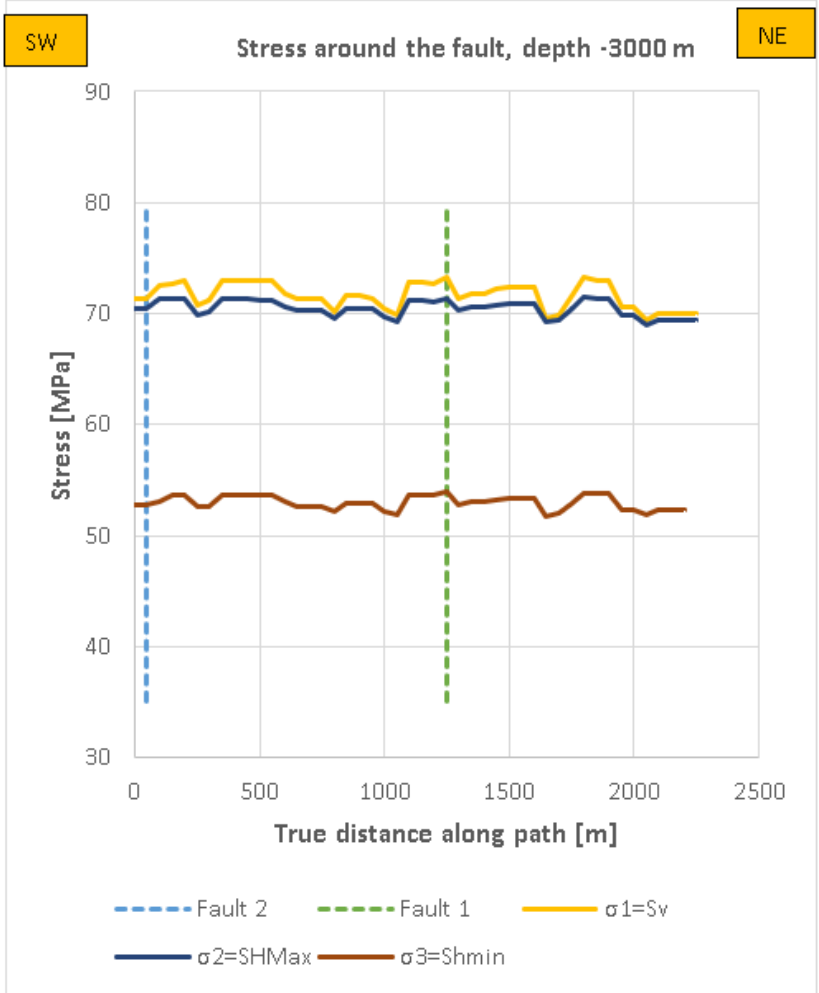

Figure 44. The magnitude of principal stresses around the faults

Figure 44 shows all principal stresses around two faults. The dashed line represents the location of two faults along the cross-section. However, the presence of fault 1 indicates a spike on the magnitudes of the principal stresses relative to the surrounding location. On the other hand, fault 1 shows an insignificant impact on the magnitudes of the principal stresses.

No stress rotations are observed around the fault point, and all principal stress orientation is oriented parallel with its acting stress. In addition, there is also no significant stress accumulation around fault 1 and 2. Therefore, those faults fault 1 and 2 is presumably inactive in the given state of stress. However, in order to determine the possible stress perturbations due to the presence of active faults,

one needs to observe the stress rotations from the borehole break-out orientation. The fluctuations of stress orientation in the borehole failure features indicate the presence of active faults.

In order to evaluate the slip tendency of fault 1 and 2, one can calculate the ratio of shear stress the normal stress. A fault is considered to be critically stressed if the ratio ($r = \tau/\sigma n$) exceeds the frictional strength coefficient (0.6-1). From the 3D geomechanical model, one can obtain the information on the dip and strike angle of the faults, including the state of stress around the fault plane (Table 10). Figure 45 shows the Mohr-Coulomb failure criterion for fault 1 and 2. Both Mohr's circle do not touch the failure envelope, indicates that faults are in stable condition under a given state of stress. Ratio shear stress to normal stress for fault 1 and 2 are 0.22 and 0.14, respectively.

Table 10. Stress state information

Source of stress state		**Unit**	**MPa**
Model	3D Geomechanical model 2C		
Fault 1 - Normal Faulting stress regime			
Depth	-3000 m	***Sv (S1)***	71.5
Nodes ID	81690	***SHMax (S2)***	70.4
Dip angle	72°	***Shmin (S3)***	52.8
Strike angle	320°	***Pp***	30.08
μ	0.6	***S_0***	0
Azimuth SHMax	325°	***Azimuth Shmin***	55°
Fault 2 – Normal faulting stress regime			
Depth	-3000 m	***Sv (S1)***	72
Nodes ID	81690	***SHMax (S2)***	70.7
Dip angle	80°	***Shmin (S3)***	53.1
Strike angle	320°	***Pp***	30.2
μ	0.6	***S_0***	0
Azimuth SHMax	325°	***Azimuth Shmin***	55°

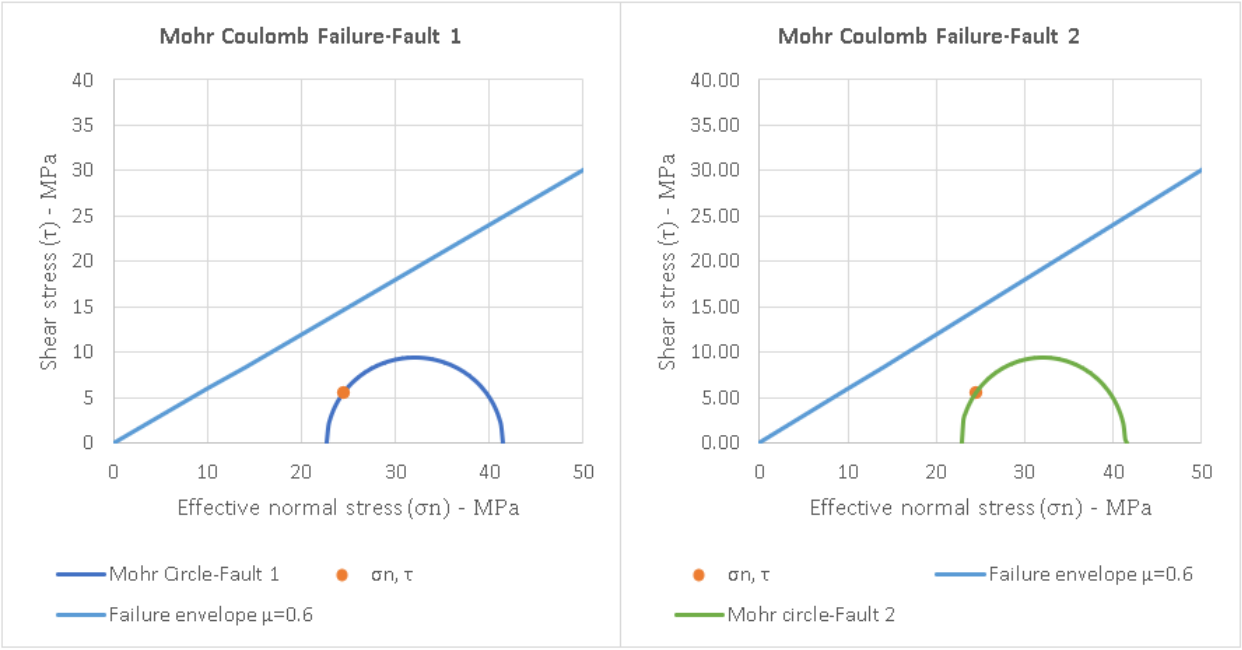

Figure 45. Mohr-Coulomb Failure for fault 1 and 2

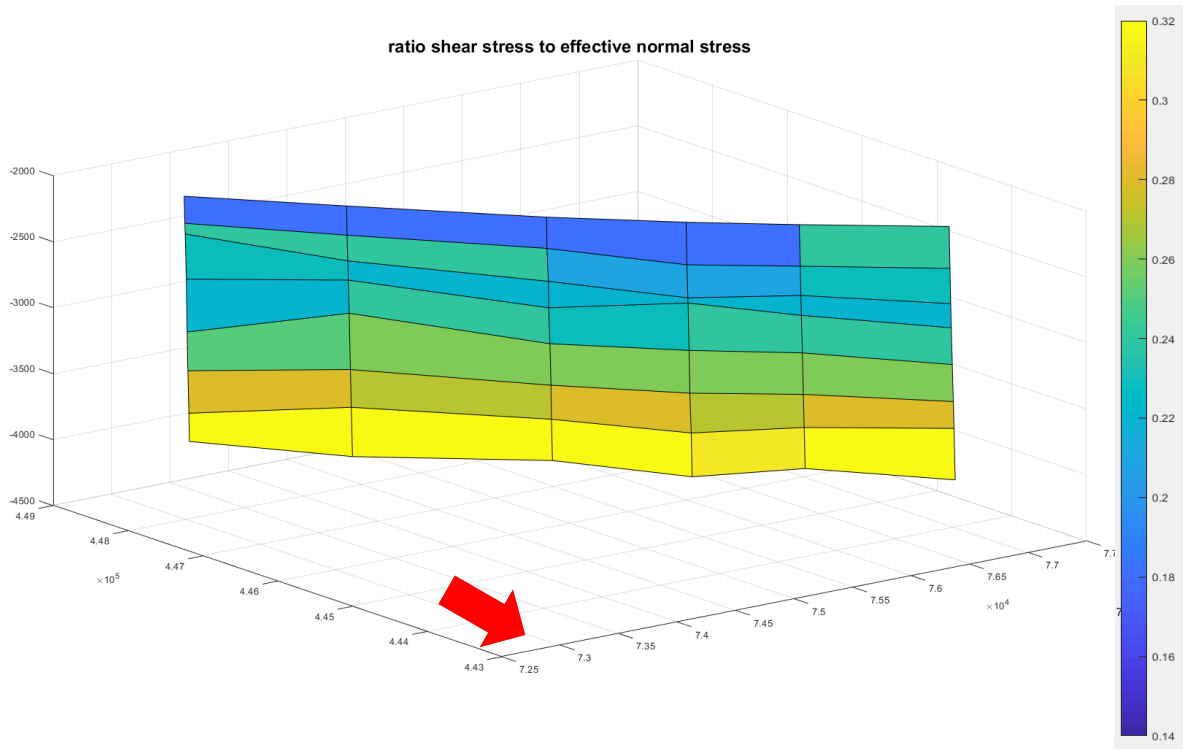

Figure 46. Perspective view of 3D faults with ratio shear stress to effective normal stress-fault 1

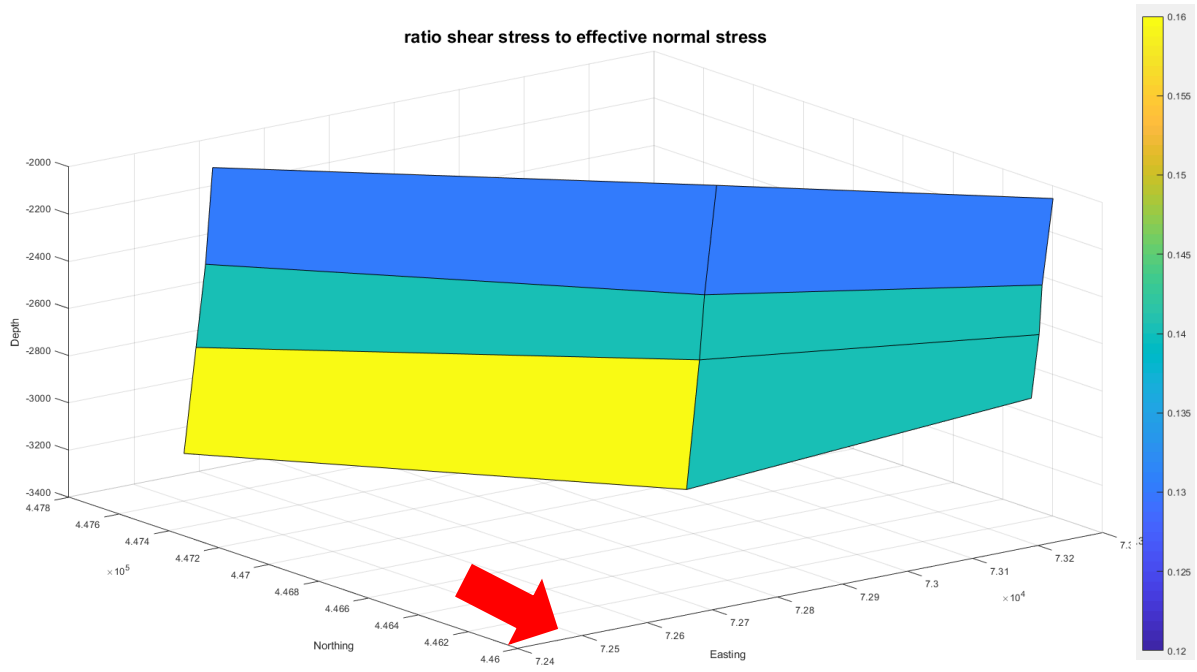

Figure 47. Perspective view of 3D faults with ratio shear stress to effective normal stress–fault 2

Figures 46 and 47 show the ratio ($r = \tau/\sigma n$) on faults 1 and 2. The stress states were obtained from 3D geomechanical-model 2C. The slip tendency in Figure 46 and 47 were calculated in the strike-slip faulting regime and normal faulting regime. The strike-slip faulting regime was calculated in the part of the fault, which has a depth of less than -3000 m, whereas the part of the fault that has a

depth of more than -3000 m was in normal faulting stress regime. Both fault 1 and fault 2 are inactive in the current stress field. The ratio ($r = \tau/\sigma n$) is less than $\mu = 0.6$

5.4.6. Model comparison

Figure 48 illustrates the comparison of the stress magnitude in the 1D and 3D model. The point example is taken from point C at a depth of -1500 m in cross-section 3 (Figure 49). It implies from the figure that there is a discrepancy in stress magnitudes between 1D and 3D model. The stress magnitude in the 1D model remains constant throughout the distance along the path in a cross-section, meanwhile the 3D model yields various stress magnitude along the path.

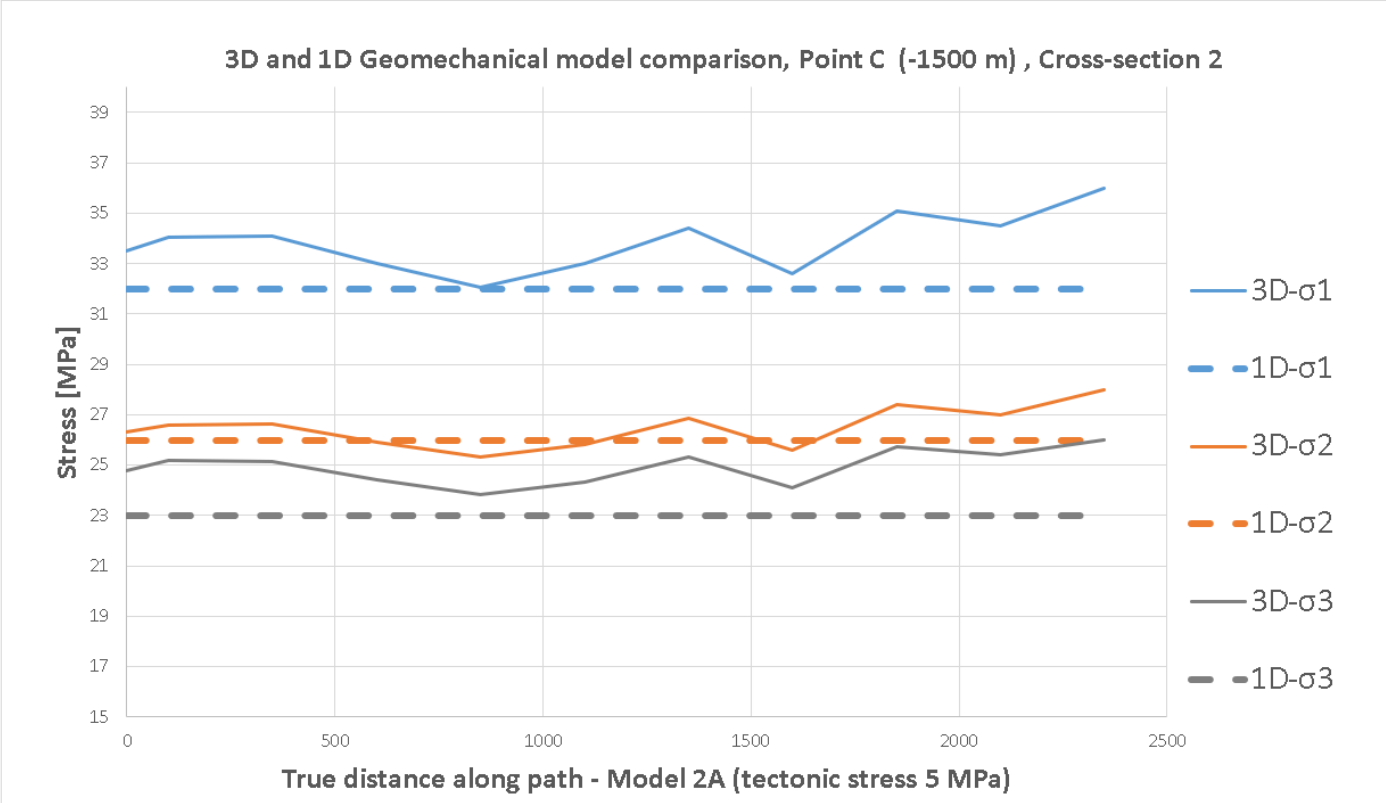

Figure 48. The comparison between 3D and 1D Geomechanical model

The 1D geomechanical model is a static model that only takes into account the rock parameters at a specific point where the well is situated. However, the 1D model is beneficial as a preliminary tool to estimate the current tectonic stress regime.

On the other hand, the stress magnitude in the 3D model shows spatial variability along the path. Because the 3D geomechanical model is constructed by taking into account the topography, lithology, geological structure (faults) as well as heterogeneity in rock properties. Therefore, a 3D geomechanical model can capture heterogeneous stress fields and carry out the dynamic simulation by using a finite element model (FEM). A tetrahedral mesh is composed of a static 3D structural model. All input parameters for FEM modeling, such as rock properties and initial stresses, are then directly mapped onto the tetrahedral mesh.

The other factor that caused the discrepancy between 1D and 3D models is the level of coarsening during 3D structural modeling. Coarsening element nodes is essential to limit processing time during

finite element simulations. Thus, this process also determines the level of resolution of the 3D model. The finer the element, the more realistic the model will become. Therefore, the discrepancy between the 1D geomechanical model and the 3D geomechanical model will be smaller.

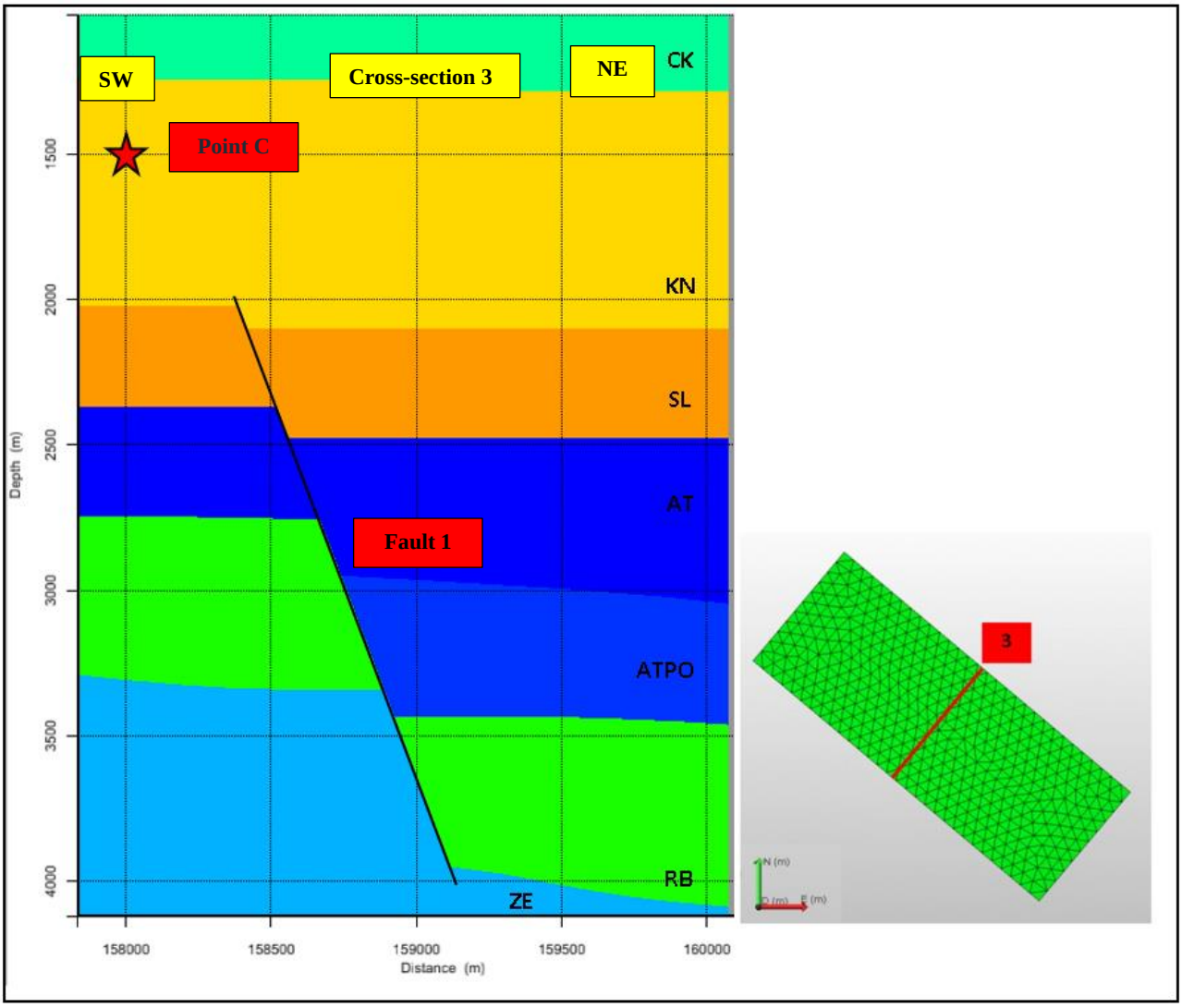

Figure 49. Cross-section 3 and the location of point C

Stratigraphy units: CK=Chalk group; KN=Rijnland group; SL=Schieland group; AT=Altena group; ATPO=Posidonia Shale RB=Lower Germanic Triassic group; ZE=Zechstein

5.4.7. Sensitivity analysis

Sensitivity analysis is carried out to find out how the density and Poisson's ratio will affect the principal stresses. The point sample was taken from point B, cross-section 1, at a depth of -4000 m (Figure 36). Model 2C was selected as a base case model to run the sensitivity analysis.

Sensitivity analysis-Density

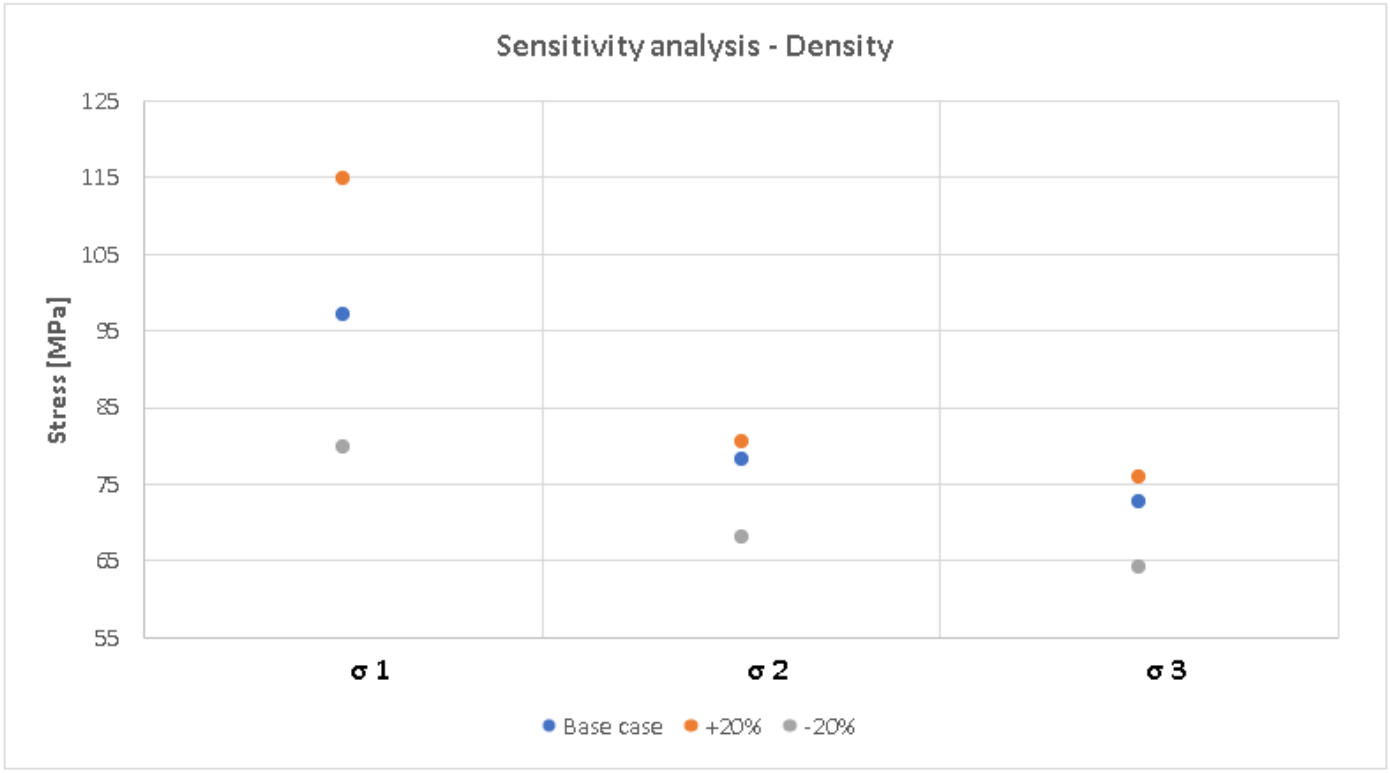

Figure 50. Sensitivity analysis - Density

Figure 50 displays the result of the sensitivity analysis. In this case, three different density values have defined. The first one is the base case with actual bulk density value comes from well log data. The second one is the base case + 20% bulk density, and the last one is the base case -20% density. The example point B is in a state of normal faulting regime.

Density has a more significant influence on the vertical stress (Sv). In this case, the Sv becomes the maximum principal stress (σ1) at a depth of -4000 m. The maximum principal stress oriented to the z-direction, which is coherence with vertical stress (Sv). By adding a 20% density from the base case, the maximum principal stress increase by almost 21%.

Furthermore, density has less impact on both the intermediate (σ2) and the minimum principal stress (σ3). Because both σ2 and σ3 are horizontal stresses in which Poisson’s ratio plays a significant role than density.

Sensitivity analysis-Poisson's ratio

The other parameter input for the geomechanical simulation is the Poisson's ratio. Similar to the density analysis, model 2C was selected as the base case scenario.

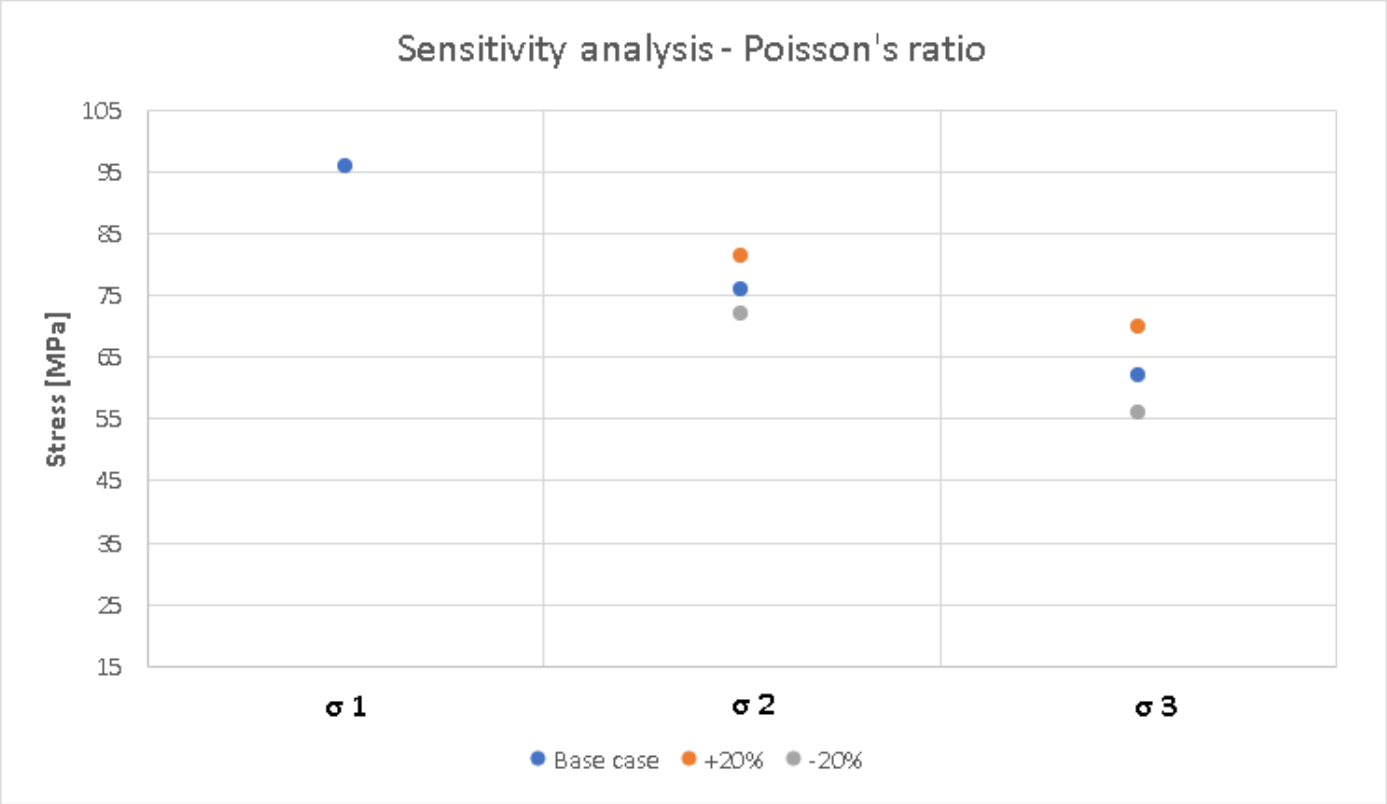

Figure 51. Sensitivity analysis – Poisson's ratio

Figure 51 displays the effect on varying Poisson's ratio value to the principal stresses. The most noticeable result is that the change in the Poisson's ratio does not influence the vertical stress (Sv). As mentioned earlier, the model used in this analysis has a normal faulting regime, where σ1 is the vertical stress (Sv). Thus, the parameter that plays a significant role in vertical stress (Sv) is only density and depth.

In addition, the effect of Poisson's ratio is more prominent on the magnitude of the minimum principal stress (Shmin). By adding a 20% Poisson's ratio from the base case, will increase the magnitude of the minimum horizontal stress (Shmin) by 13%. In this case, the minimum principal stress (σ3) is the minimum horizontal stress (Shmin). Meanwhile, by adding 20% Poisson's ratio to the model only increase 6.7% of maximum horizontal stress (SHMax) magnitude from the base case.

Minimum horizontal stress is practically approximated as fracture pressure in normal faulting stress regime. In addition, the minimum horizontal stress is a function of pore pressure, vertical stress, and Poisson's ratio, as depicted in equation 7.

5.4.8. Critically-stressed fractures analysis

In this section, simulation is carried out to evaluate which fractures and faults are critically stressed and closes to failure under the current stress field. However, there is a hypothesis introduced by (Barton et al., 1995), faulted and fractured hydraulically conductive rocks are those that critically stressed in the current stress field. This gives rise to the possibility that fracture data from well NLW-GT-01 might also come to be hydraulically conductive.

The fracture orientation is given as the angle of the fractures/faults normal vector relative to the maximum principal stress. The value of μ (coefficient of internal friction) and S_0 (cohesion) are usually obtained through triaxial rock mechanic tests in the laboratory. The value for μ is a general assumption between 0.6-1.0 as a study by Byerlee (1978) for a wide variety of crustal rocks. Also, the value of S_0 in this simulation was used for simplicity and not represent the actual field.

The fracture data in this analysis was a simple simulation and not represent the actual information in the field. However, the actual principal stresses were taken from the 3D finite element model 2C, at a depth of TVD -3984 m. There is a recent study about FMI analysis and interpretation of geological features in well NLW-GT-01 conducted by Maniar (2019). The FMI data sample in that study was also taken from depth around -3984 m. Therefore, some of the fracture dip angle data in this analysis are similar to data used in that study. The steeply dipping fractures from the FMI logs have dip angles ranging from 58° to 90° (Maniar, 2019).

Table 11. Stress state information

Source of stress state		Unit	MPa
Model	3D Geomechancal model 2C	***Sv (S1)***	97.25
Depth	-3984 m	***Shmin (S3)***	67.05
Nodes ID	86194	***Pp***	39.77
Tectonic regime	Normal faulting regime	***S_0***	0
			[-]
		μ	0.6

In this case, the minimum principal stress (σ3) is Shmin, while the maximum principal stress (σ1) is the vertical stress (Sv). Thus, the stress state is in a normal fault regime, and a fracture strike does not matter. Fracture dip will be taken into account, and it equals to β (the angle between fracture normal and the maximum principal stress). Pore pressure is considered to be a normal hydrostatic pressure (NHP).

Table 12 contains the fracture's dipping angle data. Furthermore, shear stress (τ) and effective normal stress (σn) are calculated by using equations 1 and 2. The fracture features are considered to be active when $\frac{\tau}{\sigma_n} \geq \mu$ and when Coulomb Failure Function (CFF) $\tau \geq \tau f = C + \mu(\sigma_{ft-} P_p)$.

Table 12. Dipping angle data

Dipping angle of fractures					
10°	25°	44°	75°	58°	88°
9°	40°	35°	55°	71°	85°
17°	43°	25°	65°	69°	
4°	24°		70°		

Figure 52 illustrates the result of the failure criterion from several fracture dip angle data. All faults/fractures appear to be inactive in the current stress field. Not a single fractures touch the failure envelope of $\tau = 0.6$.

Furthermore, in this normal condition, pore pressure perturbations would cause fractures to slip, for example, during the fluid injection process in geothermal production activity. Further calculation was carried out to determine the pore pressure perturbation necessary to re-activate those fractures. The following table contains some fractures with its orientations that were used for further simulation.

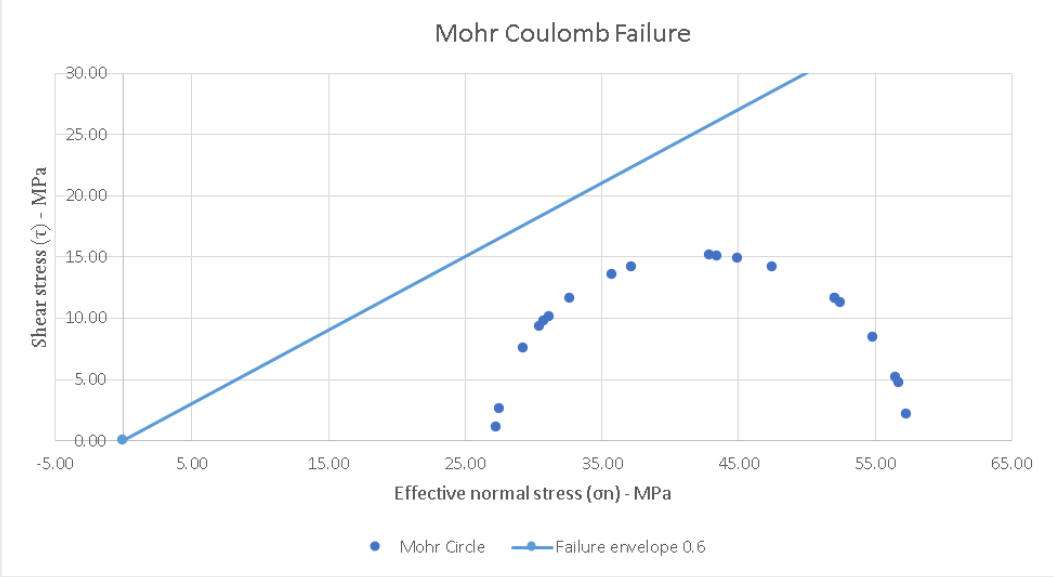

Figure 52. Mohr circle for failure criterion

Pore pressure perturbation is calculated by using the following equation :

$$P_p = \frac{S_1 + S_3}{2} + \frac{S_1 - S_3}{2} cos2\beta - \frac{\tau}{\mu} \quad (14)$$

To be concluded, from equation 13, the magnitude of the increase in pore pressure that would cause fractures to slip is 14.98 MPa. Figure 51 illustrates the final position of some fractures that would be in a failure state should there be an increase in pore pressure up to 14.98 MP from the initial state. Fractures that have a dipping angle 55°,58°,65°,69°, 70°, and 71° are now critically stressed.

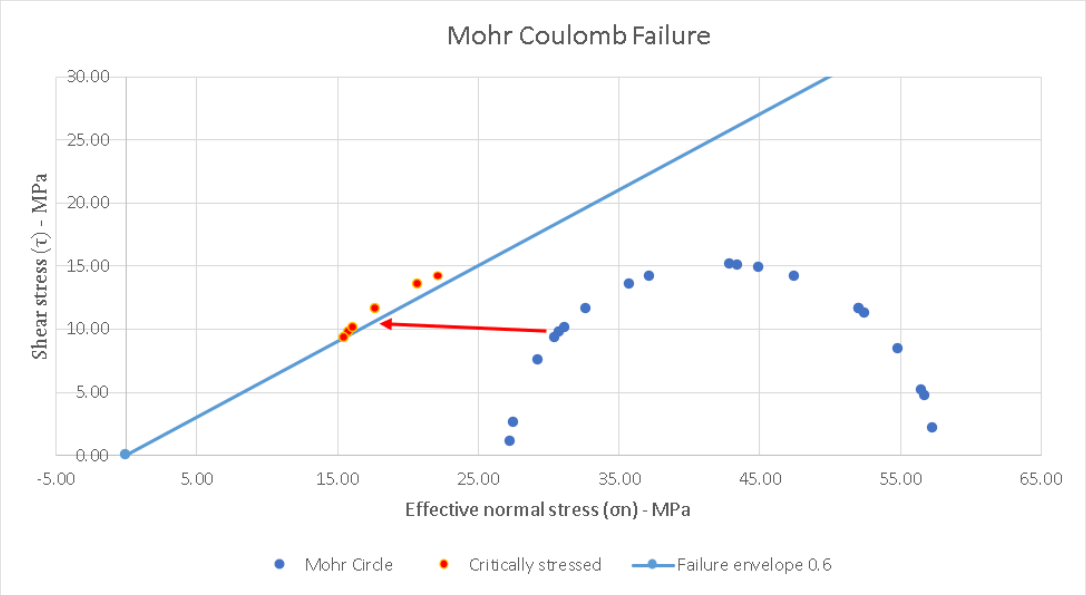

Figure 53. Mohr circle for critically-stressed fractures after pore pressure perturbation

Sensitivity analysis

The sensitivity analysis is carried out by varying the value of Pore pressure (Pp) and μ (coefficient of internal friction). The aim of this analysis is to determine the effect of μ (coefficient of internal friction) and Pore pressure on the pore pressure perturbations, in order to activate some optimally oriented fractures to slip. The samples that are used in this analysis are fractures that have a dipping angle of 55°,58°,65°,69°, 70°, and 71°

Table 13. Sensitivity analysis for critically stressed fracture

Base case μ			Base case Pp		
-20%		+20%	-20%		+20%
0.48	0.6	0.72	31.82 MPa	39.77MPa	47.72 MPa

It can be concluded In Figure 54 and Figure 55, that 17.56 MPa pore pressure increments are necessary to reactivate optimally oriented faults when the value coefficient of internal friction (μ) is set to be 0.72. Whereas, it requires 11.11 MPa pore pressure increments to reactivate fractures when the value coefficient of internal friction (μ) is decreased by 20% from the base case (Figure 56 and Figure 57). However, with μ = 0.48, the fractures are remaining in stable condition.

Meanwhile, it requires 7 MPa pore pressure increments to reactivate fractures if fractures in a slightly overpressure zone (Figure 58 and Figure 59). Also, as much as 22.93 MPa pore pressure increments are needed to reactivate fractures when in under pressure zone.

On the other hand, when pore pressure decreases, the mohr circle moves to the right and thus decreasing the possibility of failure. In a situation when pore pressure elevates, the Mohr circle

moves to the left and thus increasing the chance of failure. In addition, the smaller the coefficient friction, the closer the Mohr circle to the failure envelope.

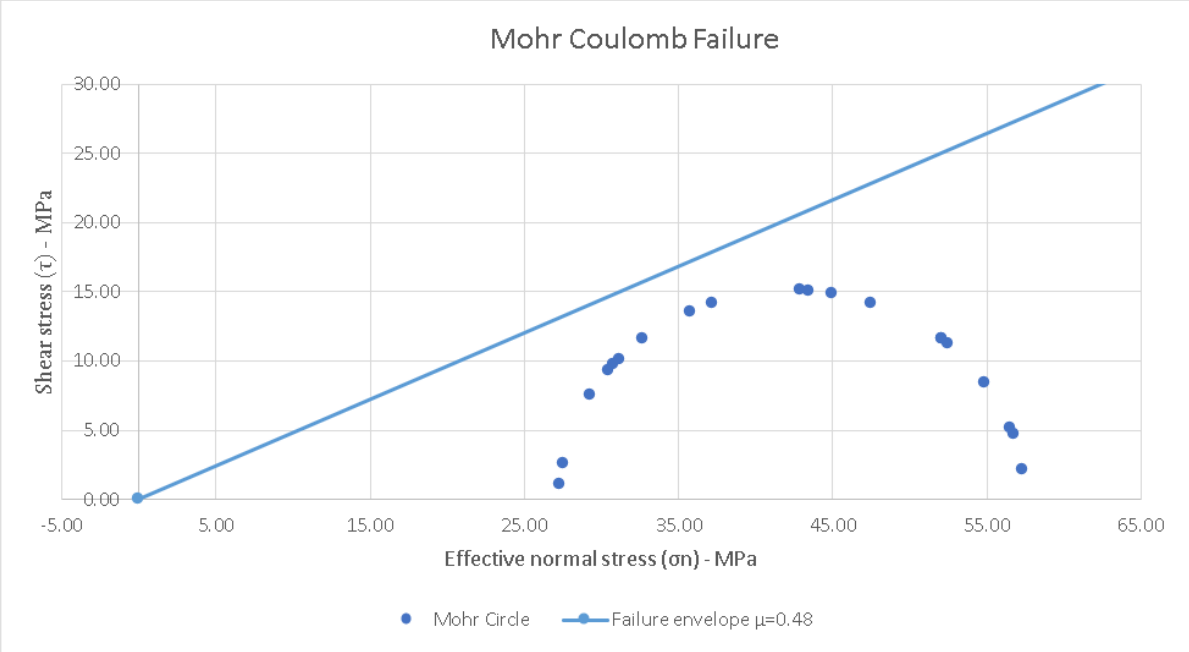

Figure 54. Mohr circle for critically-stressed fractures (μ = 0.48 and Pp=39.77 MPa)

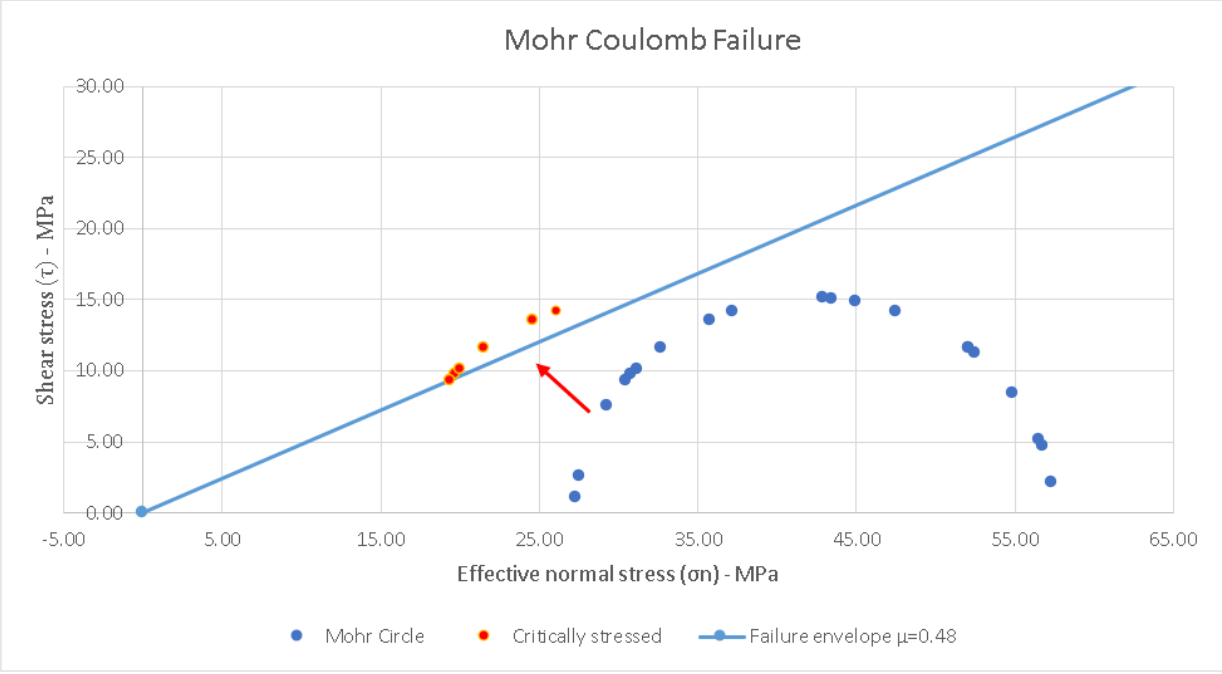

Figure 55. Mohr circle for critically-stressed fractures, after stress perturbations (μ = 0.48 and Pp=39.77 MPa)

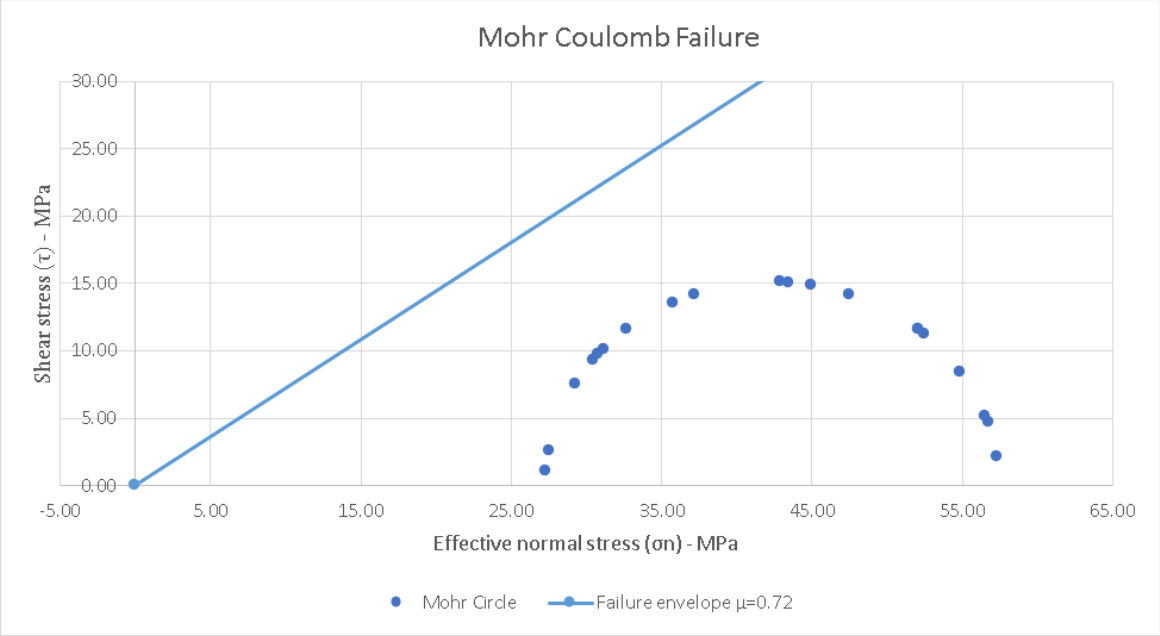

Figure 56. Mohr circle for critically-stressed fractures (μ = 0.72 and Pp=39.77 MPa)

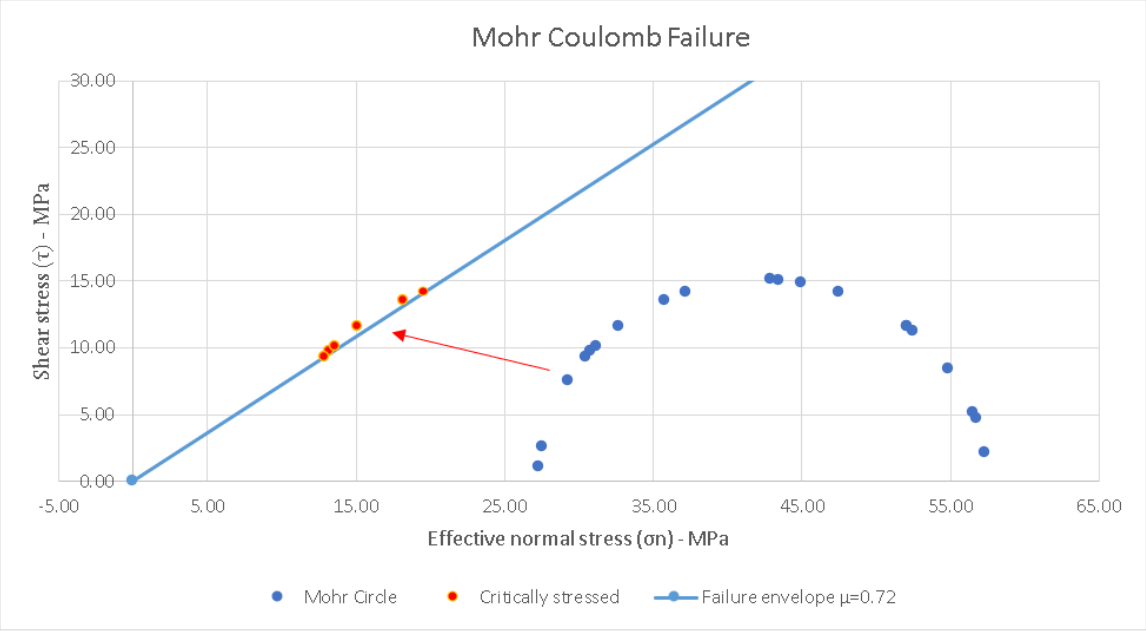

Figure 57. Mohr circle for critically-stressed fractures, after stress perturbations (μ = 0.72 and Pp=39.77 MPa)

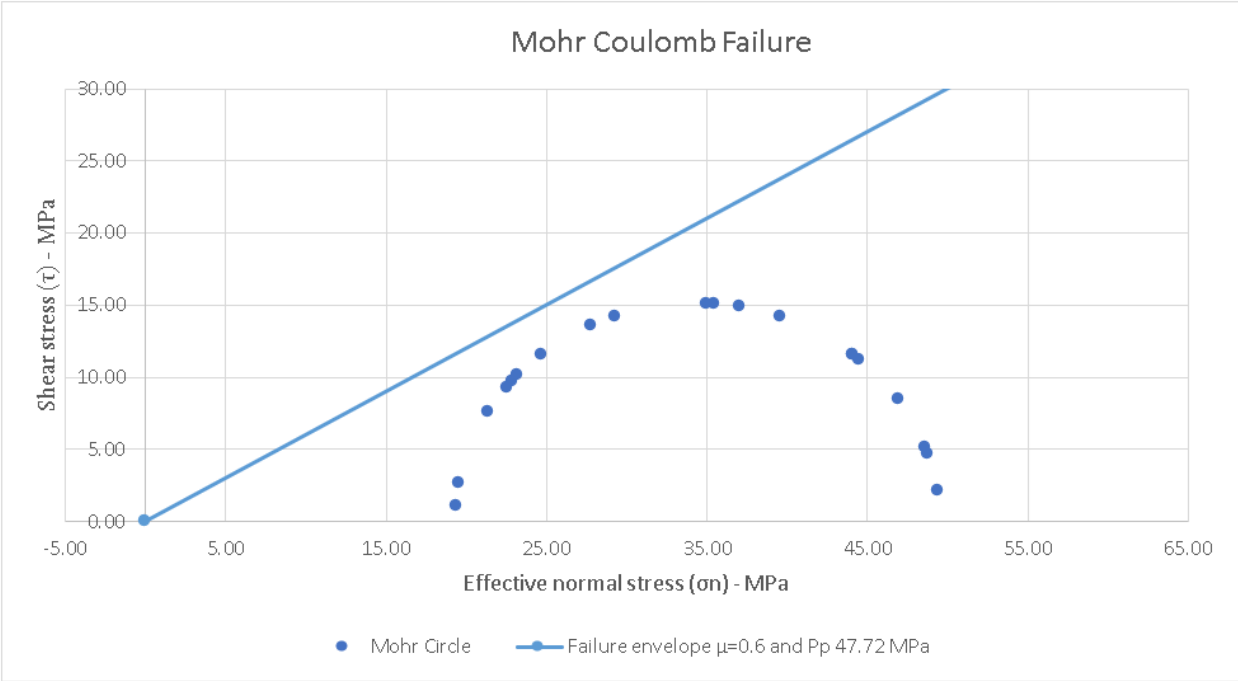

Figure 58. Mohr circle for critically-stressed fractures (μ = 0.6 and Pp=47.72 MPa)

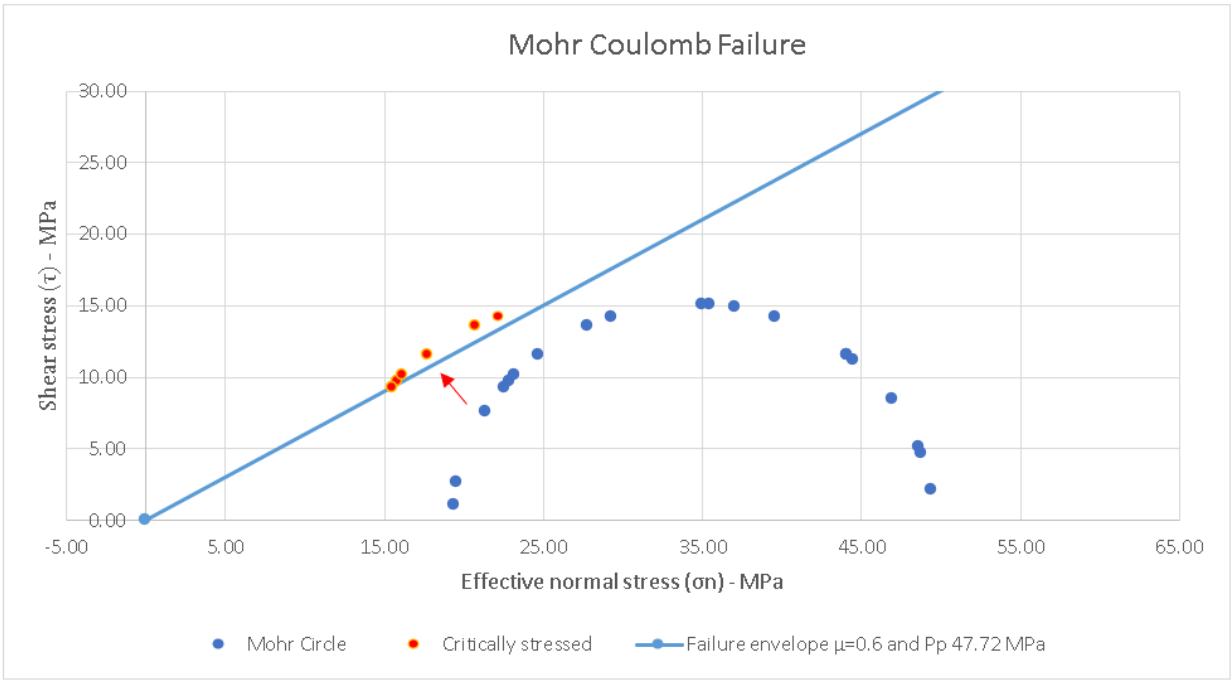

Figure 59. Mohr circle for critically-stressed fractures-after stress perturbation (μ = 0.6 and Pp=47.72 MPa)

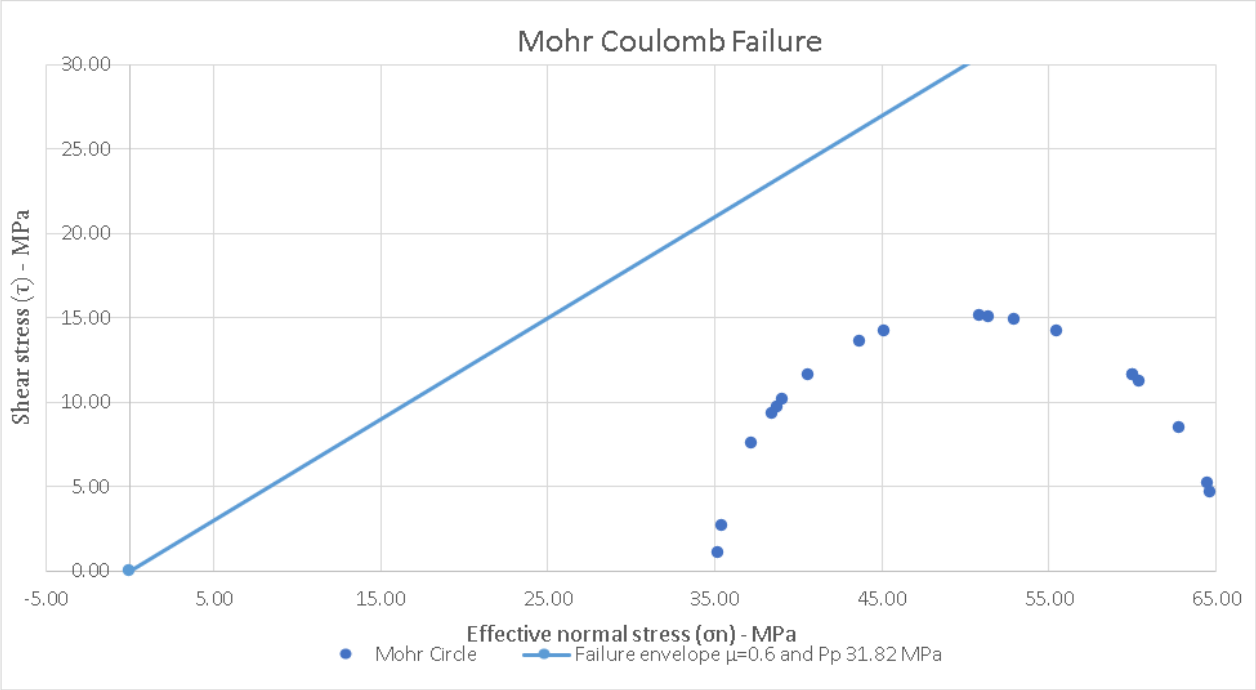

Figure 60. Mohr circle for critically-stressed fractures (μ = 0.6 and Pp=31.82 MPa)

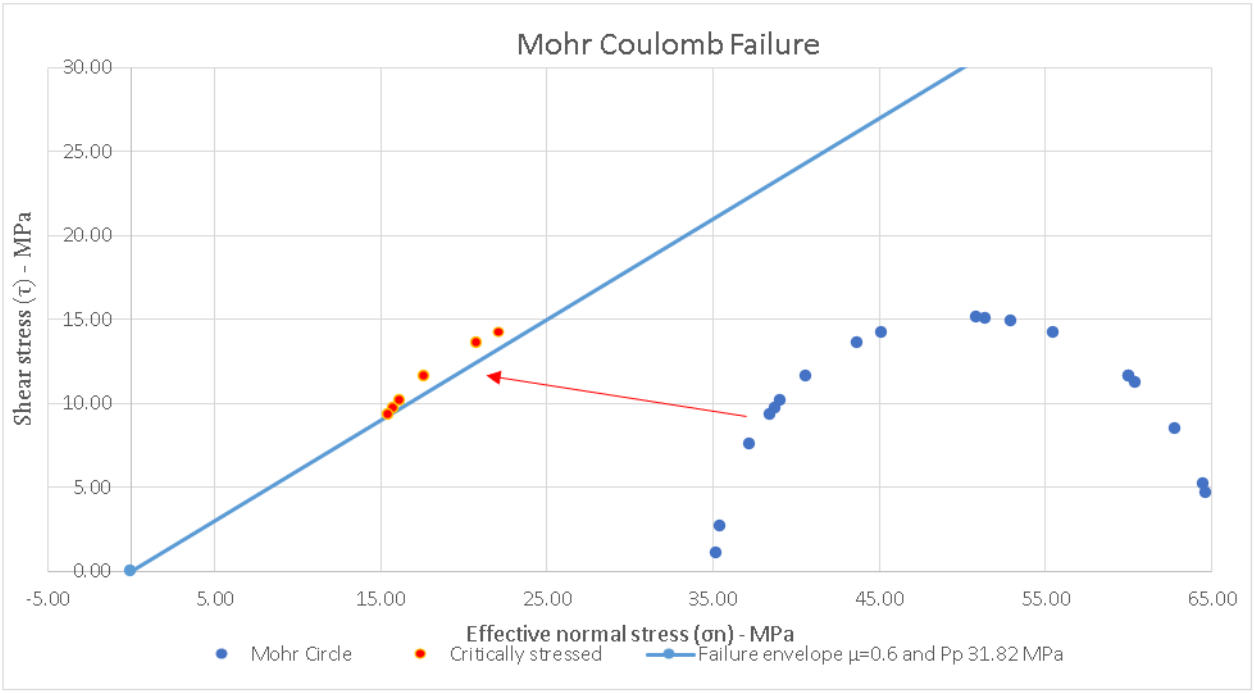

Figure 61. Mohr circle for critically-stressed fractures-after stress perturbation (μ = 0.6 and Pp=31.82 MPa)

This page is left blank intentionally

6 Conclusion & Recommendation

6.1. Conclusion

The study area is located at the geothermal field in De Lier, the Netherlands. The aim of this study is to develop a 3D geomechanical model to comprehend the state of stress in the Lower Germanic Triassic group as one of the targets for deep geothermal production. The Main Buntsandstein subgroup, as the part of Lower Germanic Triassic group, lies at a depth of -3000 m until -4000 m. However, problems that could arise when exploring a deep reservoir, among other things, is the lack of a site-specific geomechanical model. Such models can be used to predict reservoir response under complex conditions. The 1D and 3D geomechanical models were then constructed to comprehend the principal stresses distribution in the reservoir.

The size of the 3D model is approximately 5.92 km x 2.25 km. The base of the model was extended to -5500 m to prevent the influence of the boundary effects while modeling a 3D finite element. The first process was involving the horizon and fault interpretations. There are three interpreted faults and seven horizons used as a primary input in 3D geomechanical modeling. Despite the low impedance contrast in seismic data at a depth around the Lower Germanic Triassic group, the result is still reasonably good, and the vertical accuracy reaches up to 24 m. The Lower Germanic Triassic group is divided into two different blocks. One block is situated at the up-thrown block and the other at the down-thrown block. Those two blocks were separated by one normal fault.

The data used in local stress orientation analysis was taken from previous studies conducted by Van Eijs and Dalfsen (2004), Mechelse (2017), and Rondeel and Everaars (1993). In addition, the stress database from WSM (World Stress Map) was also used in this study. The local stress orientation indicates an NW-SE of SHMax orientation, with azimuth ranging from 311°N – 330°N. This result also coherence with regional stress orientation in western Europe that shows the uniform NW-SE trend, with a mean value of SHMax azimuth N325°. Furthermore, the azimuth of SHMax is one of the important parameters for the 3D geomechanical simulation.

The 1D and 3D geomechanical models are constructed and divided into four different models. Those models were applied by varying the magnitude of tectonic stress. Model 1 is a gravity-only model that is based on the assumption that gravity is the only source of stress. Meanwhile, the other three models (Model 2A, 2B, and 2C) used tectonic stress in the simulation as a source of stress. The magnitude of tectonics stress varies from 5, 10, and 20 MPa.

The 1D geomechanical models were based on stratigraphy of well LIR-45, NLW-GT-01 and LIR-43. The 1D gravity-only model indicates a normal fault stress regime at all depths. Thus, the vertical stress becomes the maximum principal stress.

The stress permutations are observed in all gravity-tectonic models (Model 2A, 2B, and 2C), at which the principal stresses direction changes throughout the depth. However, the stress regime transition is controlled by the depth rather than by stratigraphy units. The change in stress faulting regime is because the vertical stress (Sv) increases at a higher rate compared to the horizontal stresses. Therefore, at a certain depth, the vertical stress (Sv) will become the maximum principal stress.

A reverse fault stress regime is observed at the top-most of the model, followed by a strike-slip fault and a normal fault stress regime at the bottom-most of the model 2A, 2B, and 2C. The bigger the tectonic stress imposed on the model, the wider the compressive fault stress regime zone (reverse fault and strike-slip fault) will be formed. Therefore, the tectonic boundaries shift downward from model 2A to model 2C.

The 3D geomechanical model can be used to understand stress distribution in a lateral direction. For example, at a depth around -3000 m in model 2C, a transition zone faulting regime occurs. The 3D geomechanical model gives clarity on how the intermediate principal stress plays its role. In this case, the intermediate principal stress has two directions, to the vertical direction and horizontal direction. It implies that at a particular depth, the vertical stress becomes the intermediate principal stress. However, a few meters deeper, the maximum horizontal stress becomes the intermediate principal stress. It also can be implied from cross-section analysis that principal stresses can vary by the presence of different stratigraphic units and geological structures (faults and fractures).

In addition, the presence of the faults in the model does not influence the magnitude and orientation of the principal stresses and vice versa. Fault 1 and 2 are considered to be inactive under the given state of stress. The 3D geometrical model can be used to study the 3-D pattern of forces acting along faults in a particular tectonic stress field.

Density and Poisson's ratio are, among others, two input parameters for stress calculation. The magnitude of the vertical stress (Sv) could rise to 21% by adding a 20% density from the base case at a depth of -4000 m. The changing on density also impacts the horizontal stresses but not as significant as to the vertical stress (Sv). On the other hand, the magnitude of the minimum horizontal stress is more affected by the change in Poisson's ratio. By adding a 20% Poisson's ratio from the base case, will increase the magnitude of the minimum horizontal stress (Shmin) by 13%.

The 3D geomechanical model can be used to asses whether fractures or faults are active or inactive under the current stress field. An example of fracture data was taken into a simulation under normal faulting stress regime and normal hydrostatic pressure. The result gives information that all fractures appear to be inactive under the current stress state (Sv=97.25 MPa; Shmin=67.05 MPa). However, it requires an additional pore pressure perturbation up to 14.98 MPa from the initial state to cause some fractures to slip. Therefore, pore pressure and friction coefficient are, among other things, the significant factors that influence slip instability.

The knowledge about whether fractures or faults are active today could be beneficial to address reservoir challenges in geothermal production, especially in a tight reservoir. In a deep geothermal project, where the targeted formation lies down to -4000 m, induced fractures are used to enhance permeability. On the other hand, fluid injection to the subsurface will trigger pore perturbations that later could re-activate the existing fractures and faults. By knowing the current stress state, one could predict the reservoir behavior before field development.

6.2. Recommendation

The 3D geomechanical model in this study can be improved by adding some more data into the model, such as :

- Extended Leak-of-test or mini-frac to determine an accurate estimation for minimum horizontal stress (Shmin)
- An extensive study on the use of borehole failures features, such as borehole-breakout (BO) and drilling-induced fracture to constraint the possible range of maximum horizontal stress (SHMax)
- Study on image log to verify the stress orientations and perturbations near geological structures such as faults and salt domes.
- Conducted a rock a triaxial laboratory test to calibrate the static and elastic rock properties such as Young's Modulus, internal friction coefficient (μi), and cohesion (S) in both overburden and reservoir zone.
- Actual pore pressure and mud-weight data can be used for further studies, such as managing wellbore stability and calculating the expected field subsidence during production.

This page is left blank intentionally

Bibliography

Agheshlui, H., Sedaghat, M. H., and Matthai, S. J. J. o. G. R. S. E., 2018, Stress influence on fracture aperture and permeability of fragmented rocks, v. 123, no. 5, p. 3578-3592.

Ames, R., and Farfan, P., 1996, The environments of deposition of the Triassic Main Buntsandstein Formation in the P and Q quadrants, offshore the Netherlands, Geology of Gas and Oil under the Netherlands, Springer, p. 167-178.

Anderson, E. M., 1951, The dynamics of faulting and dyke formation with applications to Britain, Hafner Pub. Co.

Azit, R., Ismail, M. A. M., and Mahmood, N. J. J. T., 2016, IN-SITU STRESS MEASUREMENT BY OVERCORING AND HYDRAULIC FRACTURING OF PAHANG-SELANGOR RAW WATER TRANSFER PROJECT, v. 78, no. 8-6.

Barton, C. A., Zoback, M. D., and Moos, D. J. G., 1995, Fluid flow along potentially active faults in crystalline rock, v. 23, no. 8, p. 683-686.

Batchelor, A., 1984, Geothermal reservoir engineering: Malcolm A. Grant, E MG Donaldson and Paul F. Bixley Academic Press, New York, 1982, Elsevier.

Bell, J., Gough, D. J. E., and letters, p. s., 1979, Northeast-southwest compressive stress in Alberta evidence from oil wells, v. 45, no. 2, p. 475-482.

Bertotti, G., de Graaf, S., Bisdom, K., Oskam, B., Vonhof, H. B., Bezerra, F. H., Reijmer, J. J., and Cazarin, C. L. J. B. R., 2017, Fracturing and fluid-flow during post-rift subsidence in carbonates of the Jandaíra Formation, Potiguar Basin, NE Brazil, v. 29, no. 6, p. 836-853.

Bonté, D., Van Wees, J.-D., and Verweij, J. J. N. J. o. G., 2012, Subsurface temperature of the onshore Netherlands: new temperature dataset and modelling, v. 91, no. 4, p. 491-515.

BV, N. A. M. J. N., Assen, 2013, A technical addendum to the winningsplan Groningen 2013 subsidence, induced earthquakes and seismic hazard analysis in the Groningen field.

Byerlee, J., 1978, Friction of rocks, Rock friction and earthquake prediction, Springer, p. 615-626.

Cacace, M., Kaiser, B. O., Lewerenz, B., and Scheck-Wenderoth, M. J. G., 2010, Geothermal energy in sedimentary basins: What we can learn from regional numerical models, v. 70, p. 33-46.

Cox, J. W., The high resolution dipmeter reveals dip-related borehole and formation characteristics, *in* Proceedings SPWLA 11th Annual Logging Symposium1970, Society of Petrophysicists and Well-Log Analysts.

De Jager, J., Doyle, M., Grantham, P., and Mabillard, J., 1996, Hydrocarbon habitat of the West Netherlands Basin, Geology of gas and oil under the Netherlands, Springer, p. 191-209.

De Jager, J. J. G. o. t. N., 2007, Geological development, p. 5-26.

Den Hartog Jager, D., 1996, Fluviomarine sequences in the Lower Cretaceous of the West Netherlands Basin: correlation and seismic expression, Geology of gas and oil under the Netherlands, Springer, p. 229-241.

Donselaar, M. E., Groenenberg, R. M., and Gilding, D. T., Reservoir geology and geothermal potential of the Delft Sandstone Member in the West Netherlands Basin, *in* Proceedings Proceedings World Geothermal Congress2015.

Duin, E., Doornenbal, J., Rijkers, R., Verbeek, J., and Wong, T. E. J. N. J. o. G., 2006, Subsurface structure of the Netherlands-results of recent onshore and offshore mapping, v. 85, no. 4, p. 245.

Fuchs, K., and Müller, B. J. N., 2001, World stress map of the Earth: A key to tectonic processes and technological applications, v. 88, no. 9, p. 357-371.

Geluk, M., Plomp, A., and Van Doorn, T. H., 1996, Development of the Permo-Triassic succession in the basin fringe area, southern Netherlands, Geology of Gas and Oil under the Netherlands, Springer, p. 57-78.

Geluk, M., and Röhling, H.-G. J. G. e. M., 1997, High-resolution sequence stratigraphy of the Lower Triassic ‘Buntsandstein’in the Netherlands and northwestern Germany, v. 76, no. 3, p. 227-246.

Geluk, M. C., 2005, Stratigraphy and tectonics of Permo-Triassic basins in the Netherlands and surrounding areas, Utrecht University.
Heffer, K. J. G. S., London, Special Publications, 2015, Percolation of the interacting elastic stress fields of aligned cracks as an alternative explanation of critical crack densities, v. 409, no. 1, p. 31-47.
Heidbach, O., Rajabi, M., Reiter, K., and Ziegler, M. O., 2019, World Stress Map, *in* Sorkhabi, R., ed., Encyclopedia of Petroleum Geoscience: Cham, Springer International Publishing, p. 1-8.
Hillis, R. J. E. G., 2000, Pore pressure/stress coupling and its implications for seismicity, v. 31, no. 2, p. 448-454.
Hinkofer, T., 2017, Geomechanical Characterization of the Buntsandstein including a Fracture Model.
Jaeger, J. C., Cook, N. G., and Zimmerman, R., 2009, Fundamentals of rock mechanics, John Wiley & Sons.
Kiersnowski, H. J. G. S., London, Special Publications, 2013, Late Permian aeolian sand seas from the Polish Upper Rotliegend Basin in the context of palaeoclimatic periodicity, v. 376, no. 1, p. 431-456.
Klein, R., and Barr, M., Regional state of stress in Western Europe, *in* Proceedings ISRM International Symposium1986, International Society for Rock Mechanics and Rock Engineering.
Kortekaas, M., Böker, U., Van der Kooij, C., and Jaarsma, B. J. G. S., London, Special Publications, 2018, Lower Triassic reservoir development in the northern Dutch offshore, v. 469, no. 1, p. 149-168.
Kramers, L., Van Wees, J.-D., Pluymaekers, M., Kronimus, A., and Boxem, T. J. N. J. o. G., 2012, Direct heat resource assessment and subsurface information systems for geothermal aquifers; the Dutch perspective, v. 91, no. 4, p. 637-649.
Limberger, J., Boxem, T., Pluymaekers, M., Bruhn, D., Manzella, A., Calcagno, P., Beekman, F., Cloetingh, S., van Wees, J.-D. J. R., and Reviews, S. E., 2018, Geothermal energy in deep aquifers: A global assessment of the resource base for direct heat utilization, v. 82, p. 961-975.
Maniar, Z., 2019, Reservoir quality analysis of the Triassic sandstones in the Nederweert and Naaldwijk areas: A post-mortem study.
Mechelse, E., 2017, The in-situ stress field in the Netherlands: Regional trends, local deviations and an analysis of the stress regimes in the northeast of the Netherlands.
Müller, B., Zoback, M. L., Fuchs, K., Mastin, L., Gregersen, S., Pavoni, N., Stephansson, O., and Ljunggren, C. J. J. o. G. R. S. E., 1992, Regional patterns of tectonic stress in Europe, v. 97, no. B8, p. 11783-11803.
Pharaoh, T., Dusar, M., Geluk, M., Kockel, F., Krawczyk, C., Krzywiec, P., Scheck-Wenderoth, M., Thybo, H., Vejbæk, O., and Van Wees, J., 2010, Petroleum geological atlas of the Southern Permian Basin area.
Rafaelsen, B. J. U. T. L. S., Tromso, Norway, 2006, Seismic resolution and frequency filtering.
Raffensperger, J. P., and Vlassopoulos, D. J. H. J., 1999, The potential for free and mixed convection in sedimentary basins, v. 7, no. 6, p. 505-520.
Rondeel, H., and Everaars, J. J. E. m. o. n. d. r. t. g. e. a. i. N.-N. H. K. N. M. I., 1993, Spanning in noordoost Nederland, een breakoutanalyse.
Rondeel, H. E., Batjes, D. A. J., and Nieuwenhuijs, W. H., 1996, Geology of Gas and Oil under the Netherlands: Selection of papers presented at the 1993 International Conference of the American Association of Petroleum Geologists, held in The Hague, Springer Science & Business Media.
Rouchet, J. d. J. A. b., 1981, Stress fields, a key to oil migration, v. 65, no. 1, p. 74-85.
Straathof, D., 2012, Costs of Deep Geothermal Energy in the Netherlands, Petten: ECN.
Terzaghi, K. J. E. N.-R., 1925, Principles of soil mechanics, v. 95, no. 19-27, p. 19-32.
Van Adrichem Boogaert, H., and Kouwe, W., 1993, Stratigraphic nomenclature of the Netherlands, revision and update by RGD and NOGEPA.
Van Adrichem Boogaert, H., and Kouwe, W. J. R. G. D., 1997, Stratigraphic Nomenclature of the Netherlands, Revision and Update by RGD and NOGEPA, Meded, v. 50.
Van Balen, R., Van Bergen, F., De Leeuw, C., Pagnier, H., Simmelink, H., Van Wees, J., and Verweij, J. J. N. J. o. G., 2000, Modelling the hydrocarbon generation and migration in the West Netherlands Basin, the Netherlands, v. 79, no. 1, p. 29-44.

Van Eijs, R., and Dalfsen, W. J. T.-N. I., 2004, Borehole observations of maximum horizontal stress orientations in the Dutch upper crust, p. 11-14.
Van Hulten, F., and Poty, E. J. G. J., 2008, Geological factors controlling Early Carboniferous carbonate platform development in the Netherlands, v. 43, no. 2-3, p. 175-196.
Van Wees, J.-D., Fokker, P. A., Van Thienen-Visser, K., Wassing, B. B., Osinga, S., Orlic, B., Ghouri, S. A., Buijze, L., and Pluymaekers, M. J. N. J. o. G., 2017, Geomechanical models for induced seismicity in the Netherlands: Inferences from simplified analytical, finite element and rupture model approaches, v. 96, no. 5, p. s183-s202.
Van Wees, J.-D., Kramers, L., Juez-Larré, J., Kronimus, A., Mijnlieff, H., Bonte, D., van Gessel, S., Obdam, A., and Verweij, H., Thermo GIS: an integrated web based information system for geothermal exploration and governmental decision support for mature oil and gas basins, *in* Proceedings Proceedings World Geothermal Congress 20102010, p. 7.
Verweij, J., Simmelink, H., Underschultz, J., and Witmans, N. J. N. J. o. G., 2012, Pressure and fluid dynamic characterisation of the Dutch subsurface, v. 91, no. 4, p. 465-490.
Willems, C., Nick, H., Goense, T., and Bruhn, D. J. G., 2017, The impact of reduction of doublet well spacing on the Net Present Value and the life time of fluvial Hot Sedimentary Aquifer doublets, v. 68, p. 54-66.
Wong, T. E., Batjes, D. A., and de Jager, J., 2007, Geology of the Netherlands, Edita-the Publishing House of the Royal.
Zang, A., Oye, V., Jousset, P., Deichmann, N., Gritto, R., McGarr, A., Majer, E., and Bruhn, D. J. G., 2014, Analysis of induced seismicity in geothermal reservoirs–An overview, v. 52, p. 6-21.
Ziegler, P., and Dèzes, P. J. G. S., London, Memoirs, 2006, Crustal evolution of western and central Europe, v. 32, no. 1, p. 43-56.
Ziegler, P. J. G. R., 1982, Triassic rifts and facies patterns in Western and Central Europe, v. 71, no. 3, p. 747-772.
Zoback, M., Barton, C., Brudy, M., Castillo, D., Finkbeiner, T., Grollimund, B., Moos, D., Peska, P., Ward, C., Wiprut, D. J. I. J. o. R. M., and Sciences, M., 2003, Determination of stress orientation and magnitude in deep wells, v. 40, no. 7-8, p. 1049-1076.
Zoback, M. D., 2010, Reservoir geomechanics, Cambridge University Press.
Zoback, M. D., and Gorelick, S. M. J. P. o. t. N. A. o. S., 2012, Earthquake triggering and large-scale geologic storage of carbon dioxide, v. 109, no. 26, p. 10164-10168.
Zoback, M. D., Moos, D., Mastin, L., and Anderson, R. N. J. J. o. G. R. S. E., 1985, Well bore breakouts and in situ stress, v. 90, no. B7, p. 5523-5530.

This page is left blank intentionally

Appendices

Appendix A: Wells data

Table 14. Information about wells data

Well	DT	RHOB	Sonic	Well Markers	Deepest formation	Age
LIR-45	Yes	Yes	No	Yes	Maurits Fm	Triassic
LIR-43	No	Yes	Yes	Yes	Vlieland Fm	Jurassic
HON-GT-01	Yes	Yes	No	Yes	Rodenrijs Cly Fm	Jurassic
HON-GT-02	No	No	No	Yes	Albasserdam Mmbr	Jurassic
LIR-14	No	No	No	Yes	De Lier Mmbr	Jurassic
LIR-32	No	No	No	Yes	Vlieland Fm	Jurassic
LIR-15	No	No	No	Yes	De Lier Mmbr	Jurassic
LIR-31	No	No	No	Yes	Vlieland Fm	Jurassic
LIR-33	No	No	No	Yes	Vlieland Fm	Jurassic
LIR-04	No	No	No	Yes	Vlieland Fm	Jurassic
LIR-13	No	No	No	Yes	Vlieland Fm	Jurassic
LIR-07	No	No	No	Yes	Vlieland Fm	Jurassic
LIR-08	No	No	No	Yes	Vlieland Fm	Jurassic
LIR-47	No	No	No	Yes	Vlieland Fm	Jurassic
LIR-16	No	No	No	Yes	Vlieland Fm	Jurassic
LIR-38	No	No	No	Yes	Vlieland Fm	Jurassic
LIR-35	No	No	No	Yes	Vlieland Fm	Jurassic
LIR-37	No	No	No	Yes	Vlieland Fm	Jurassic
LIR-17	No	No	No	Yes	Vlieland Fm	Jurassic
LIR-09	No	No	No	Yes	Vlieland Fm	Jurassic
LIR-28	No	No	No	Yes	Vlieland Fm	Jurassic
LIR-27	No	No	No	Yes	Vlieland Fm	Jurassic
LIR-25	No	No	No	Yes	Vlieland Fm	Jurassic
LIR-26	No	No	No	Yes	Ommenlanden Fm	Cretaceous
LIR-20	No	No	No	Yes	Vlieland Fm	Jurassic
LIR-44	No	No	No	Yes	Eemhaven Mmbr	Jurassic
LIR-34	No	No	No	Yes	Vlieland Fm	Jurassic
NLW-GT-01	Yes	Yes	Yes	Yes	Rogenstein Mmbr	Triassic

Table 15. The interval velocity calculation

Interval 1 Mean Sea Level to Top Cretaceous (Ommeladen)

wellname	TWT top interval	TWT base interval	TVD top interval	TVD base interval	Delta TWT	Delta TVDepth	Calculated Vint	Calculated Thickness	Difference in thickness	Calculated TVDepth	Difference in TVDepth
	[s]	[s]	[m]	[m]	[s]	[m]	[m/s]	[m]	[m]	[m]	[m]
Lir 45	0.0000	0.8496	-0.004	-733.330	0.850	733.3260	1726.4	735.923	2.6	735.9	2.6
Lir 43	0.0000	0.8660	-0.004	-753.170	0.866	753.1660	1739.3	750.207	-3.0	750.2	-3.0
						Final choice Vint	1732.5				

Interval 2 Top Jurassic (Upper Werkendam Member) 1732.85998

wellname	TWT top interval	TWT base interval	TVD top interval	TVD base interval	Delta TWT	Delta TVDepth	Calculated Vint	Calculated Thickness	Difference in thickness	Calculated TVDepth	Difference in TVDepth
	[s]	[s]	[m]	[m]	[s]	[m]	[m/s]	[m]	[m]	[m]	[m]
Lir 45	0.8496	1.8918	-733.33	-2423.48	1.0	1690.2	3243.3	1689.5	-0.7	2425.4	1.9
						Final choice Vint	3242.0				

Interval 3 ber) to Top Triassic (Dolomitic Keuper Member)

wellname	TWT top interval	TWT base interval	TVD top interval	TVD base interval	Delta TWT	Delta TVDepth	Calculated Vint	Calculated Thickness	Difference in thickness	Calculated TVDepth	Difference in TVDepth
	[s]	[s]	[m]	[m]	[s]	[m]	[m/s]	[m]	[m]	[m]	[m]
Lir 45	1.8918	2.1581	-2423.48	-2882.96	0.3	459.5	3450.5	459.4	-0.1	2884.8	1.9
						Final choice Vint	3450.0				

Interval 4 ember) to Base Triassic (Zeichstein Group)

wellname	TWT top interval	TWT base interval	TVD top interval	TVD base interval	Delta TWT	Delta TVDepth	Calculated Vint	Calculated Thickness	Difference in thickness	Calculated TVDepth	Difference in TVDepth
	[s]	[s]	[m]	[m]	[s]	[m]	[m/s]	[m]	[m]	[m]	[m]
Lir 45	2.1581	2.3643	-2882.96	-3372.03	0.206	489.1	4743.9	488.9	-0.2	3373.7	1.7
						Final choice Vint	4742.0				

Vertical resolution is derived from the seismic sections at the well locations and the interval velocities. The resolution is calculated by counting the number of cycles, that is peak to peak or trough to trough (Figure 62) in a particular window (2350 ms is used here), then converting the cycle observed to meters using the interval velocity using equations 15 and 16 (Rafaelsen, 2006). Those equations were used to calculate the wavelength and the resolution (Rayleigh's criterion), respectively. The vertical resolution in the Lower Germanic Triassic Group is around 20.25 ms, which is equal to 24 m.

$$\lambda = \frac{V}{f} \quad (15)$$

$$\text{resolution} = \frac{\lambda}{4} \quad (16)$$

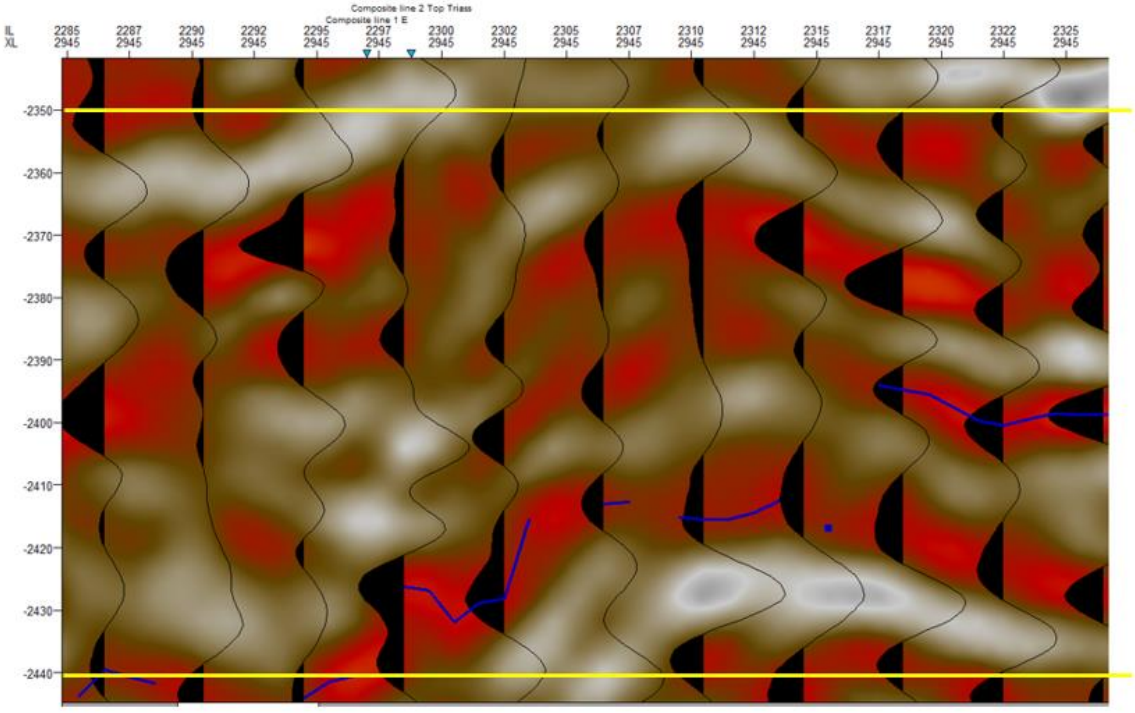

Delta_t between -2350 to -2440 = 90 ms
Wiggles cycle = 4
Vint Triassic = 4742 m/s

$$\frac{90\ x\ 0.9}{4} = 20.25$$

$$\frac{20.25\ x\ 4742}{1000} = 96.02$$

$$\frac{96.02}{4} = 24\ m$$

Figure 62. Vertical accuracy in the Lower Germanic Triassic Group (LGT)

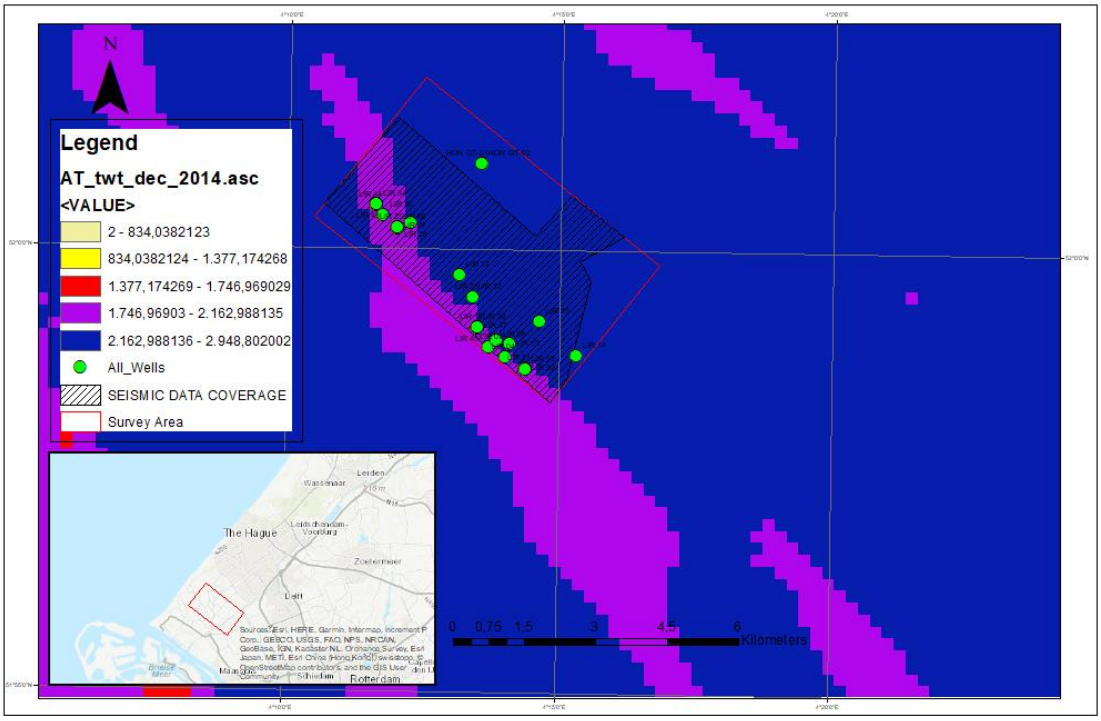

Figure 63. Wells and two-way travel time. Basemap from ESRI, TWT layer from DGM-NLOG

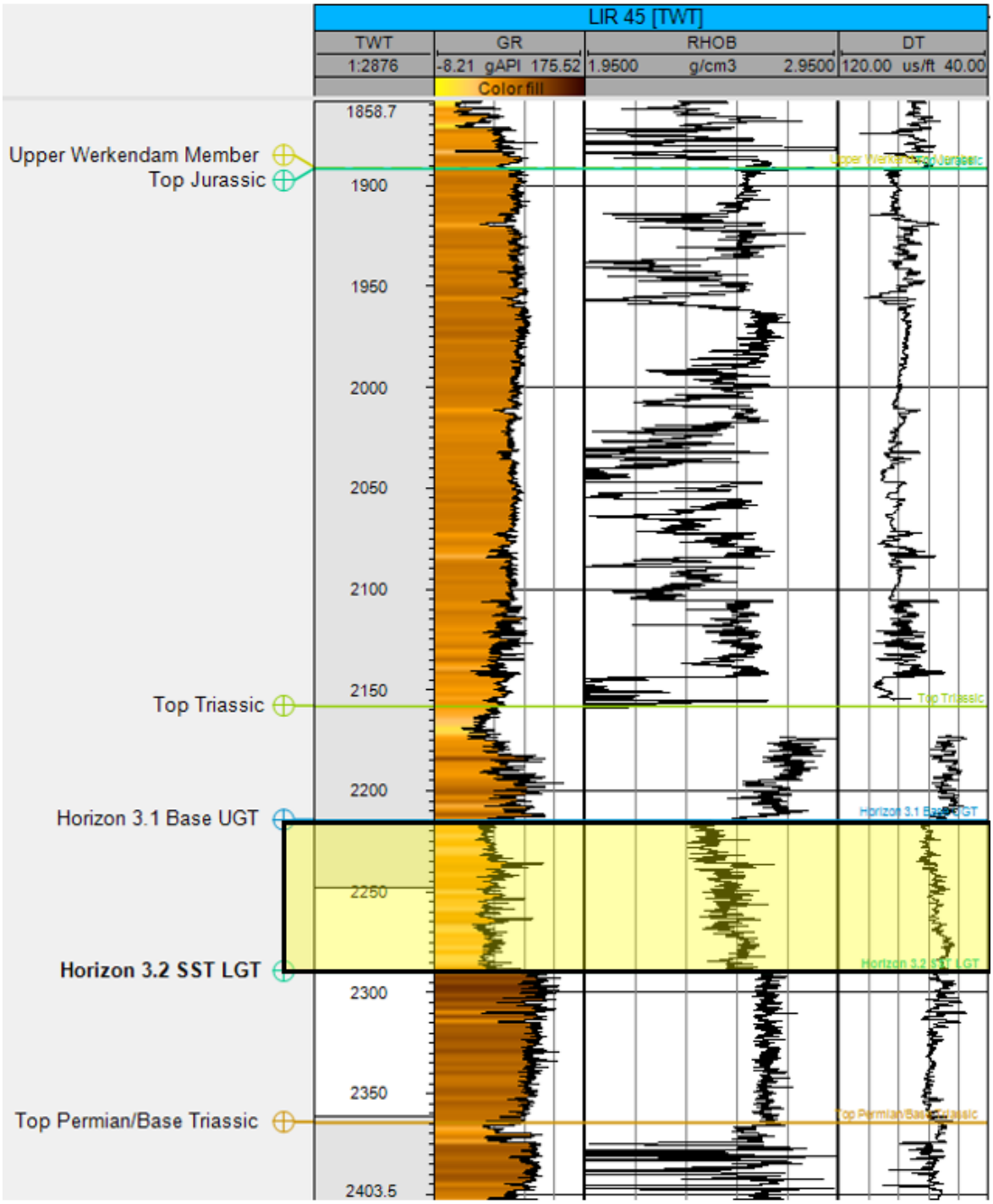

Figure 64. Well markers and two-way travel time value in base (LGT)

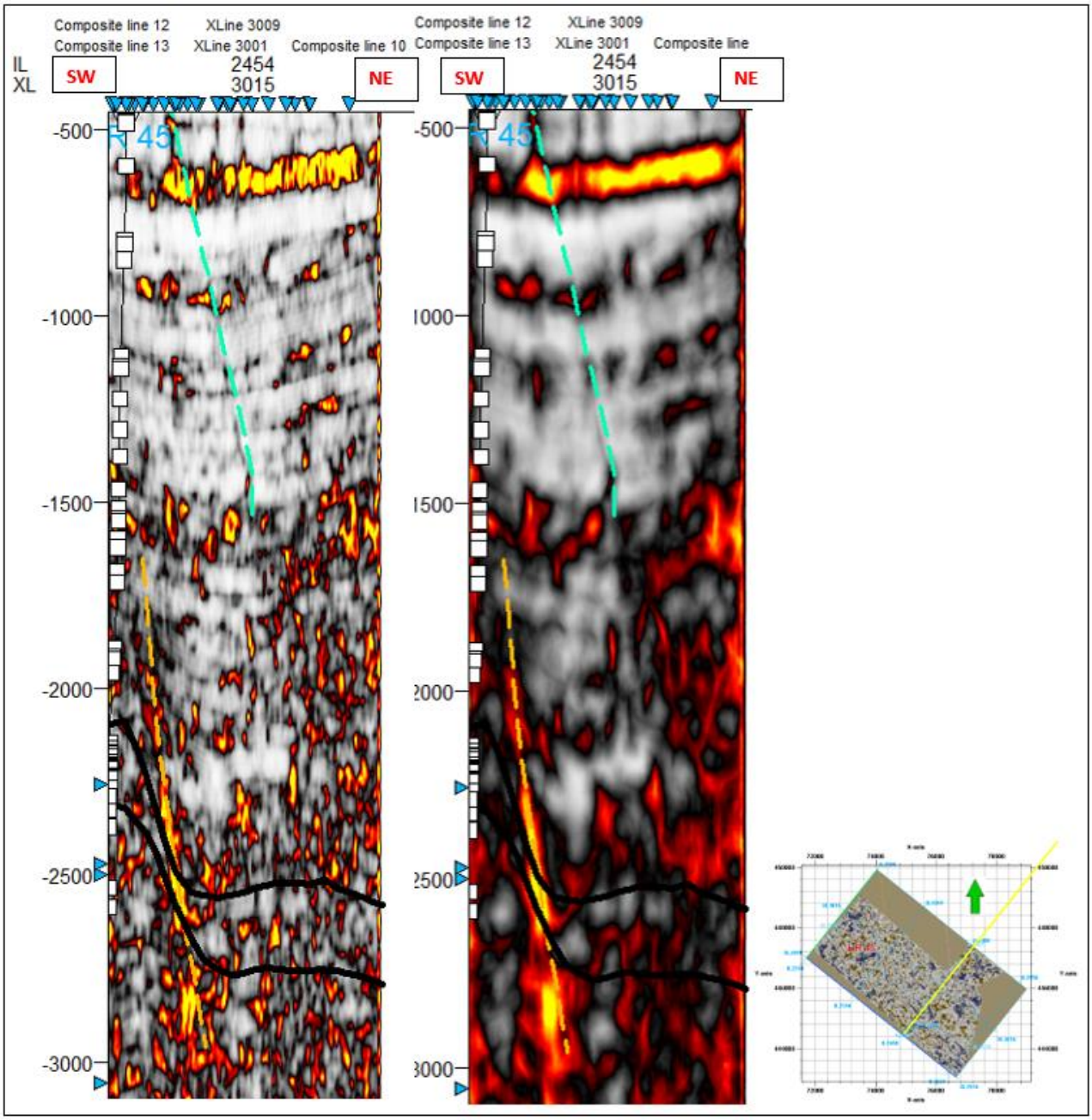

Figure 65. Variance attributes for fault interpretation. The light color indicates faults presence

Figure 65 shows the variance attributes used as guidance while making fault interpretation. The variance represents the trace-to-trace variability over a particular sample interval and therefore produces interpretable lateral changes in acoustic impedance. Discontinuity features, such as faults, produce a high variance coefficient, therefore, make it detectable in 3D seismic volumes.

Figure 66 and Figure 67 show the example of the Digital Geological Model (DGM v4) from the subsurface of the Netherlands. The DGM was composed of seismic interpretations using publicly available 2D and 3D seismic survey data. However, the purpose of the DGM model is to provide a regional geological understanding. Thus, the model should not be consulted for reservoir scale issues. The use of DGM in this project was only for guidance while making horizon interpretations.

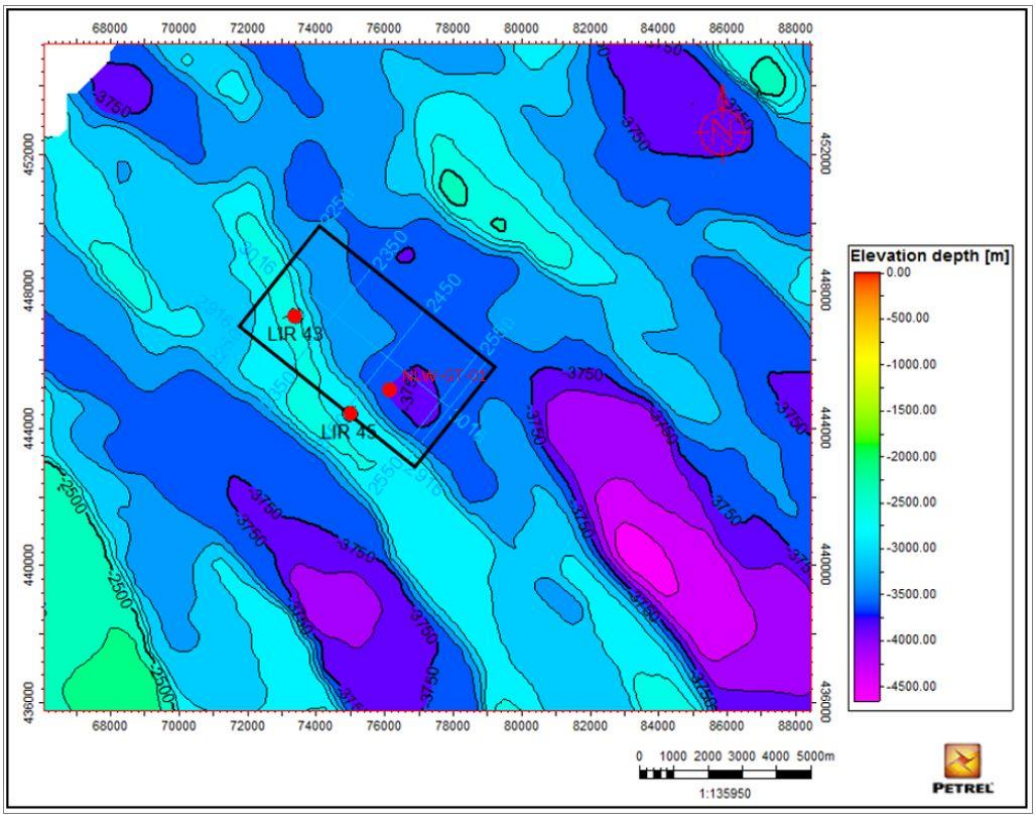

Figure 66. Depth map of top-Lower Germanic Triassic group. Model is taken from Digital Geological Model v4 onshore

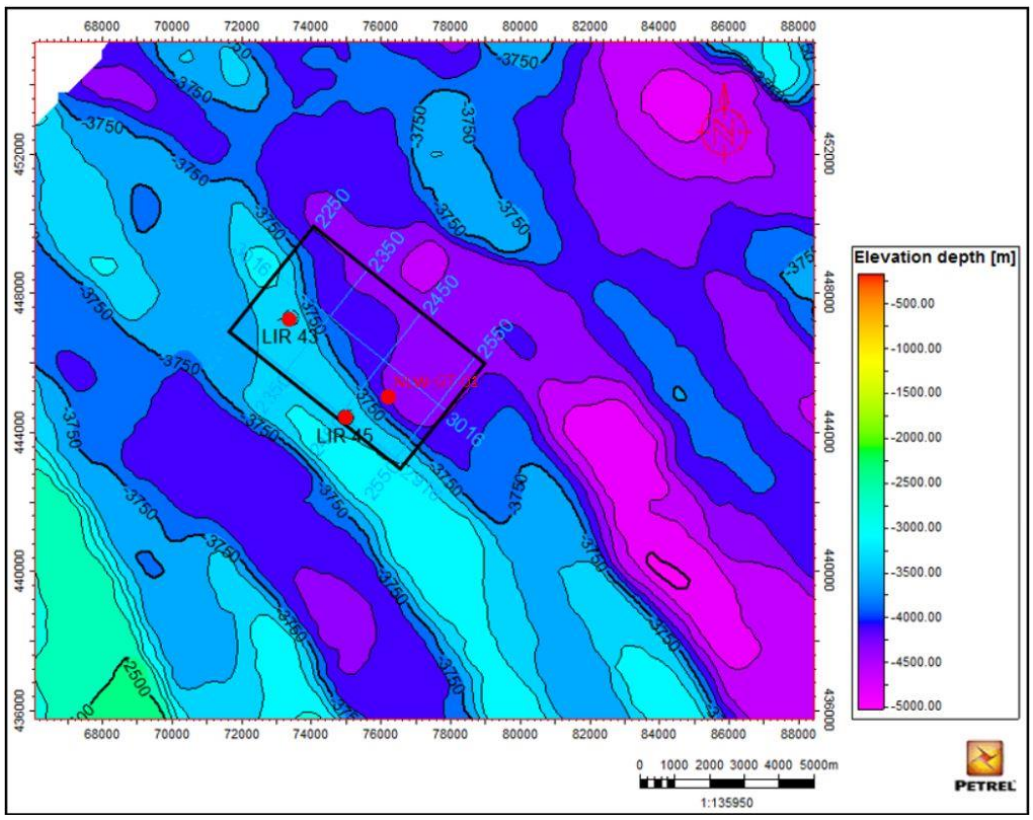

Figure 67. Depth map of base-Lower Germanic Triassic group. Model is taken from Digital Geological Model v4 onshore

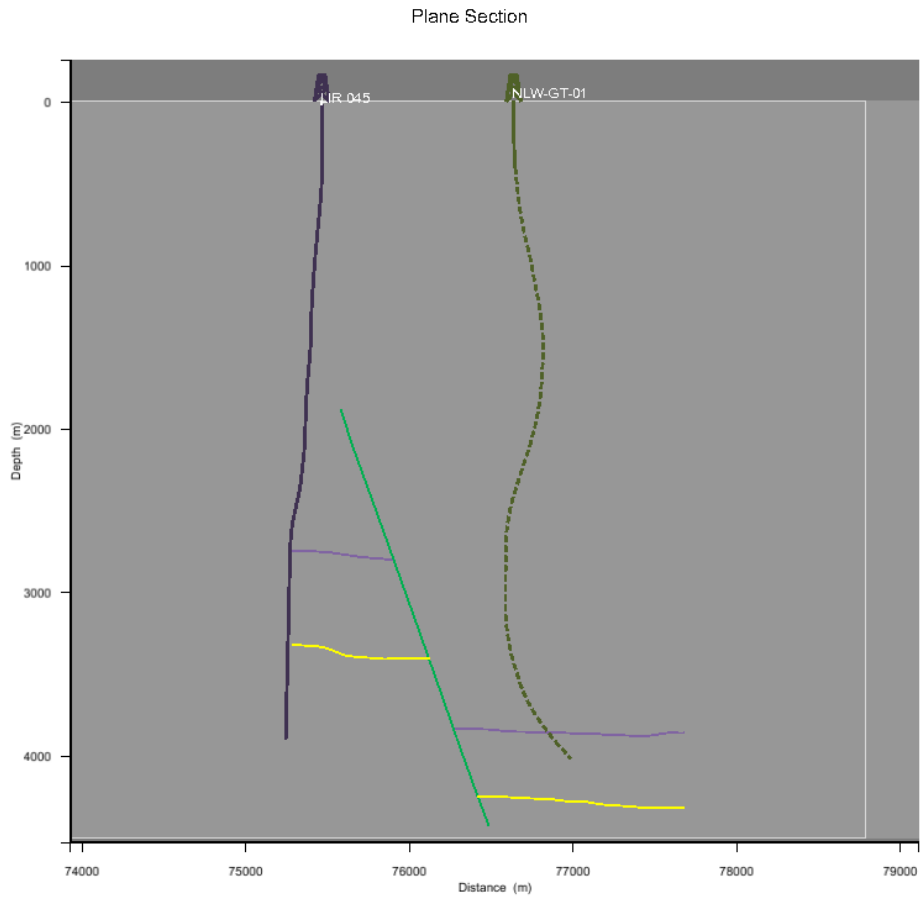

Figure 68. Cross-section view-the Lower Germanic Triassic group

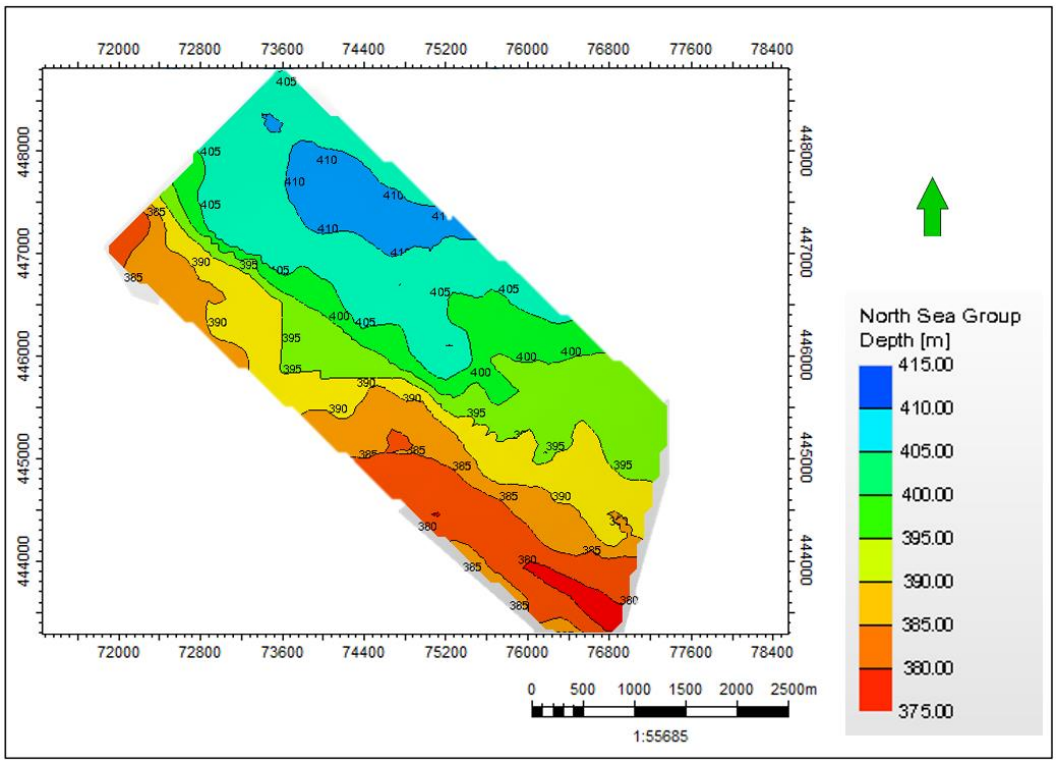

Figure 69. The depth map of base Upper North Sea group (NU)

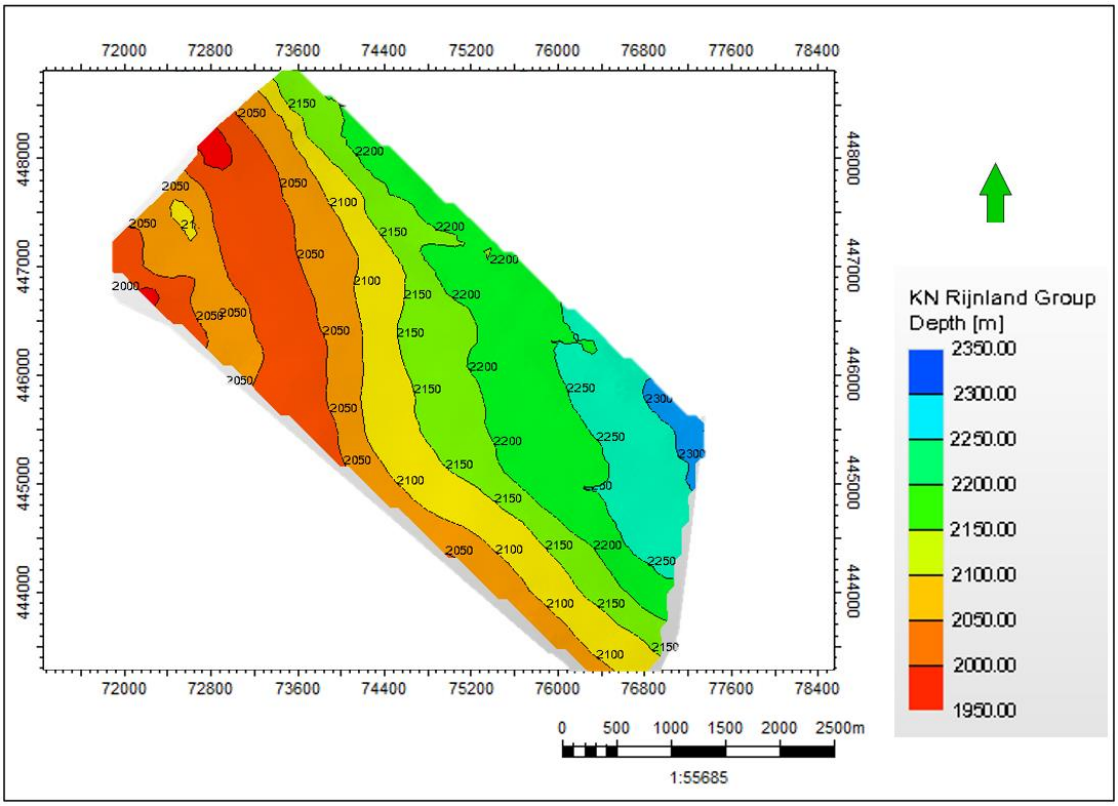

Figure 70. The depth map of base Rijnland group (KN)

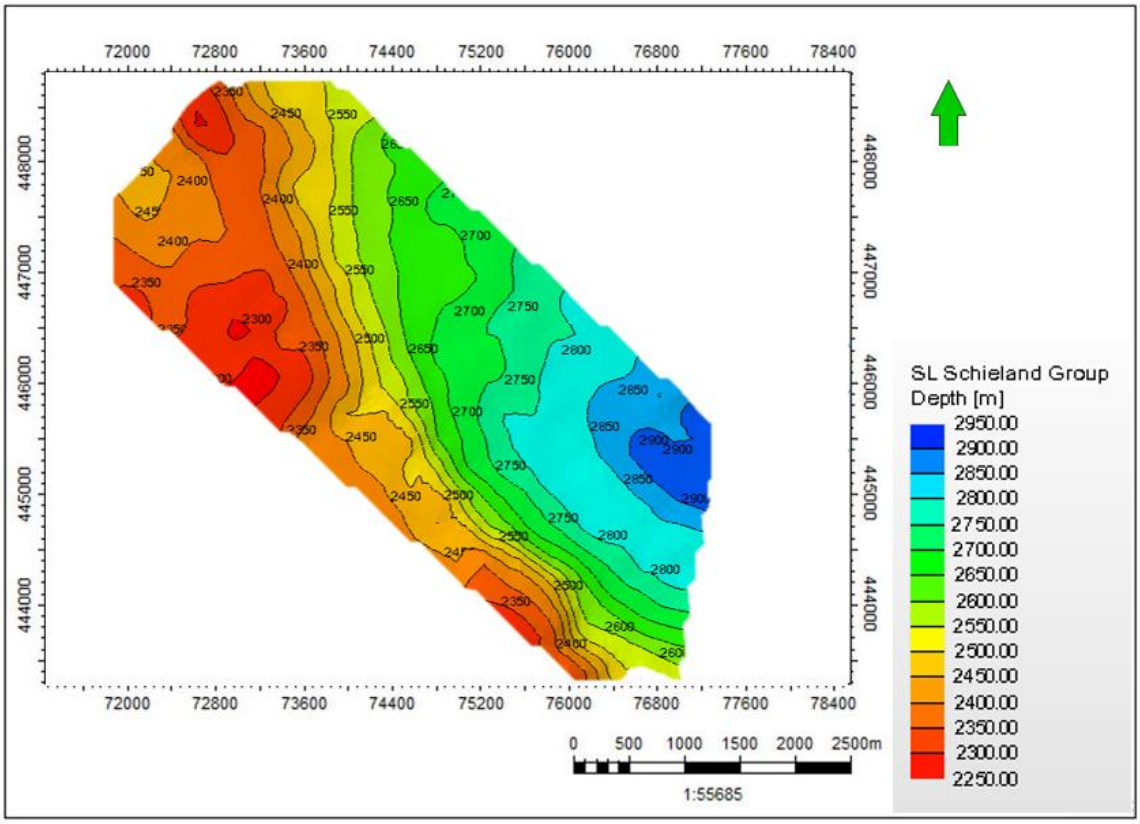

Figure 71. The depth map of base Schieland group (SL)

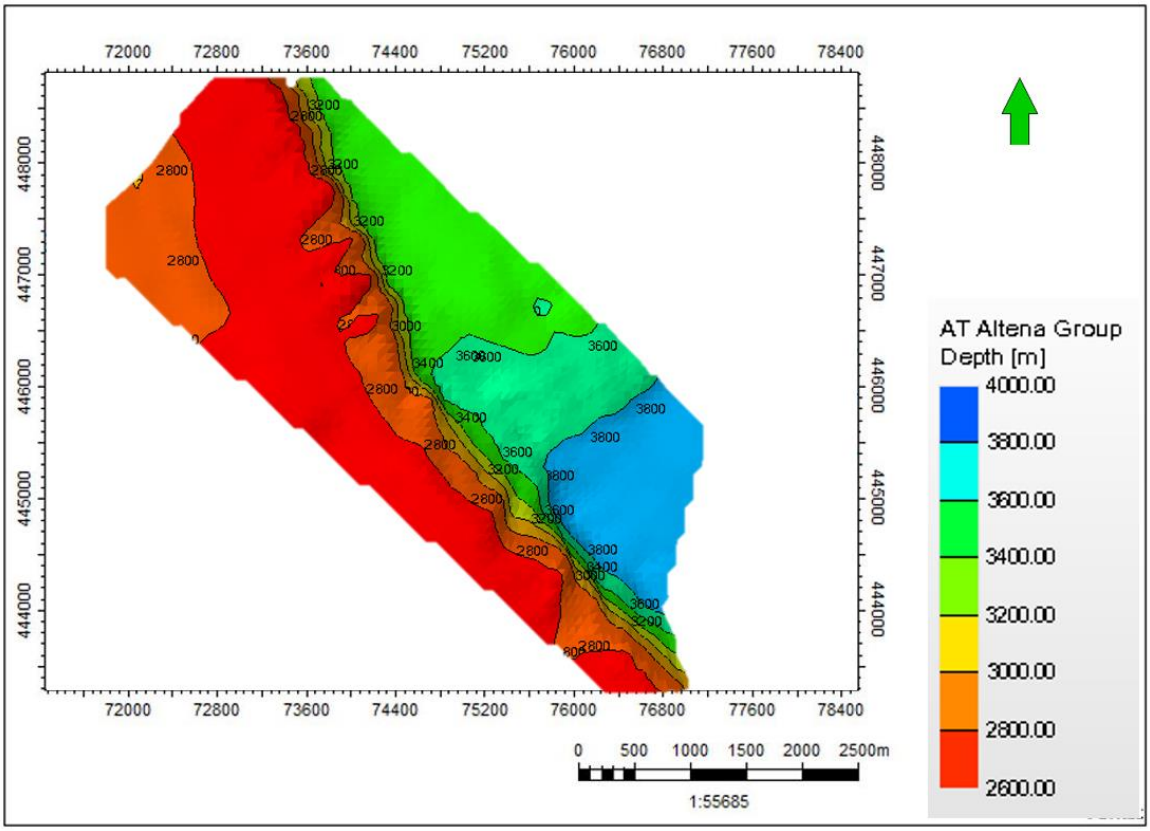

Figure 72. The depth map of base Altena group (AT)

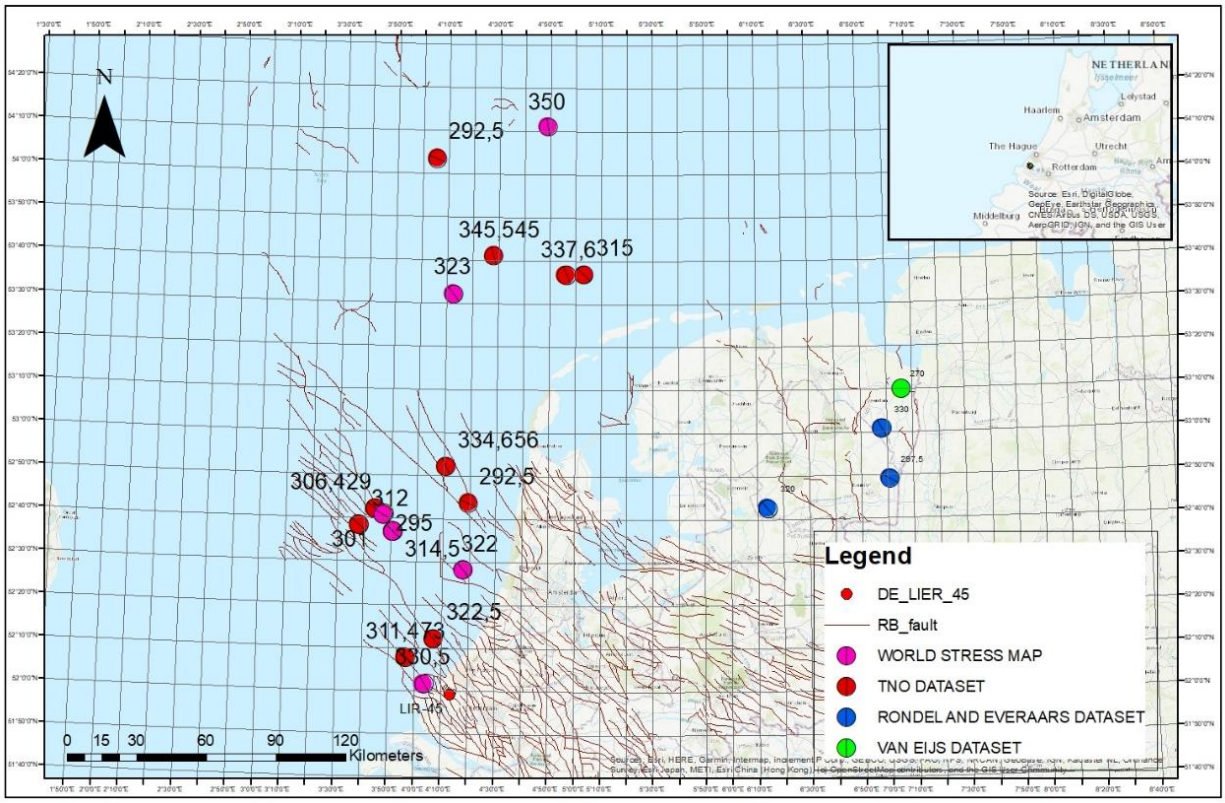

Figure 73. Stress map showing SHMax direction in the Lower Germanic Triassic group

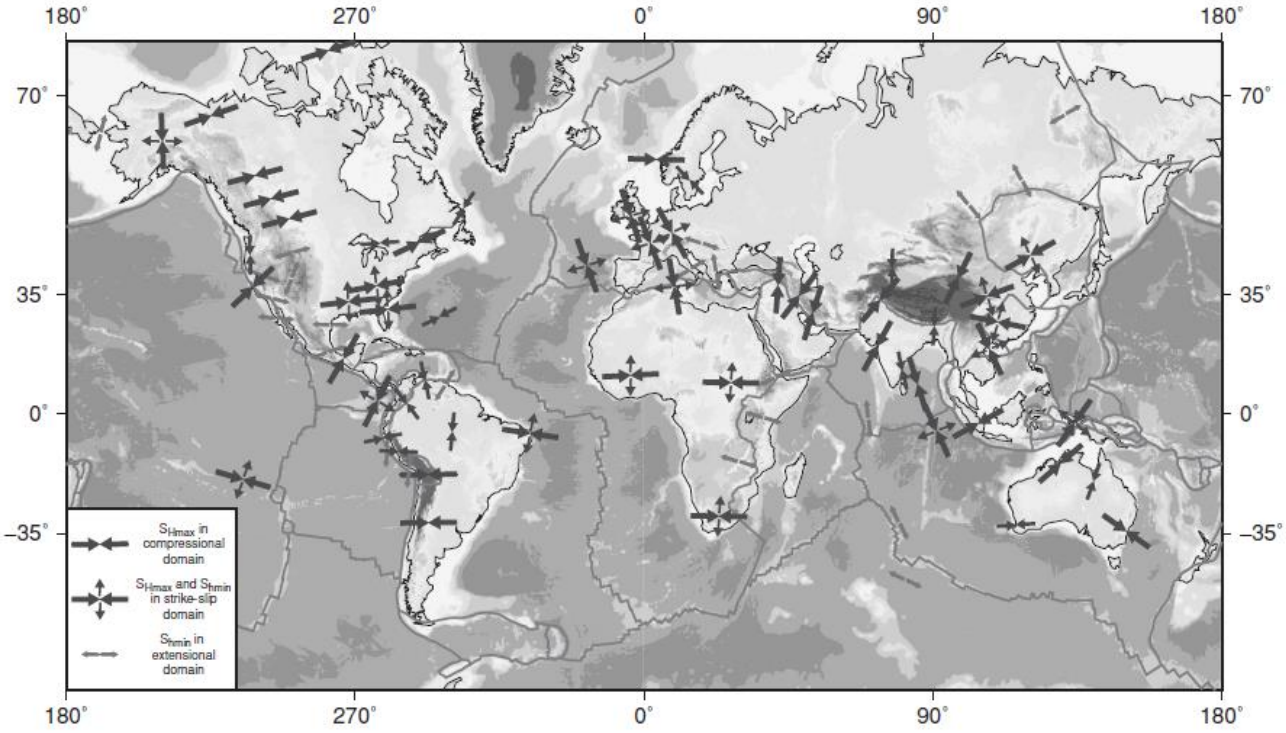

Figure 74. World stress map (Zoback, 2010)

Appendix D: 1D Geomechanical modeling

The following figures show the result of 1D geomechanical modeling in well LIR-43. Despite the fact that this well does not intersect with the Triassic formation, but the trend of the stress regime is similar to well LIR-45. Well LIR-43 was used during horizon interpretation as guidance for shallower formation.

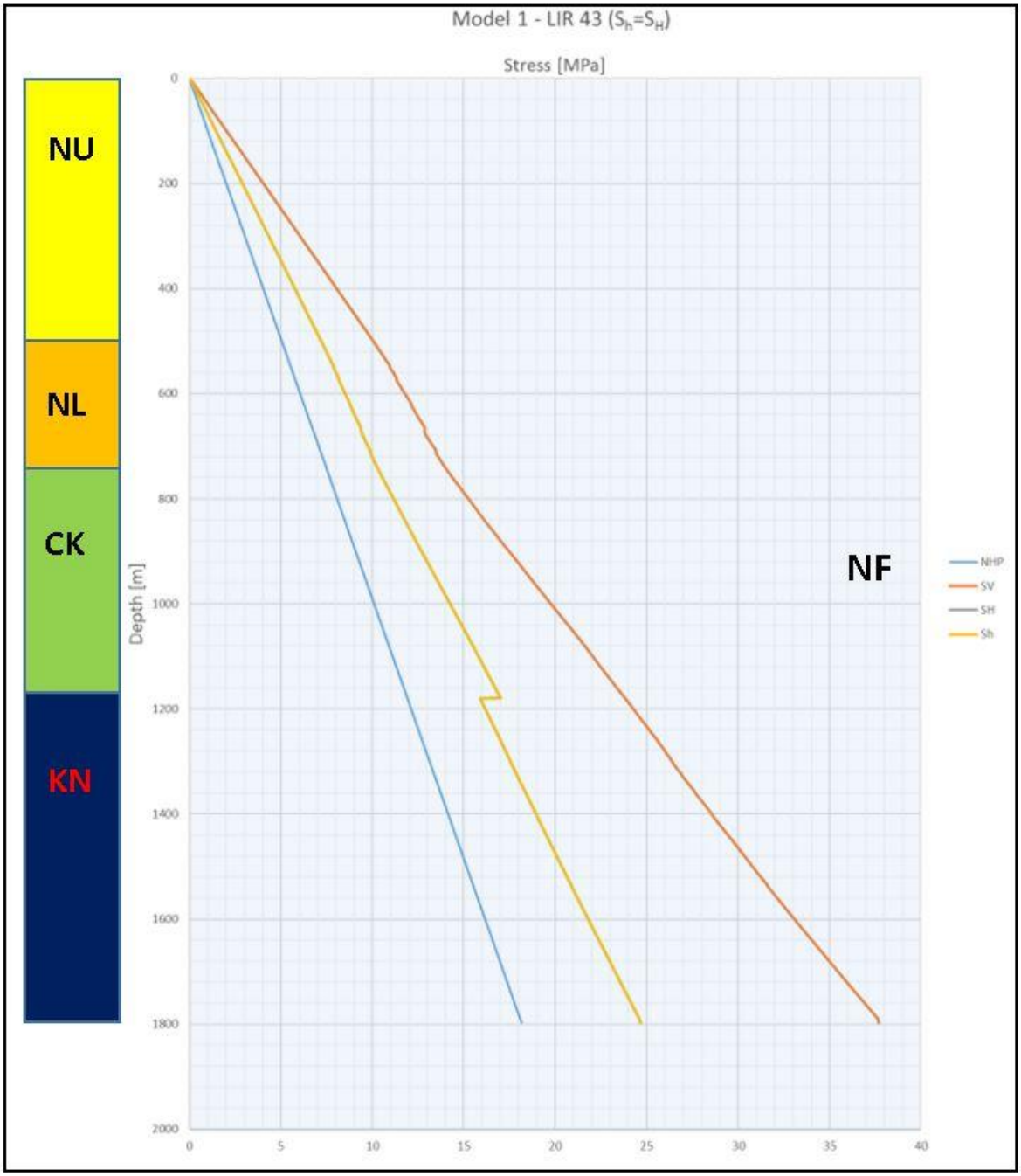

Figure 75. Stress profile against depth; NU=Upper North Sea group;NL=Lower North Sea group; CK=Chalk group;KN=Rijnland group;SL=Schieland group;AT=Altena group;RB=Lower Germanic Triassic group

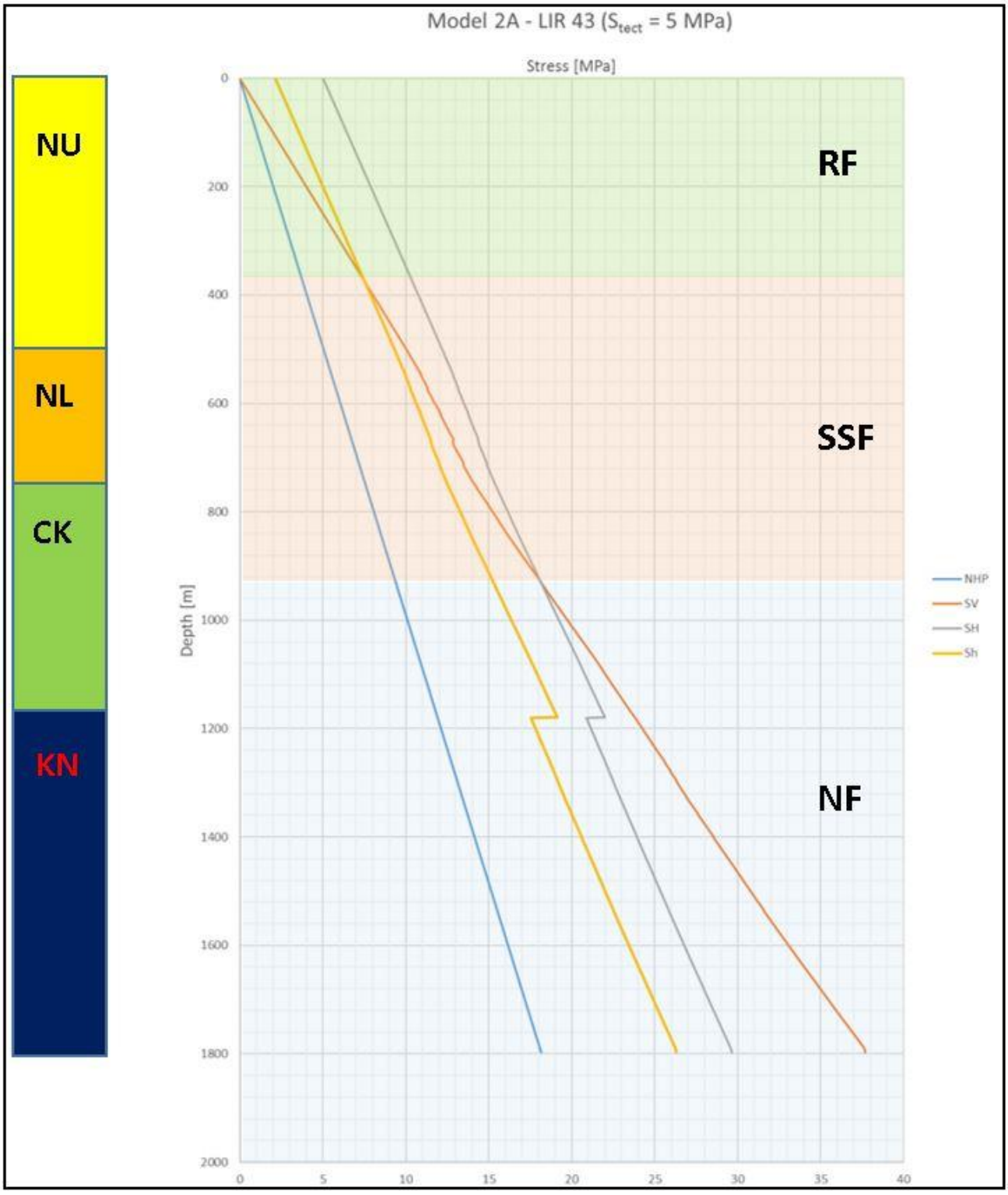

Figure 76. Stress profile against depth with tectonic stress 5 MPa; NF = Normal Fault SSF = Strike-slip fault; RF = Reverse fault

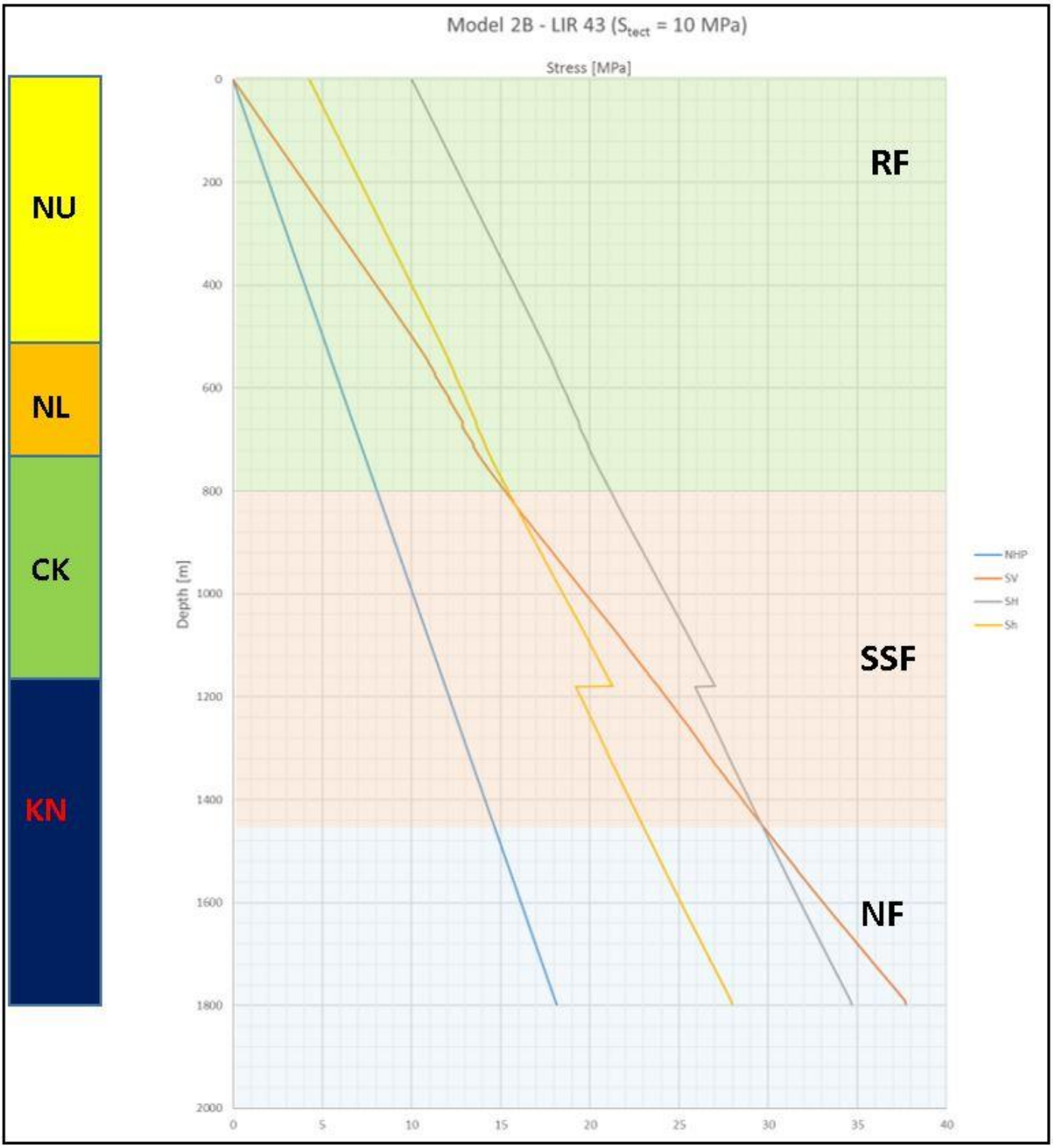

Figure 77. Stress profile against depth with tectonic stress 10 MPa; NF = Normal Fault SSF = Strike-slip fault; RF = Reverse fault

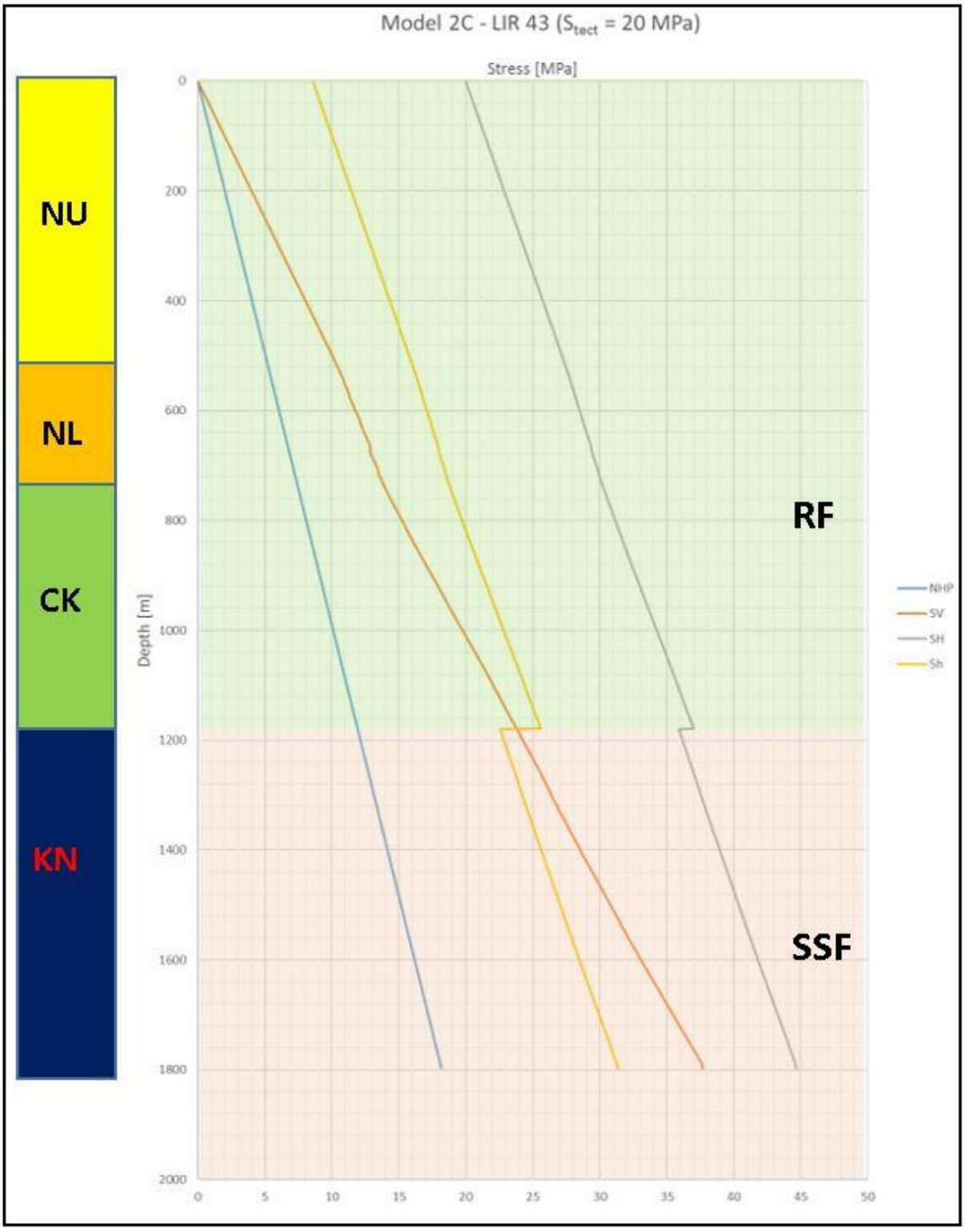

Figure 78. Stress profile against depth with tectonic stress 20 MPa; SSF = Strike-slip fault; RF = Reverse fault

The following figure shows the density data (RHOB) calculated from raw log data, obtained from NLOG. The bulk density was calculated and used as a primary input in the Abaqus simulation. Furthermore, the bulk density was used to calculate ESRmin and ESRmax.

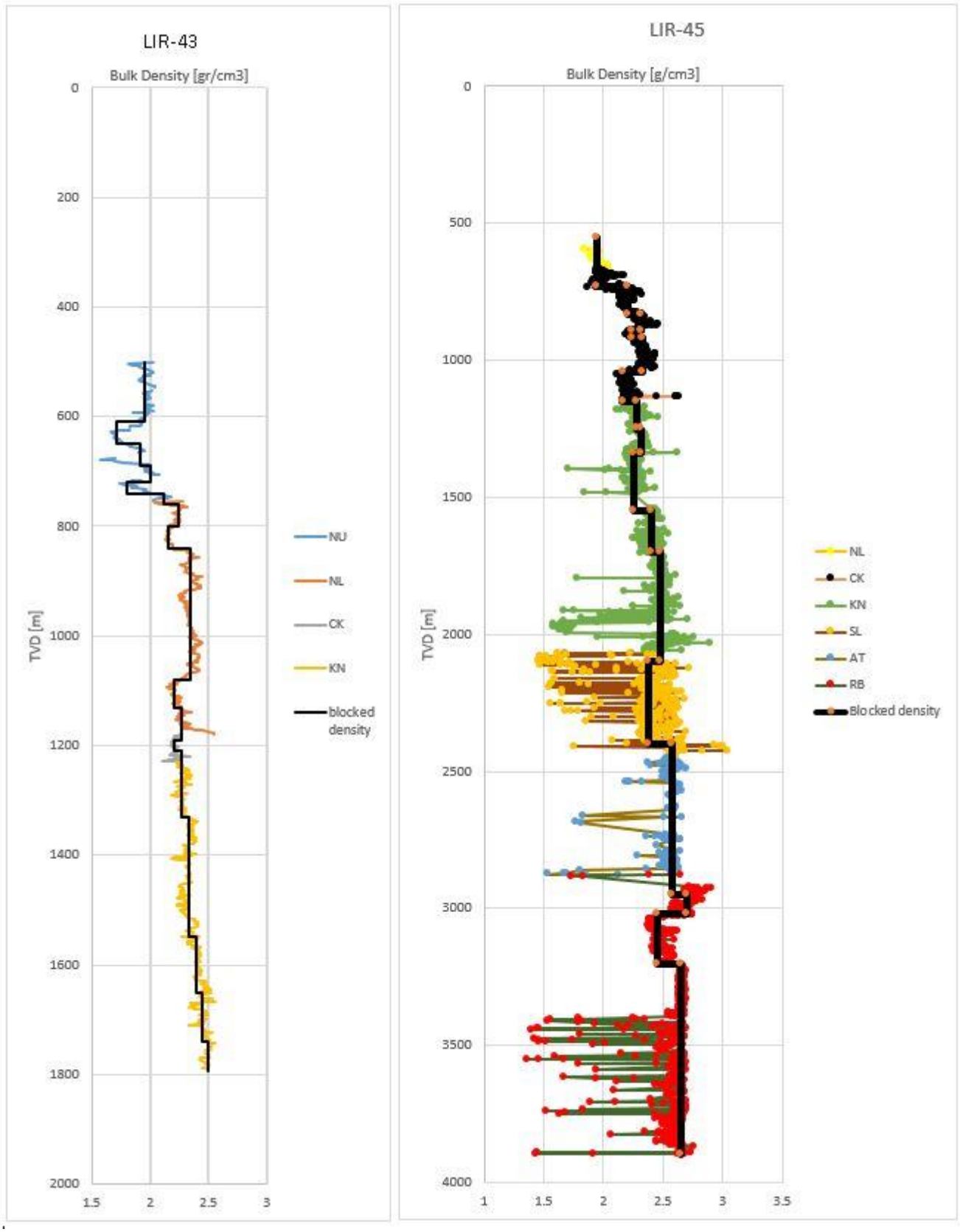

Figure 79. Bulk density Well LIR-43 & LIR 45

The following figure shows the density data (RHOB) of well NLW-GT-01 obtained from NLOG. The density data was available only at depth from -4100 m until - 4340 m. The bulk density was calculated and was used as a primary input in the Abaqus simulation.

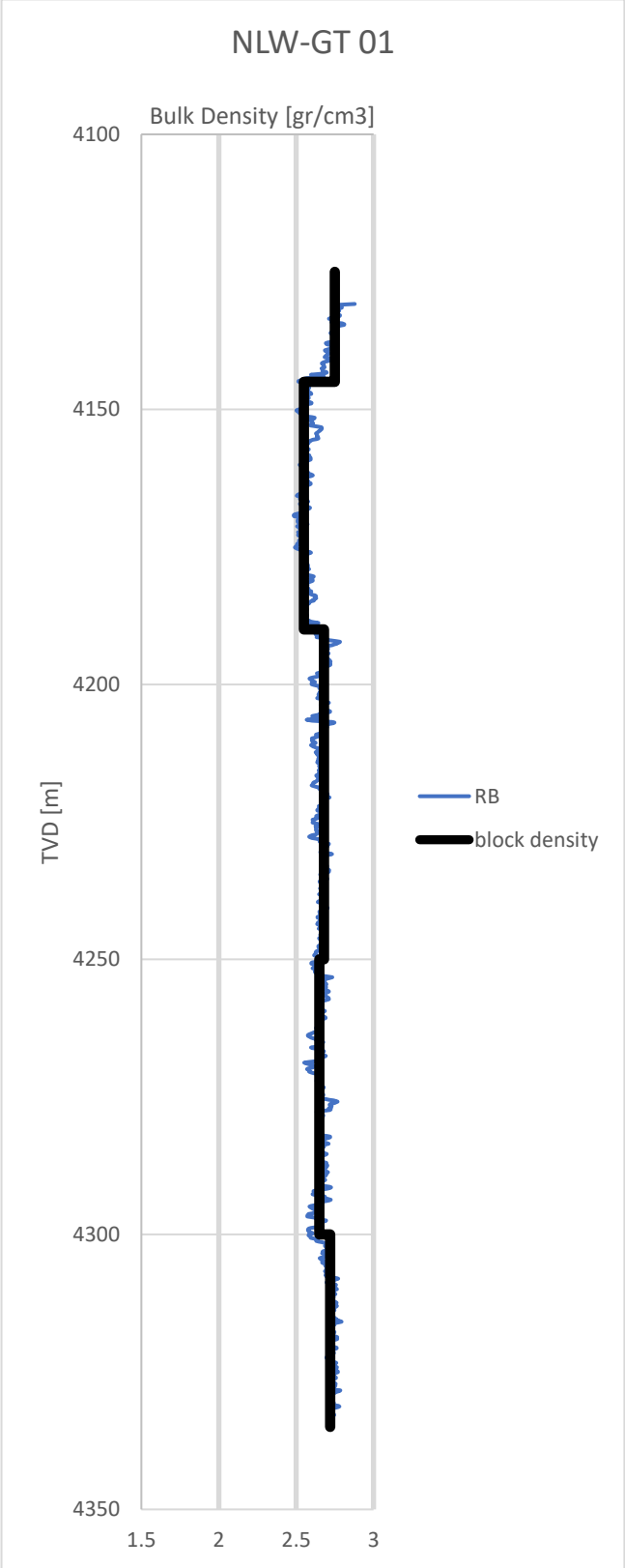

Figure 80. Bulk density Well NLW-GT 01

The following figures show the 1D model of well NLW-GT 01. The Lower Germanic Triassic group at a depth of -4100 m until -4340 exhibits a normal fault regime throughout all models.

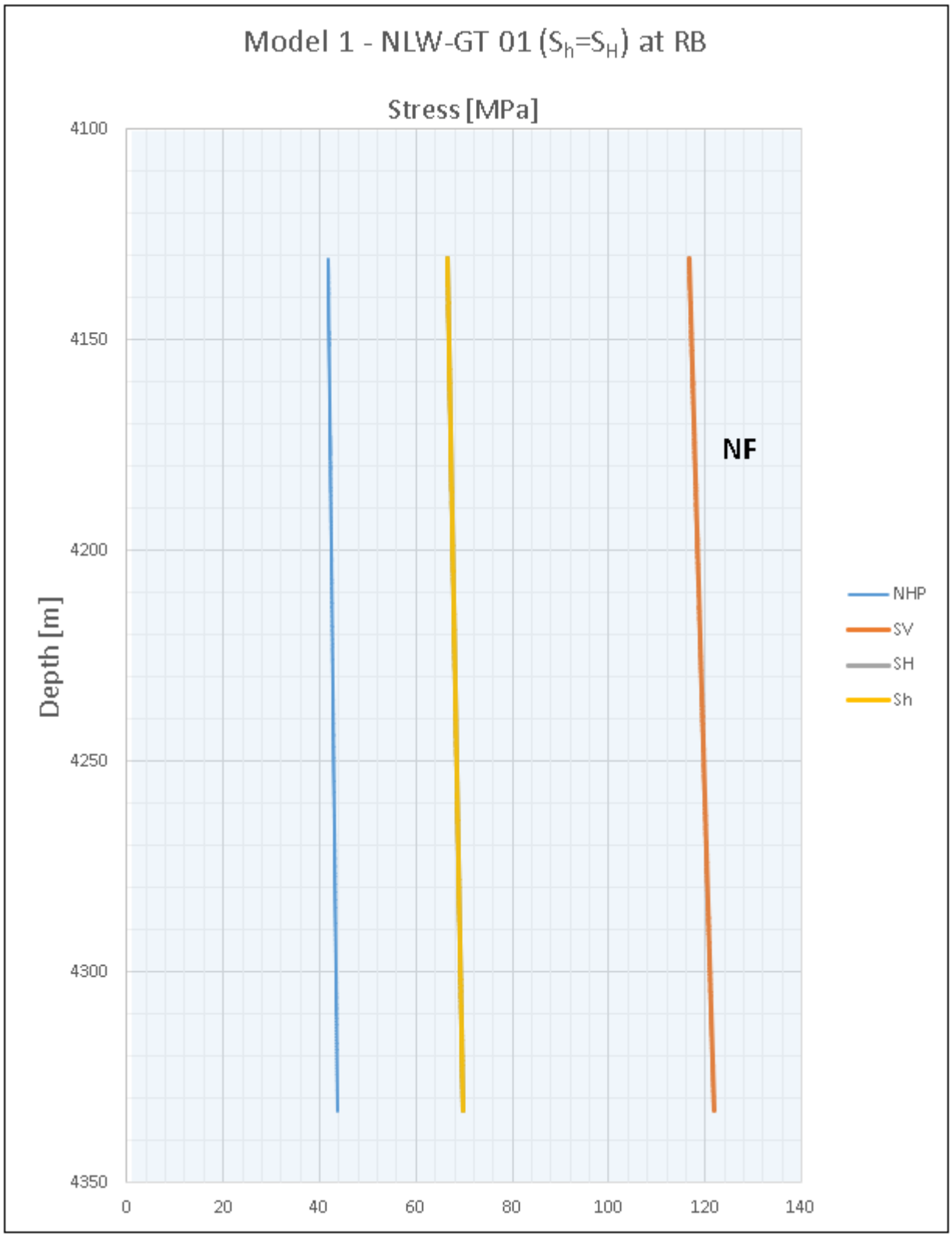

Figure 81. Stress profile against depth; RB = Lower Germanic Triassic group; NF = Normal Fault

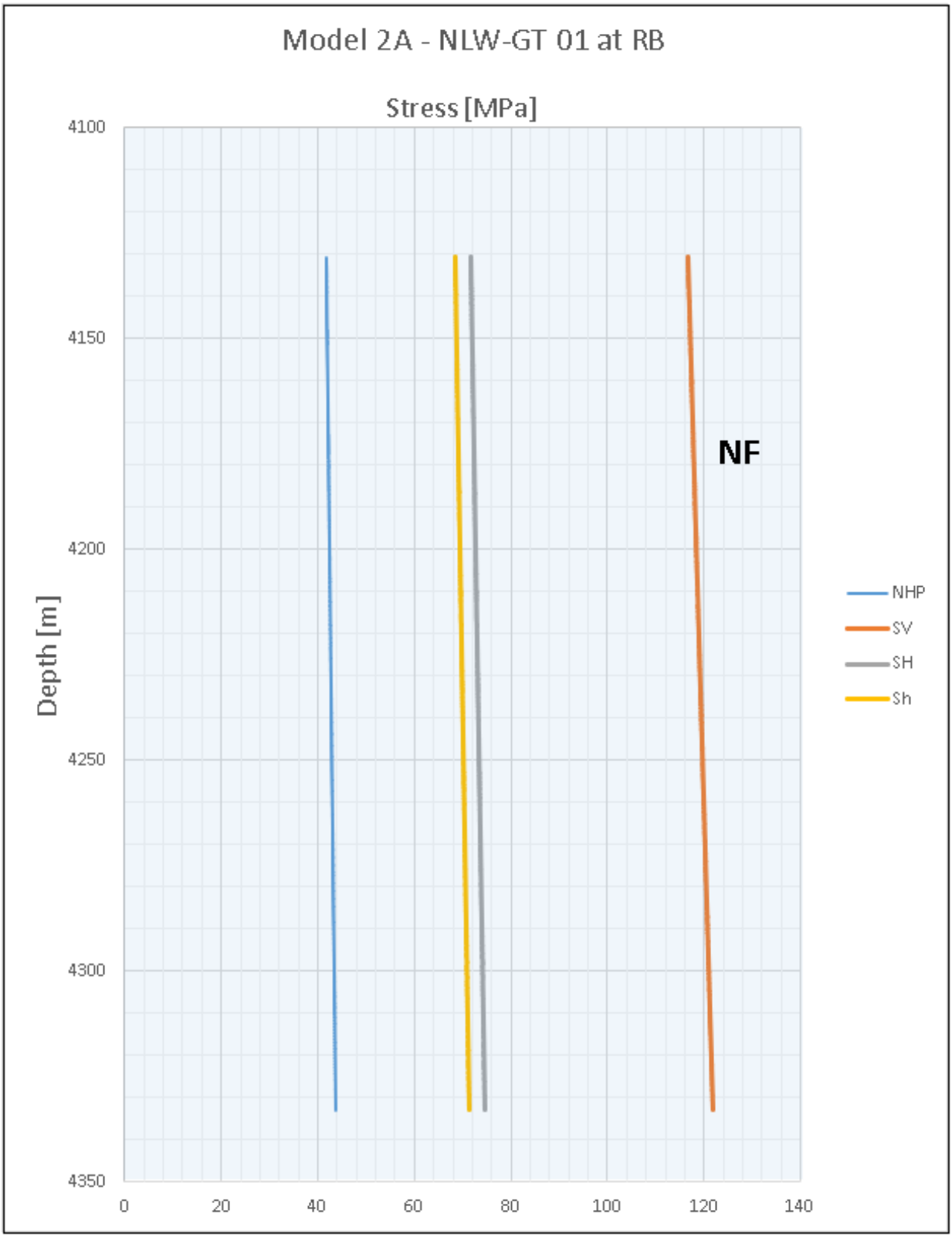

Figure 82. Stress profile against depth with tectonic stress 5 MPa; NF = Normal Fault

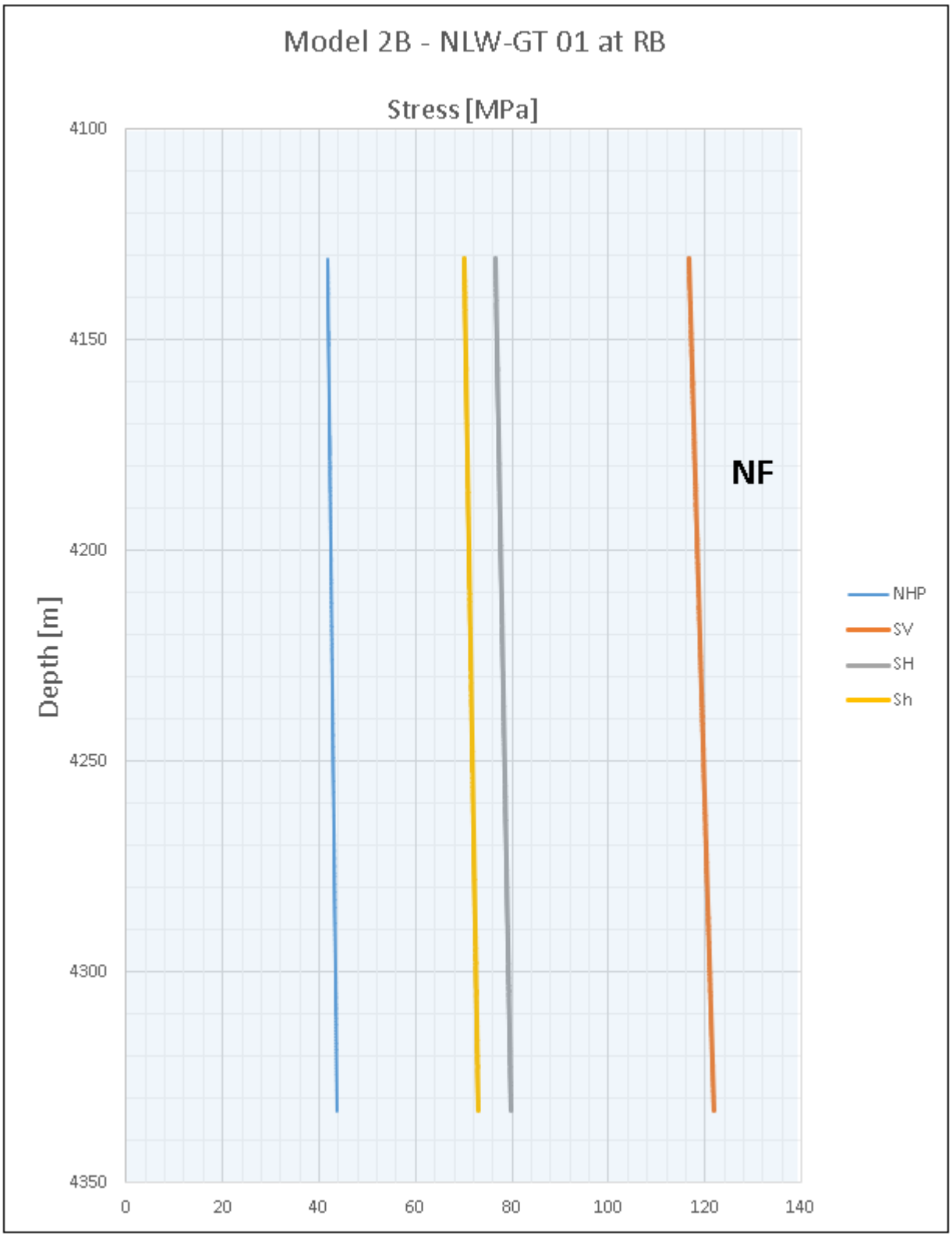

Figure 83. Stress profile against depth with tectonic stress 10 MPa; NF = Normal Fault

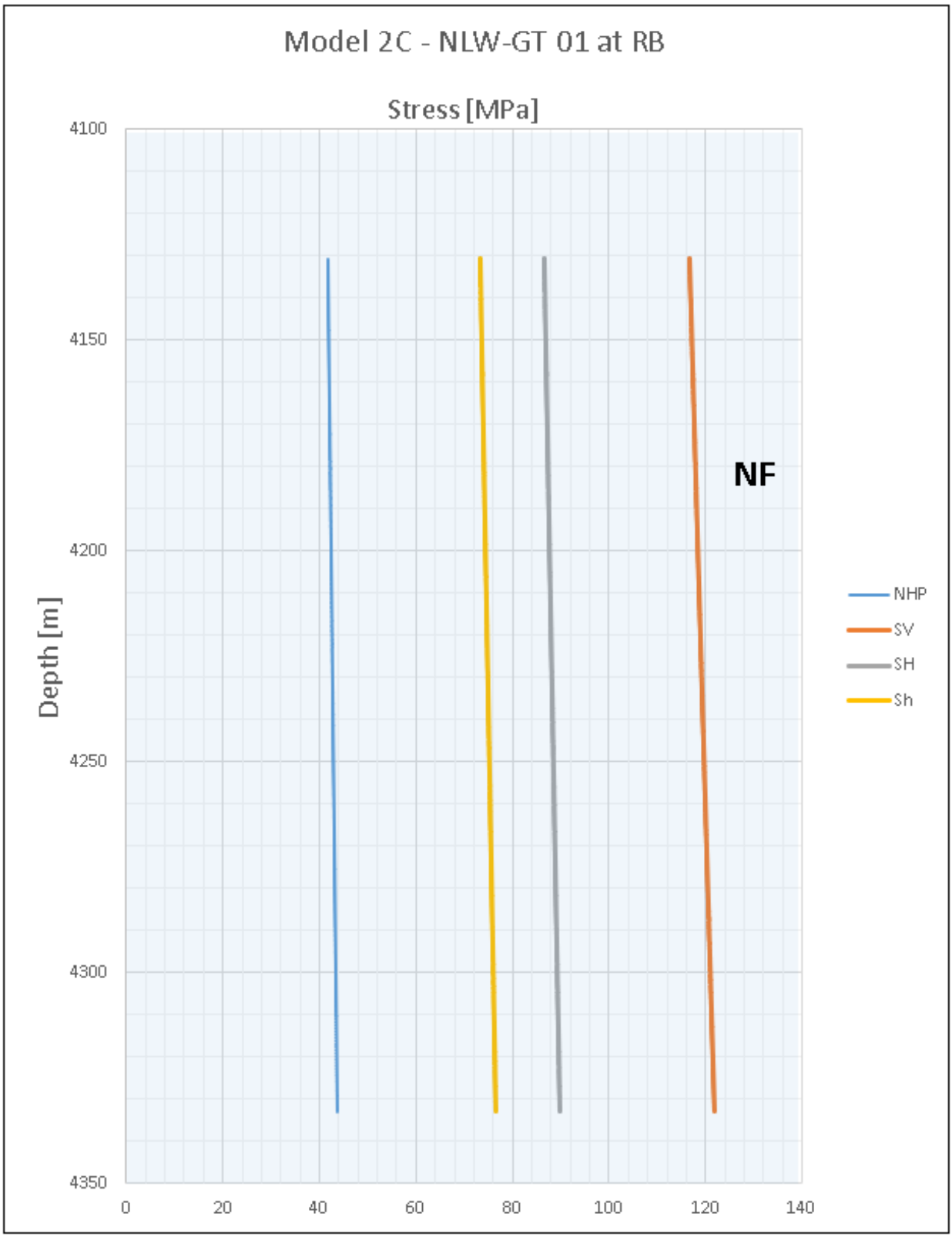

Figure 84. Stress profile against depth with tectonic stress 20 MPa; NF = Normal fault

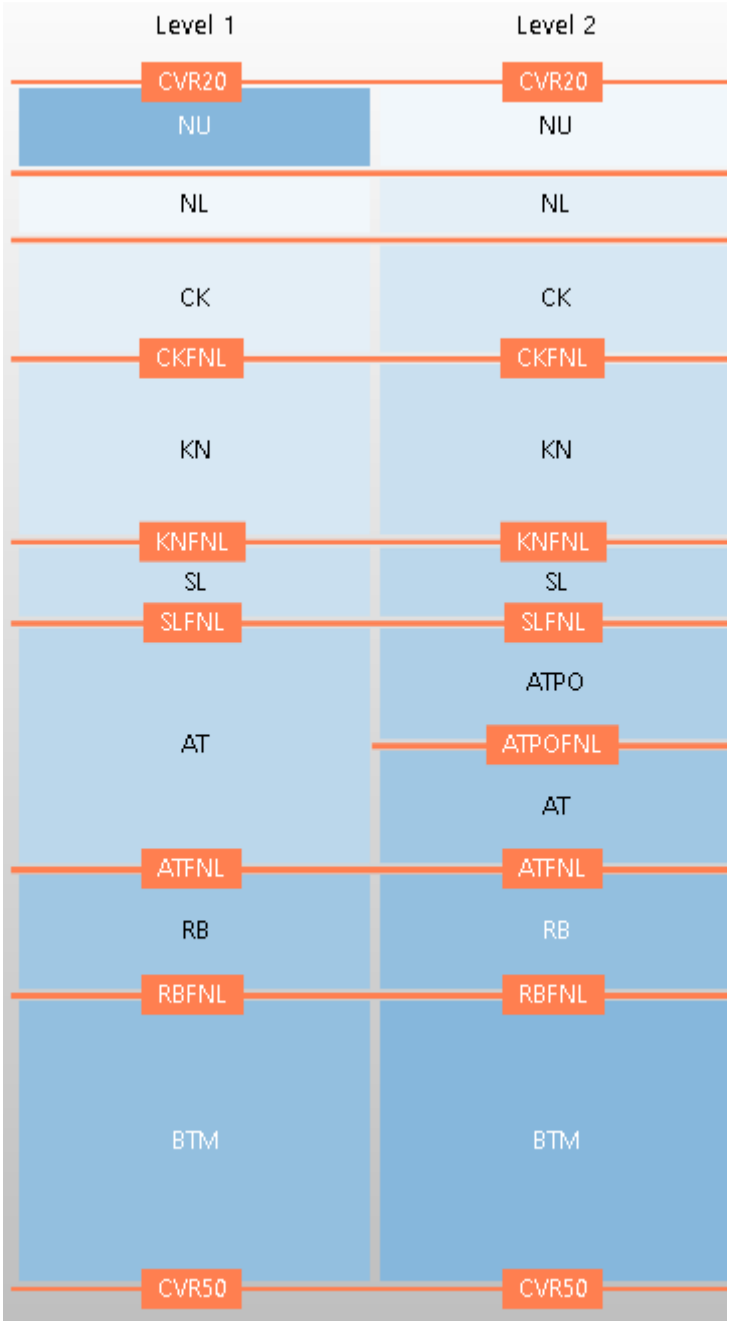

Figure 85. Stratigraphic model

Figure 85 is the stratigraphic model from top to bottom. The sequence of the horizons was following the interpreted horizons from seismic interpretation. NU is the Upper North Sea group; NL is the Lower North Sea group; CK is the Chalk group; KN is the Rijnland group; SL is the Schieland group; AT is the Altena group and RB is the Lower Germanic Triassic group. ATPO is Posidonia Shale formation and is considered part of the Altena group (AT). Therefore, in the stratigraphic model, ATPO lies at Level 2. The horizon of base ATPO is only found at the down-thrown block of the model. No presence of ATPO at the up-thrown block, due to erosion. The rock properties of ATPO were set to be similar to the Altena group (AT).

Figure 86 shows the finite element model and its corresponding material. The depth of the model was extended to -5500 m to prevent the influence of the boundary effects on the finite element modeling.

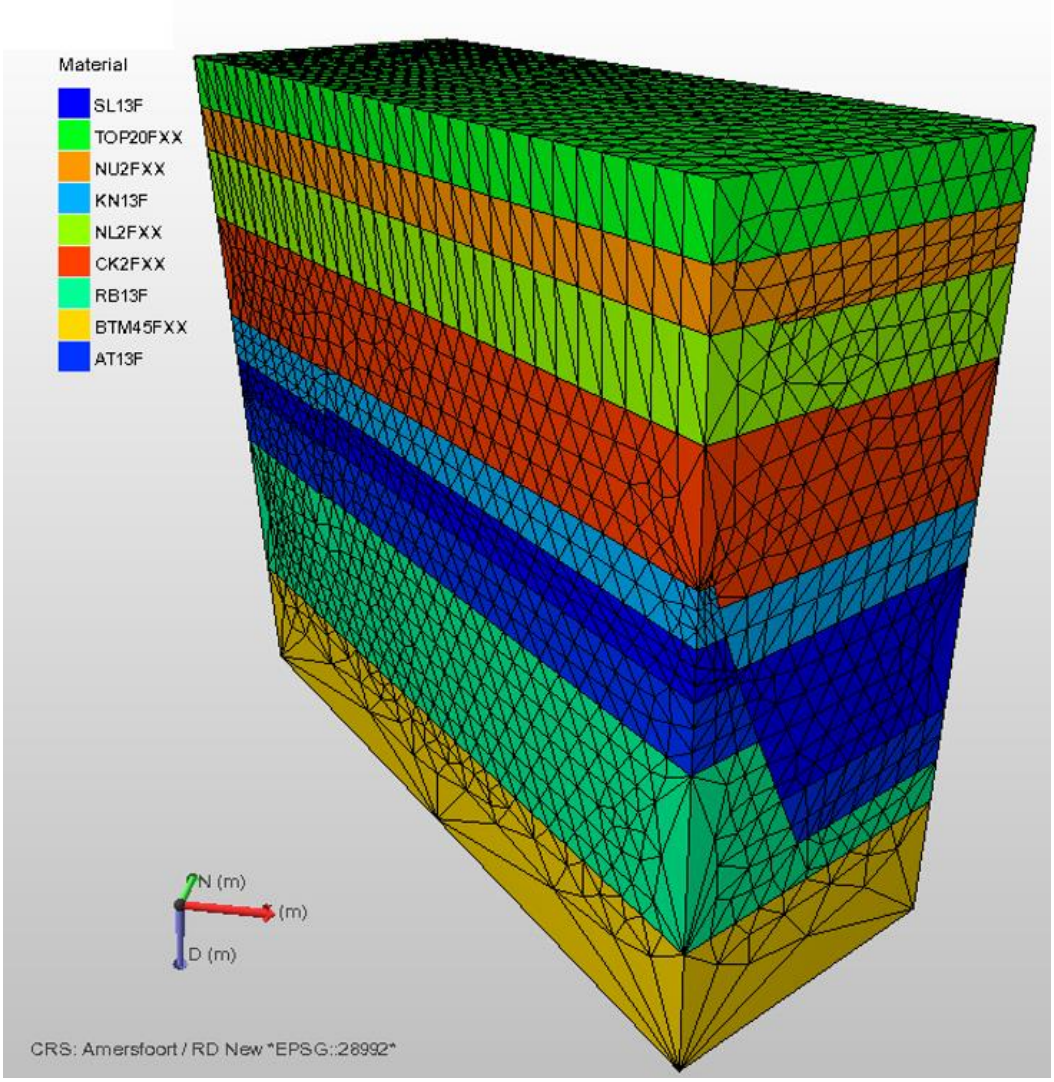

Figure 86. The finite element model and its corresponding material

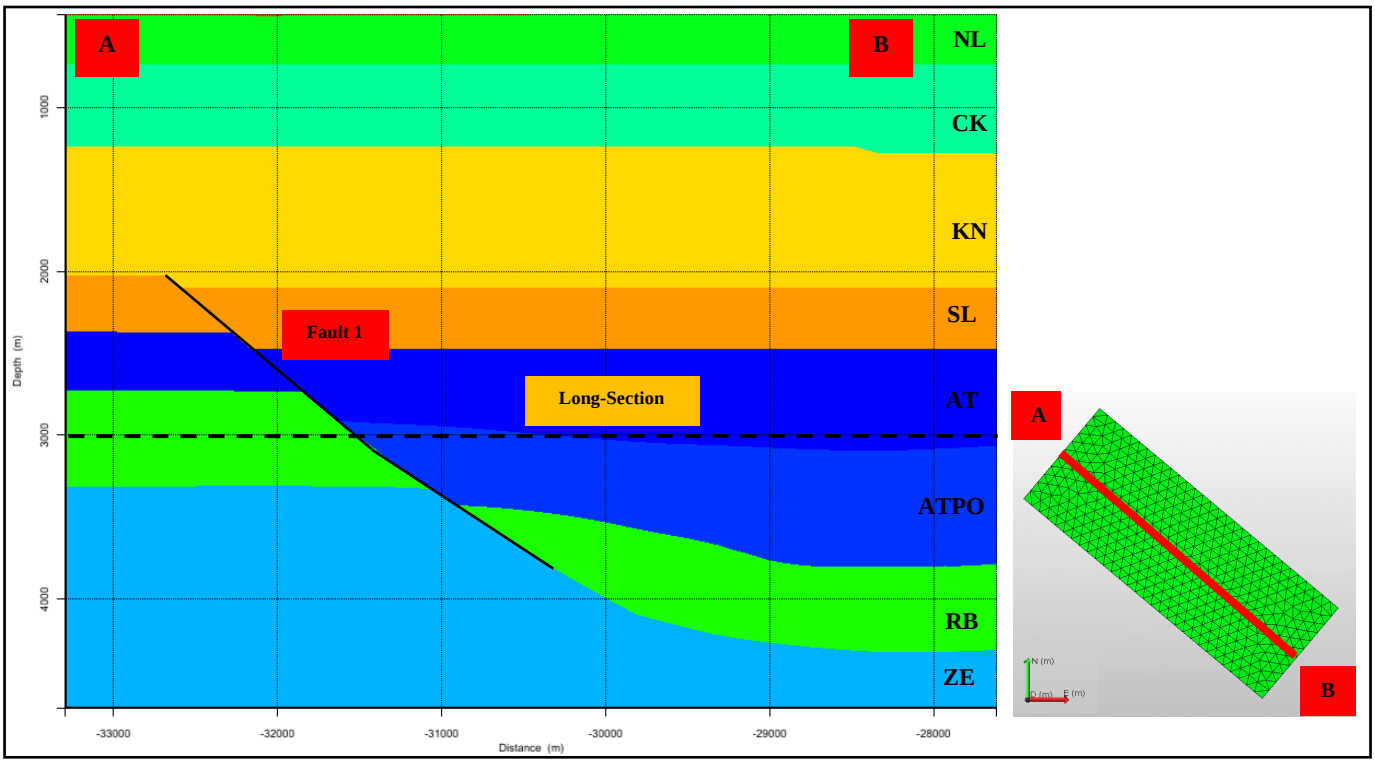

Figure 87. The location of Long-section A-B

Stratigraphy units: NL=Lower North Sea group; CK=Chalk group; KN=Rijnland group; SL=Schieland group; AT=Altena group; ATPO=Posidonia Shale RB=Lower Germanic Triassic group; ZE=Zechstein.

Figure 87 and Figure 88 shows the location and magnitudes profile of the principal stresses within long section A-B. In general, the magnitudes profile of the principal stresses in cross-section (Figure 42) and long sections have a similar trend.

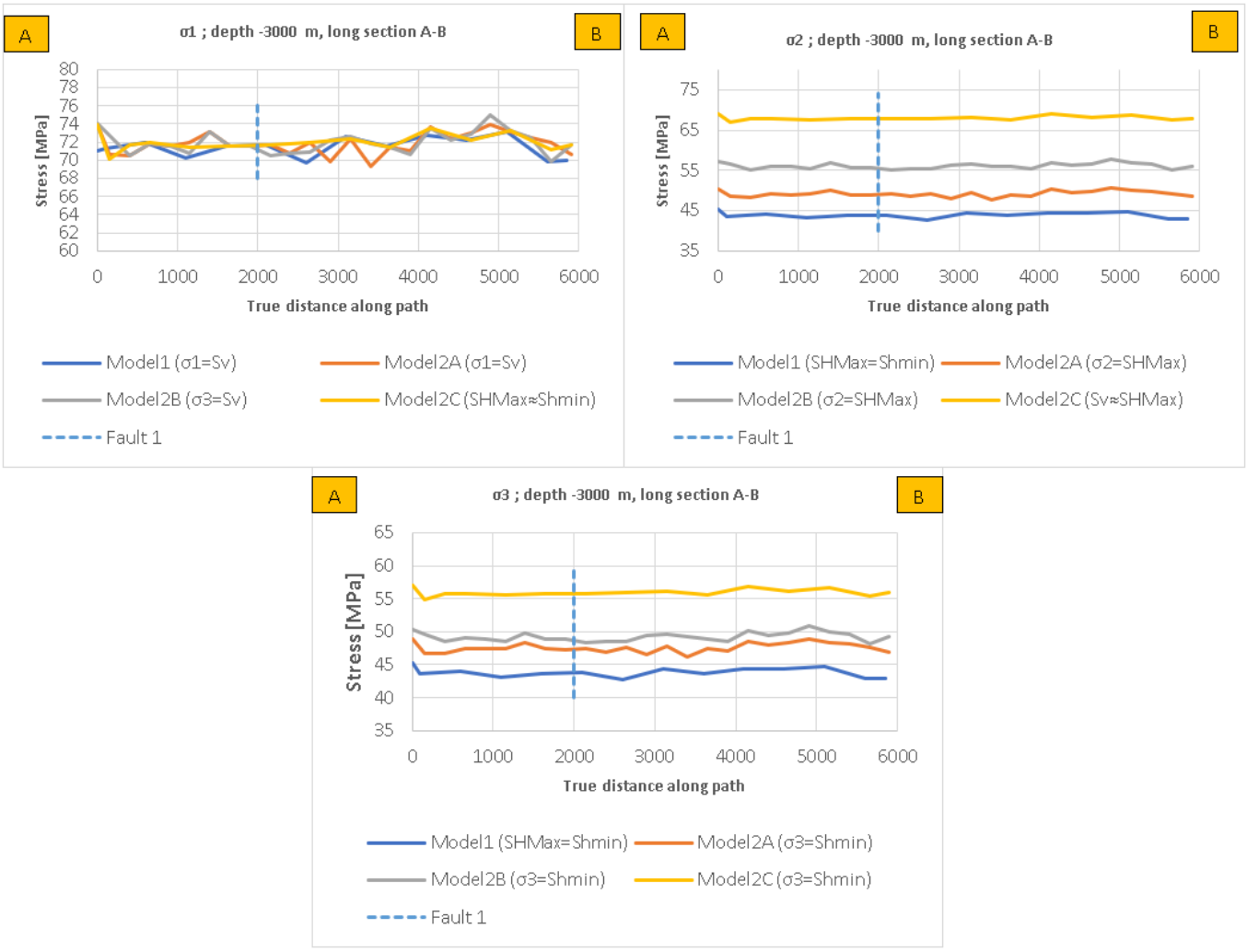

Figure 88. The magnitude of principal stresses in long-section A-B (depth of -3000 m). Left: Maximum principal stress, right: intermediate principal stress, bottom: minimum principal stress

Sensitivity analysis ; Point C – Cross-section 1 ; Depth – 1000 m

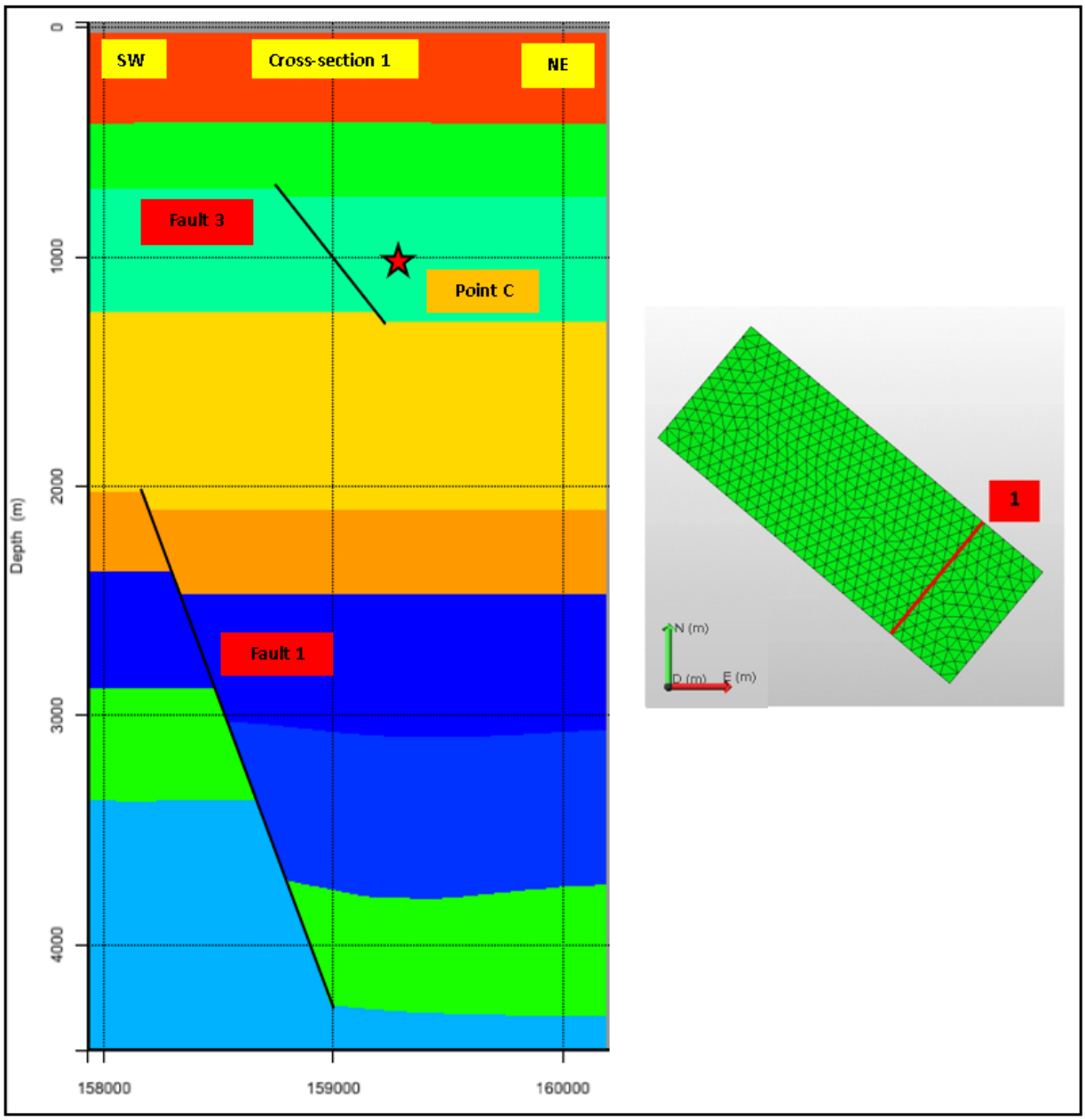

Figure 89. Location point C for sensitivity analysis

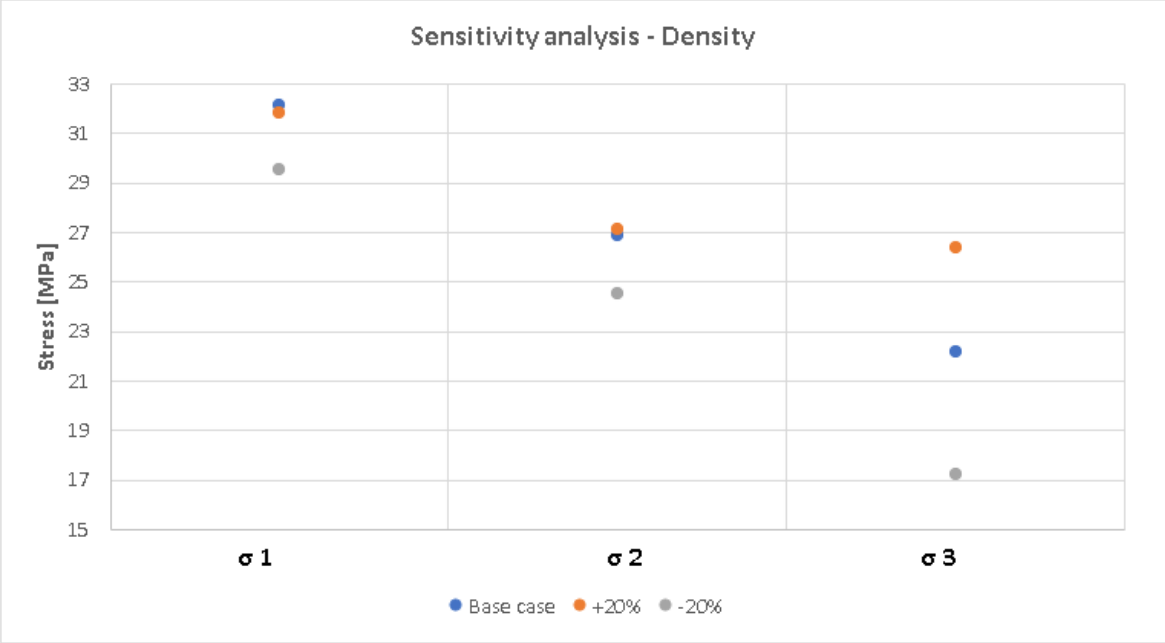

Figure 90. Sensitivity analysis on Density – Point C

This is the other example of sensitivity analysis from Point C, cross-section 1, at a depth of -1000 m (Figure 89). Point C experiences a reverse faulting stress regime, in which the vertical stress becomes the minimum principal stress. Figure 90 depicts that density has a more significant effect on vertical stress (Sv).

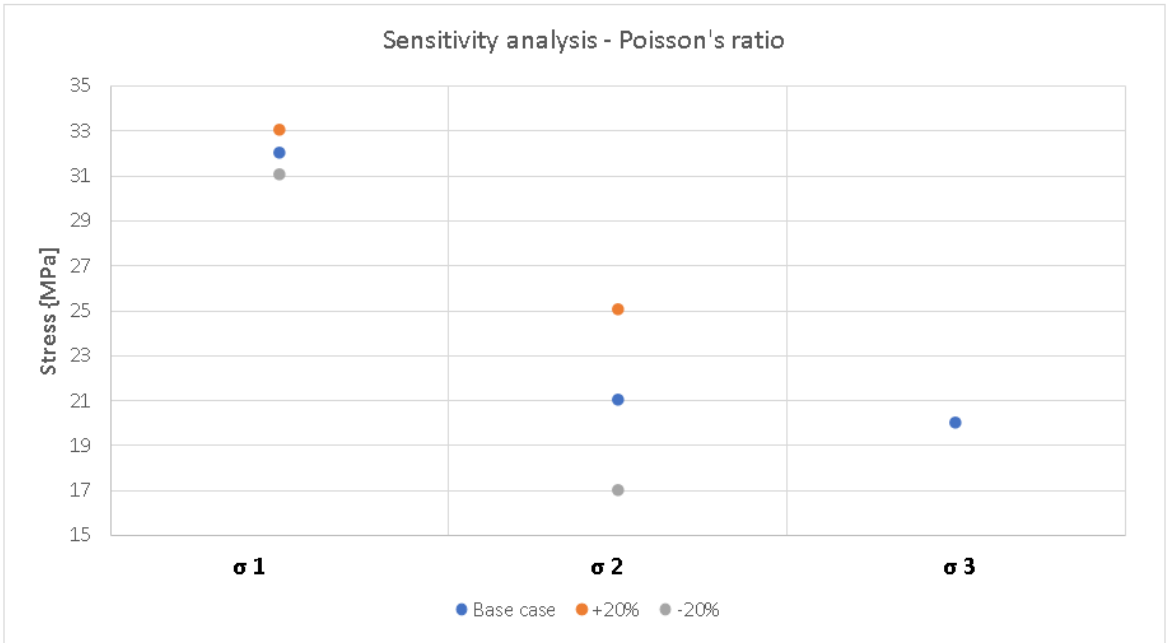

Figure 91. Sensitivity analysis on Poisson's ratio – Point C

On the other hand, Poisson's ratio does not affect the vertical stress (Sv). The intermediate principal stress is the minimum horizontal stress (Shmin). Therefore, changing the value of Poisson's ratio influences more to the intermediate principal stress (Shmin). To be concluded, changing the value

of density and Poisson's ratio has a significant effect on the vertical stress (Sv) and minimum horizontal stress (Shmin), respectively and regardless of the faulting stress regime.

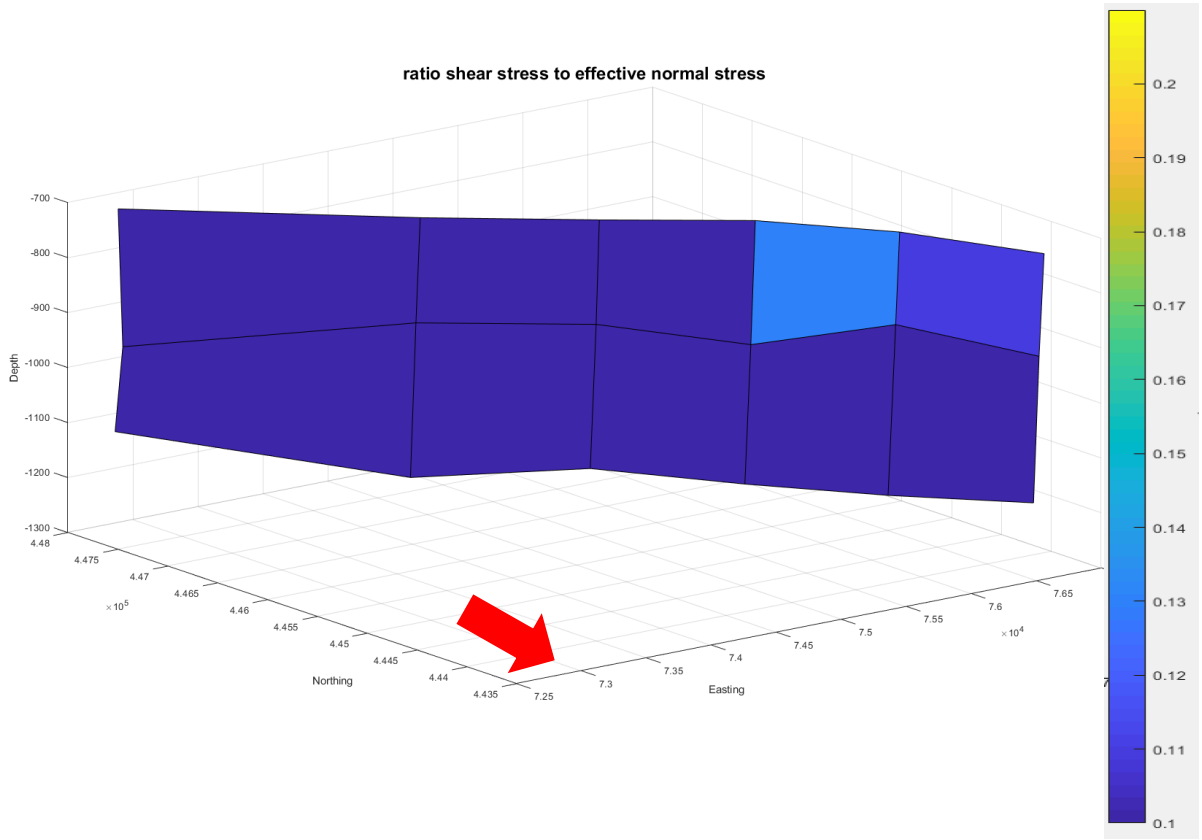

Figure 92. Perspective view of 3D faults with ratio shear stress to effective normal stress–fault 3, under reverse faulting stress regime